Dynamic Rupture Simulations Integrated with Earthquake Observations

Thesis by

Yihe Huang

In Partial Fulfillment of the Requirements for the Degree

of

Doctor of Philosophy

CALIFORNIA INSTITUTE OF TECHNOLOGY

Pasadena, California

2014

(Defended May 8, 2014)

ACKNOWLEDGEMENTS

First of all, I am extremely grateful to my advisor Jean-Paul Ampuero for his full support during my PhD study. He is not only an advisor on scientific research, but also a life mentor and a dear friend. I still remember our first conversation through his phone call on the morning of Chinese New Year 2009. That is one of my most memorable new years as my heart was filled with excitement for the next five years. He has opened a door for me and guided me through the sweetness and bitterness of doing research with fearless spirit.

I thank from the bottom of my heart the great help and guidance from Don Helmberger and Hiroo Kanamori. They have provided me with a kaleidoscope of all aspects of earthquakes. Much of this thesis results from fruitful discussions with them, not to mention how grateful I am for their humor and foresight. I owe a debt of gratitude to Tom Heaton, the advisor of my second oral project, who has given me enormous encouragement and understanding. I've learnt from him the way to conduct research with a rigorous attitude and the courage to speak out with one's own opinion. I am very grateful for the advice of Nadia Lapusta and Victor Tsai, who have always been my role models. I would like to thank members of my oral committee, Jason Saleeby, Jennifer Jackson and Rob Clayton, whose encouragements were so valuable for a beginner in geoscience. My sincere gratitude also goes to Jean-Philippe Avouac, Joann Stock, Mark Simons, Mike Gurnis and Paul Asimow for the fantastic classes they have taught.

Life in Seismo Lab has been such a wonderful journey. Julia Zuckerman and Kim Baker-Gatchalian have always offered me a hand at any time and anywhere. Life is a lot easier with help from Donna Mireles, Evelina Cui, Rosemary Miller, Sarah Gordon and Viola Carter. I've really enjoyed the time with my officemates Asaf Inbal, Brent Minchew, Bryan Riel, Daniel Bowden, Lijun Liu, Lingsen Meng, Vanessa Andrews and YoungHee Kim, who make every day a great day. I have learned from them positive attitudes and persistent passion for research. I would also like to thank Daoyuan Sun, Francisco Ortega, Laura Alisic, Ting Chen and Xiangyan Tian, who gave me a lot of help in my first year. I owe my sincere thanks to Dongzhou Zhang, Dunzhu Li, Junle Jiang (and his family), Kangchen Bai, Shengji Wei (and his wife Jiangyan), Xiaolin Mao, Yingdi Luo, Yiran Ma, and Zhongwen Zhan, who make me feel not far away from home.

My special thanks go to Jianwen Liang, who introduced me to the field of earthquake sciences and encouraged me to pursue a career in academia. All my dreams could not have come true without the unconditional love of my dear parents and my dear husband.

ABSTRACT

Dynamic rupture simulations are unique in their contributions to the study of earthquake physics. The current rapid development of dynamic rupture simulations poses several new questions: Do the simulations reflect the real world? Do the simulations have predictive power? Which one should we believe when the simulations disagree? This thesis illustrates how integration with observations can help address these questions and reduce the effects of non-uniqueness of both dynamic rupture simulations and kinematic inversion problems. Dynamic rupture simulations with observational constraints can effectively identify non-physical features inferred from observations. Moreover, the integrative technique can also provide more physical insights into the mechanisms of earthquakes. This thesis demonstrates two examples of such kinds of integration: dynamic rupture simulations of the M_w 9.0 2011 Tohoku-Oki earthquake and of earthquake ruptures in damaged fault zones:

(1) We develop simulations of the Tohoku-Oki earthquake based on a variety of observations and minimum assumptions of model parameters. The simulations provide realistic estimations of stress drop and fracture energy of the region and explain the physical mechanisms of high-frequency radiation in the deep region. We also find that the overridding subduction wedge contributes significantly to the up-dip rupture propagation and large final slip in the shallow region. Such findings are also applicable to other megathrust earthquakes.

(2) Damaged fault zones are usually found around natural faults, but their effects on earthquake ruptures have been largely unknown. We simulate earthquake ruptures in damaged fault zones with material properties constrained by seismic and geological observations. We show that reflected waves in fault zones are effective at generating pulse-like ruptures and head waves tend to accelerate and decelerate rupture speeds. These mechanisms are robust in natural fault zones with large attenuation and off-fault plasticity. Moreover, earthquakes in damaged fault zones can propagate at super-Rayleigh speeds that are unstable in homogeneous media. Supershear transitions in fault zones do not require large fault stresses. In the end, we present observations in the Big Bear region, where variability of rupture speeds of small earthquakes correlates with the laterally variable materials in a damaged fault zone.

TABLE OF CONTENTS

LIST OF FIGURES

LIST OF TABLES

NOMENCLATURE

Slip. The relative displacement at a given fault location.

Rise time. The local duration of slip.

Crack-like rupture. Rupture with rise time comparable to the overall rupture duration.

Pulse-like rupture (or slip pulse). Rupture with rise time much shorter than the overall rupture duration.

Fault stress. The stresses applied to fault.

Stress drop (static). The difference between stresses before and after an earthquake.

Fault strength. The ability of fault to withstand an applied stress (usually shearing).

Static strength. The fault strength right before it starts moving.

Dynamic strength. The fault strength when it is moving.

Strength drop (or strength excess). The difference between static strength and dynamic strength.

Critical slip distance. The slip needed for fault strength to drop from static level to dynamic level.

C h a p t e r 1

INTRODUCTION

Earthquakes are usually associated with brittle failure, and thus could be described by the Mohr-Coulomb model: earthquakes initiate when fault stress exceeds fault strength. Assessment of earthquake probability would be feasible if fault stress and strength were measurable. However, both of the quantities are not static given the short time scale of earthquakes. Stresses are modulated by waves propagating in the surrounding medium. Frictional strength is constantly perturbed by the change of sliding velocity, temperature, contact materials and pore fluids. Moreover, earthquakes are not a sudden failure of the whole fault, but a propagation of shear cracks (or pulses) at a certain range of speeds. Hence, how large the earthquakes turn out to be really depends on the spatial and temporal variations of stresses and fault strength.

Numerical simulations have proved very useful in the provision of physical insights into complex problems. In particular, dynamic rupture simulations consider the effect of wave interactions and advance together with laboratory rock deformation experiments and high-resolution earthquake observations. Rock friction constitutive laws derived from laboratory experiments help regularize numerical models and lead to breakthroughs in understanding earthquake rupture processes [Ida, 1972; Andrews, 1976; Madariaga, 1976; Dieteric, 1978, 1979; Day, 1982a, 1982b; Ruina, 1983]. The growing high-quality seismic network and detailed observations of large earthquakes result in the development of more realistic fault models [Heaton, 1990; Wald and Heaton, 1994; Cochard and Madariaga, 1996; Olsen et al., 1997]. For the past decade, dynamic models of complex earthquake ruptures are more feasible thanks to booming computer power [Harris et al., 2009], the achievement of seismic slip rates in experiments [Di Toro et al., 2011] and the innovation of seismic imaging methods [Ishii et al., 2005].

A series of key questions emerge with the rapid development of dynamic rupture simulations. How many features in the simulations can we trust? Can we use the simulations to "predict" earthquakes? What is the fundamental physics behind the variety of dynamic rupture models? To answer these questions, first of all, we need to be aware of the non-uniqueness of dynamic rupture simulations [Goto and Sawada, 2010], which are more sensitive to stress drop rather than absolute shear stress. There also exists a tradeoff between strength drop (or strength excess) and critical

slip distance, the product of which is fracture energy that ultimately controls rupture propagation. Keeping this in mind, we should always use observations and laboratory experiments to constrain assumptions of model parameters. On the other hand, simulations that can reproduce every detail of observations are not necessarily true given the non-uniqueness of kinematic inversion problems [Ide, 2007]. The assumptions of Green's functions, fault geometry and source time functions can introduce non-realistic and non-physical features in the inversion results.

The next two chapters in the thesis are devoted to addressing the above issues by using the 2011 Mw9.0 Tohoku-Oki earthquake as an example: (1) Chapter 2 elucidates a 2D dynamic rupture model that provides physical interpretations of the Tohoku-Oki rupture. The model assumptions are kept minimal, but the results are capable of explaining the key features. We also integrate for the first time dynamic rupture simulations and results from back-projection [Ishii et al., 2005; Meng et al., 2011], a new method of imaging ruptures in large earthquakes. (2) Chapter 3 discusses a variety of observations (e.g., slip inversions) from the earthquake and uses them as constraints for model parameters. We find that three different dynamic models are sufficient to explain the variety of available observations. We constrain the values of critical slip distance using the observed frequency-dependent rupture process and solve the trade-off between strength drop and critical slip distance. The models provide realistic estimations of several important source parameters such as stress drop and fracture energy, and emphasize the significant role of subduction wedges on the possible large slip near the trench.

Another crucial contribution of dynamic rupture modeling is to identify individual types of complexity that can affect or even control earthquake ruptures. Such contribution is of more practical importance when the individual types of complexity can be characterized in nature. In particular, along with the complexity of stresses and strengths, dynamic rupture simulations can also consider different geometries and materials. Natural faults are rarely single planes. They exhibit rough surfaces at different scales [Dunham, et al., 2011b] and link among primary planes and secondary fault strands. Earthquakes may propagate through different fault strands by jumping the stepovers [Harris and Day, 1993; Oglesby, 2008] or by changing rupture propagation direction [Kame et al., 2003]. Most of the fault strands exist in so-called fault zones, which are usually damaged, given the nature of strain localization. As revealed by the recent high-resolution analyses of both seismic and borehole data (Table 1.1), the damaged fault zones around most

major faults are usually several hundred meters wide with seismic velocities 20-65% lower than the surrounding medium. They may reach as deep as ~10 km or may only exist in the top ~3-4 km [Ben-Zion, et al., 2003; Li et al., 2007]. Although these fault zones were found to be prominent in natural faults, a homogeneous medium is still a common underlying assumption in dynamic rupture simulations and kinematic inversions. How such near-fault structures affect earthquake ruptures as well as long-term evolution of fault stresses still remains largely unknown.

Table 1.1 Summary of material properties of main fault zones

Fault Zones	Width (m)	Velocity Reduction (%)	Q_s	References
San Andreas	~ 150	30-40	10-40	[Lewis and Ben-Zion, 2010]
	~ 200			[Li et al., 2006]
San Jacinto	125-180	35-45	20-40	[Lewis et al., 2005]
	150-200	25-60		[Yang and Zhu, 2010]
Landers	270-360	35-60		[Li et al., 2007]
	150-200	30-40	20-30	[Peng et al., 2003]
Hector Mine	75-100	40-50	10-60	[Li et al., 2002]
Calico	~ 1500	40-50		[Cochran et al., 2009]
	~ 1300	40-50		[Yang et al., 2011]
Nojima	100-220			[Mizuno et al., 2008]
Anatolian	~ 100	50	10-15	[Ben-Zion et al., 2003]

We use two chapters to investigate the possible role of damaged fault zone structures on earthquake ruptures: (1) In Chapter 4, we formulate this problem by using a 2D symmetric fault zone with certain widths and velocity reductions. The fault is governed by a modified slip-weakening friction law. We find that ruptures in fault zones with strong enough velocity reductions behave as slip pulses rather than cracks. Such pulses are generated by waves reflected from the boundaries of the fault zone and are robust to variations of stresses and fault zone structure smoothness. This new mechanism of pulse generation implies that on natural faults surrounded by damaged fault zones earthquakes are unlikely to propagate as pure cracks. The fault zones can also induce multiple rupture fronts involving coexisting pulses and cracks, which contribute to the complexity of high-frequency ground motions. (2) In Chapter 5, we investigate ruptures on faults governed by strongly velocity-weakening friction law and find a richer behavior of ruptures: ruptures can propagate as multiple slip pulses with oscillating rupture speeds in damaged fault zones. We characterize the relation between fault-zone structures and rupture properties through a systematic parameter study, and investigate the respective

contribution of waves by using kinematic models. We find that as long as these waves are present in natural fault zones, they will interact with earthquake ruptures and modulate rupture properties. Furthermore, we consider the possible role of inelasticity in natural fault zones and incorporate attenuation and off-fault plasticity in our models. We find that earthquake ruptures in plastic fault zones may leave a permanent signature in the geological record.

In Chapter 6, we discuss the possibility of using dynamic rupture simulations to "predict" earthquake observations. Through such closed-loop studies, we can verify the findings from simulations and provide more physical insights into observations. In particular, we find through simulations that earthquakes in damaged fault zones can propagate at super-Rayleigh speeds that are unstable in a homogeneous medium. However, such speeds are observed in several moderate and large earthquakes, such as 1979 M_w 6.5 Imperial Valley earthquake [Archuleta, 1984; Spudich and Cranswick, 1984], 1999 M_w 7.2 Düzce earthquake [Birgören et al., 2004; Bouin, et al., 2004; Konca et al., 2004] and 2009 M_w 4.6 Inglewood earthquake [Luo et al., 2010]. Tan and Helmberger [2010] find that a M_w 3.5 event in the 2003 Big Bear sequence also propagated at an unstable super-Rayleigh speed, which seems related to its vicinity to the main fault. We analyze the high-frequency data of clusters of several M_w 2.1-3.1 earthquakes in detail and demonstrate that a damaged fault zone with laterally variable materials exists in the Big Bear region. Such heterogeneous fault zone structure results in variability of rupture speeds of small earthquakes. With the development of dynamic models of complex earthquake ruptures and the growth of seismic instrumentation and imaging techniques, the integrative approach will become more feasible and crucial for understanding earthquake processes and contribute ultimately to the mitigation of seismic hazards.

C h a p t e r 2

A DYNAMIC MODEL OF THE FREQUENCY-DEPENDENT RUPTURE PROCESS OF THE 2011 TOHOKU-OKI EARTHQUAKE

Huang, Y., L. Meng, and J.-P. Ampuero (2012), A dynamic model of the frequency-dependent rupture process of the 2011 Tohoku-Oki earthquake. Earth, Planets and Space, special issue "The 2011 Tohoku Earthquake", 64(12), 1061-1066, doi: 10.5047/eps.2012.05.011.

We present a 2D dynamic rupture model that provides a physical interpretation of the key features of the 2011 Tohoku-Oki earthquake rupture. This minimalistic model assumes linear slip-weakening friction, the presence of deep asperities and depth-dependent initial stresses. It reproduces the first-order observations of the along-dip rupture process during its initial 100 s, such as large static slip and low-frequency radiation up-dip from the hypocenter, and slow rupture punctuated by high-frequency radiation in deeper regions. We also derive quantitative constraints on the ratio of shallow versus deep radiation from teleseismic back-projection source imaging. This ratio is explained in our model by the rupture of deep asperities surrounded by low stress drop regions, and by the decrease of initial stresses towards the trench.

2.1 Introduction

The data recorded during the Mw 9.0 2011 Tohoku-Oki earthquake provides a transformative opportunity to gain insight into the physics of devastating mega-earthquakes. Numerous studies are shaping our view of the static and kinematic aspects of the rupture process of this event. A striking feature is the large slip in the shallower region. Ocean-bottom pressure gauge, tsunami, and multi-beam bathymetric data indicate that slip near the trench is as large as 50 to 80 m [Fujiwara et al., 2011; Ito et al., 2011; Kanamori and Yomogida, 2011]. Kinematic slip inversions also place the area of largest slip up-dip from the hypocenter [Kanamori and Yomogida, 2011; Koketsu et al., 2011; Pollitz et al., 2011]. Another striking feature is the distinct location of high-frequency (HF) and low-frequency (LF) slip. Teleseismic back-projection studies find that the HF energy around 1 Hz originates from the deeper region [Kanamori and Yomogida, 2011; Meng et al., 2011; Yao et al., 2011], while other studies see the low-frequency radiation comes from the shallower region [Simons et al., 2011; Wei et al., 2011]. The present work aims to provide a dynamic interpretation

of the contrasted frequency content of slip in the deeper and shallower regions of the Tohoku-Oki earthquake rupture. To quantitatively constrain the dynamic model we derive in Section 2.2 an estimate of the ratio of shallow versus deep HF source amplitude from the back-projection source imaging of Meng et al [2011].

The evolution of the rupture speed down-dip from the hypocenter is also constrained by back-projection studies. Meng et al. [2011] described it as a very slow initial phase (<10 s), followed by a stage of regular rupture speed (<20 s), and finally a stage of slow rupture speed of order 1 km/s interspersed with HF radiation episodes (<90 s). Because the slip rate, rise time and up-dip rupture speed are less robustly determined by current studies, we do not include them as first-order constraints in our model.

In Section 2.3 we formulate a 2D dynamic rupture model that is consistent with the key observations described above. Simulation results are presented and discussed in Section 2.4 and 2.5. Our model is obviously not unique [Goto and Sawada, 2010] and is deliberately minimal in its assumptions. Its scope is limited to the initial 100 s of the rupture process, before the rupture became dominated by along-strike rupture propagation. It nevertheless constitutes a demonstration of a conceptual interpretation of the depth-dependent frequency content and slow down-dip rupture of the Tohoku-Oki earthquake proposed by Meng et al. [2011]. It also provides a basis for more sophisticated 3D dynamic modeling [Galvez et al, 2011].

2.2 Back Projection Constraints on Shallow vs. Deep HF Source Amplitude

Meng et al [2011] employed a novel, high-resolution multitaper-MUSIC array processing technique to image the rupture process of the Tohoku-Oki earthquake at high frequency around 1 Hz based on teleseismic data recorded by the USArray and the European seismic network. Location and timing of HF radiation sources were robustly constrained but less attention was paid to their amplitude. In order to provide a quantitative constraint on HF source amplitude, we derive an upper bound on the HF slip rate power in the shallower regions relative to the deeper regions. We estimate the minimum value of the amplitude ratio between shallow secondary peaks over deep primary peaks of the back-projection images that allows the detection of shallow sources without ambiguity. We then convert this into a threshold on HF slip rate amplitude ratios.

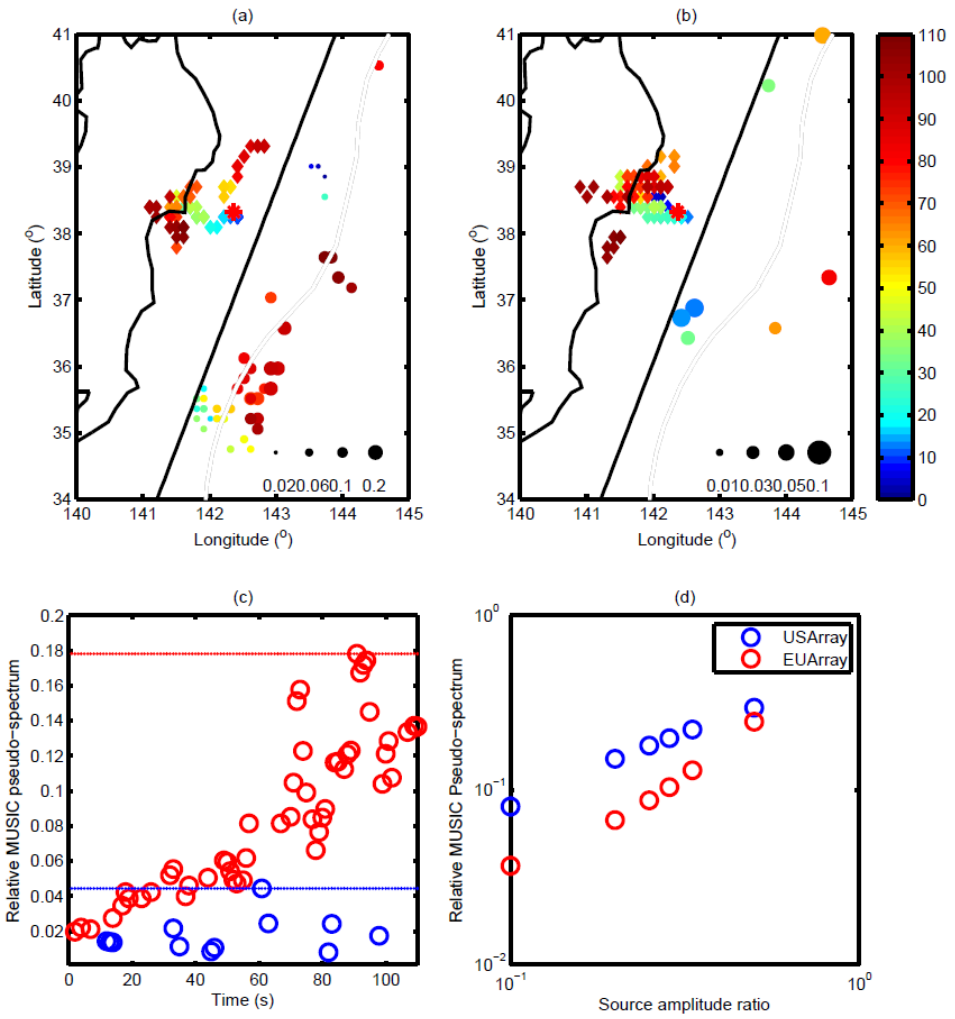

Figure 2.1: Shallow secondary features of Tohoku-Oki earthquake identified in MUSIC back-projection from (a) USArray and (b) European array. The thick black line, double line curve and black line east of the epicenter (red star) are the Japanese coastline, the trench and our conventional boundary between "deep" and "shallow" sources. The deep high frequency radiators (diamonds) and shallow local maxima (circles) are also shown. The color indicates rupture time. The size of the circles denotes the ratio between the amplitude of the shallow MUSIC pseudo-spectrum peak and that of the contemporaneous global maximum. (c) The ratio between shallow and deep simultaneous MUSIC pseudo-spectrum maxima for the European array (red) and USArray (blue). The dashed lines indicate the largest ratio for each array. (d) Shallow/deep MUSIC pseudo-spectrum ratio as a function of shallow/deep source amplitude ratio.

We define the boundary between "deep" and "shallow" as a line striking 210 degrees at a distance of 0.5 degrees east from the epicenter. In each frame of the first 110 s of Meng et al [2011]'s back-

projection images of the USArray and European array data we identify the largest secondary peak of the MUSIC pseudo-spectrum at shallow depth (Figures 2.1a and 2.1b). These secondary peaks are of uncertain origin: they could be either true shallow sources, sidelobes of the deep sources or artifacts introduced by coda waves. We compute the ratio of these secondary peaks (when they exist) over the deep global maxima (Figure 2.1c). We take the maximum ratio over all time frames to represent the threshold for unambiguous detection of shallow sources: ~0.18 for the European array and ~0.04 for the USArray. The larger threshold at the European array is attributed to stronger artifacts and aliasing due to its sparser station distribution, although these artifacts do not affect the analysis of the strongest deep radiators.

To convert this threshold on the MUSIC pseudo-spectrum ratio into a threshold on relative source amplitude we analyze synthetic scenarios comprising two simultaneous point sources, located 1 degree down-dip and 1 degree up-dip, respectively, from the JMA mainshock epicenter. The 2 degrees distance is approximately the separation between the location of the HF radiators [Meng et al, 2011] and the peak slip region close to trench [Fujiwara et al, 2011, Ito et al 2011, Koketsu et al, 2011]. Synthetic Green's functions at teleseismic distance including the effect of a regional velocity model for Japan [Miura et al, 2005] were computed by interfacing a spectral element code (SPECFEM3D, Tromp et al, 2008) and a generalized ray theory code [Chu et al, 2009]. We applied MUSIC back-projection to the synthetic waveforms from double-source scenarios with a range of seismic moment ratios between the shallow and deep sources, and measured the ratio of shallow vs. deep MUSIC pseudo-spectrum peaks. We obtained a power law relationship between MUSIC pseudo-spectrum ratio and source amplitude ratio (Figure 2.1d). Combining these calibration curves with the MUSIC pseudo-spectrum ratio threshold derived previously, we estimate that the source amplitude ratio threshold is 0.5 for the European array and 0.1 for USArray. We conclude that during the Tohoku-Oki earthquake the deep sources were at least 10 times as strong as the shallow ones at 1 Hz.

2.3 Dynamic Rupture Model Assumptions

Our 2D dynamic rupture model of the Tohoku-Oki earthquake comprises a 200 km wide thrust fault with a dip angle of 14^{o} embedded in a homogeneous elastic half space (Figure 2.2). The assumed density, shear modulus and Poisson's ratio are 3000 kg/m^3, 30 GPa and 0.25, respectively. The fault is governed by the linear slip-weakening friction law with static and dynamic friction coefficients of

0.6 and 0.2, respectively, and critical slip-weakening distance of 3 m except in five deep asperities in which the critical distance is 1 m. The shallower region of the Tohoku megathrust has usually been considered weakly coupled [Loveless and Meade, 2010], since few earthquakes had occurred there. In comparison, the deeper region has ruptured several times in Mw 7 and Mw 8 events and hosts numerous repeating earthquake sequences [Igarashi et al., 2003]. Thus, the deeper region certainly contains asperities with a range of sizes [Kanamori and Yomogida, 2011], while the shallower region might be dominated by a large asperity with much longer recurrence time.

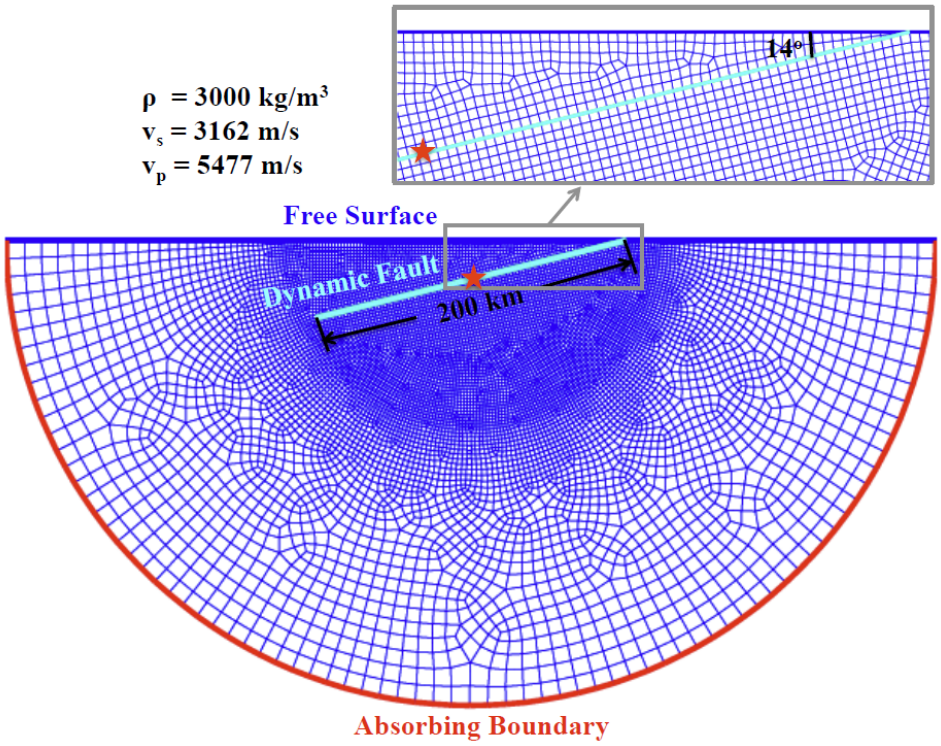

Figure 2.2: The unstructured mesh with free boundary on the top (blue line) and absorbing boundary in a circular (red line). The hypocenter (red star) is in the middle of the 200 km long fault (turquoise line). The zoom-in picture shows the mesh around the fault and the fault dipping angle. The density, S velocity and P velocity are indicated in the top left.

Furthermore, the effective normal stress on the subducted plate interface should increase with depth as a result of the overburden pressure, and decrease significantly in areas of large pore fluid pressure. Tobin and Saffer [2009] found extremely low effective stress in the Nankai subduction zone from the trench to a down-dip distance of 20 km due to elevated pore pressures. Though

similar studies are still lacking in Tohoku, we found that such variation of effective normal stress can explain the rupture behavior of the shallower region. Based on the observation on the Nankai subduction zone, the effective normal stress is set to 10 MPa in a 20 km wide region near the trench and then increases linearly up to 100 MPa at 80 km from the trench.

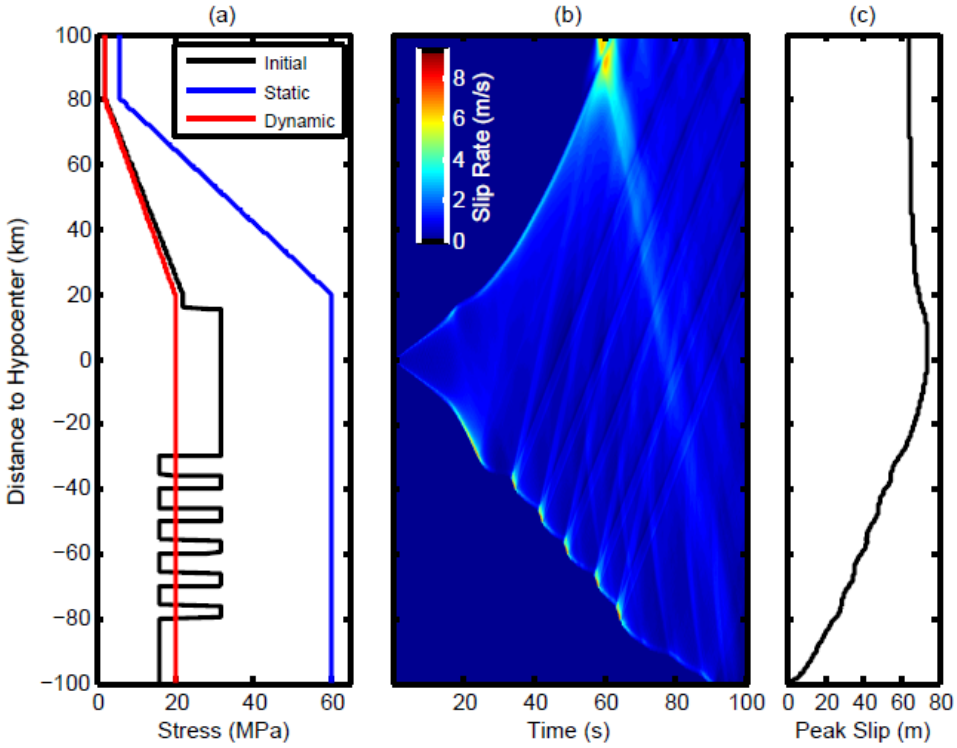

Figure 2.3: (a) Initial shear stress, static strength and dynamic strength in the numerical model setup as a function of distance to the hypocenter. (b) Spatiotemporal distribution of slip rate. (c) Peak slip as a function of distance to the hypocenter.

Figure 2.3a shows our assumed distributions of initial shear stress, static strength and dynamic strength along the fault. The hypocenter is surrounded by a large asperity with high initial shear stress. The shear stress is then reduced in the shallower region and tapered in accordance with the effective normal stress. In the deeper region, we set five small asperities surrounded by areas with negative stress drop. The spontaneous dynamic rupture problem is solved with the 2D spectral element code SEM2DPACK (http://www.sourceforge.net/projects/sem2d/, see e.g. Huang and Ampuero, 2011). The mesh is unstructured and includes progressive coarsening towards a circular absorbing boundary 300 km away from the epicenter (Figure 2.2). We nucleate the rupture using

the time-weakening procedure of Andrews [1985] with imposed rupture speed 800 m/s. The rupture starts propagating spontaneously after 15 s.

2.4 Numerical Results

We show in Figure 2.3b the spatio-temporal distribution of slip rate resulting from our simulation. The rupture propagates bilaterally from the hypocenter. Outside the nucleation region, the up-dip rupture accelerates and reaches the Rayleigh wave speed (~ 2.9 km/s). Near the trench a supershear rupture front emerges ahead of the main front, accompanied by an acceleration of slip rate up to ~ 6.5 m/s due to the effect of the free surface [Nielsen, 1998]. A shallow weak layer, velocity-strengthening friction or off-fault dissipation can help inhibit the supershear transition near the free surface [Kaneko and Lapusta, 2010]. After the rupture reaches the trench, a strong slip acceleration front is generated by the reflection from the free surface (see e.g. Figure 5a in Ma and Beroza, 2008). The front modulates the slip along the fault again, and the final slip in the shallower region is between 64 and 74 m (Figure 2.3c).

In the down-dip direction, the rupture speeds up to ~2 km/s before ~25 s, and then decelerates to ~1 km/s after reaching the region of small asperities, which radiate high-frequency energy. The fast down-dip propagation followed by slow propagation with high-frequency bursts is a key feature in the back-propagation results of Meng et al. [2011]. The strong P and S phases generated by each small asperity interfere with each other and produce an interesting pattern in the spatio-temporal distribution of slip rate (Figure 3b). The peak slip rate inside the small asperities is around 9 m/s. However, this does not lead to a large slip at depth because of the overall small stress drop. The final slip tapers almost linearly towards the bottom of the seismogenic zone (Figure 2.3c).

To study the spatial complementarity between LF and HF slip we filter the simulated slip rate in different frequency bands: an LF band with frequencies lower than 0.1 Hz, an HF band with frequencies of 0.5 - 1 Hz and an HF band with frequencies higher than 0.75 Hz. We plot the HF and LF peak slip rate values in Figure 4a. The 0.5 - 1 Hz peak slip rate in the deeper region is about four times as large as that in the shallower region, and it is roughly five times for frequencies higher than 0.75 Hz. Simulations that ignore the tapering of initial stresses towards the trench produce very large HF slip near trench, while simulations without deep asperities reproduce the observed slow front but not the deep HF radiation.

To facilitate the comparison between our simulation and the back-projection result, we compute the HF slip rate power over a 10 s sliding window and apply a spatial Gaussian smoothing with a half width of 50 km, comparable to the main lobe width of the array response of the USArray and the European array (Figure 2.4b). We find that the overall source power in the deeper region is at least three times larger than in the shallower region, and the power ratio increases with frequency. Hence, the simulation demonstrates that a depth-dependent distribution of asperities is a viable mechanism to explain why the Tohoku-Oki radiated more HF energy from its deeper regions.

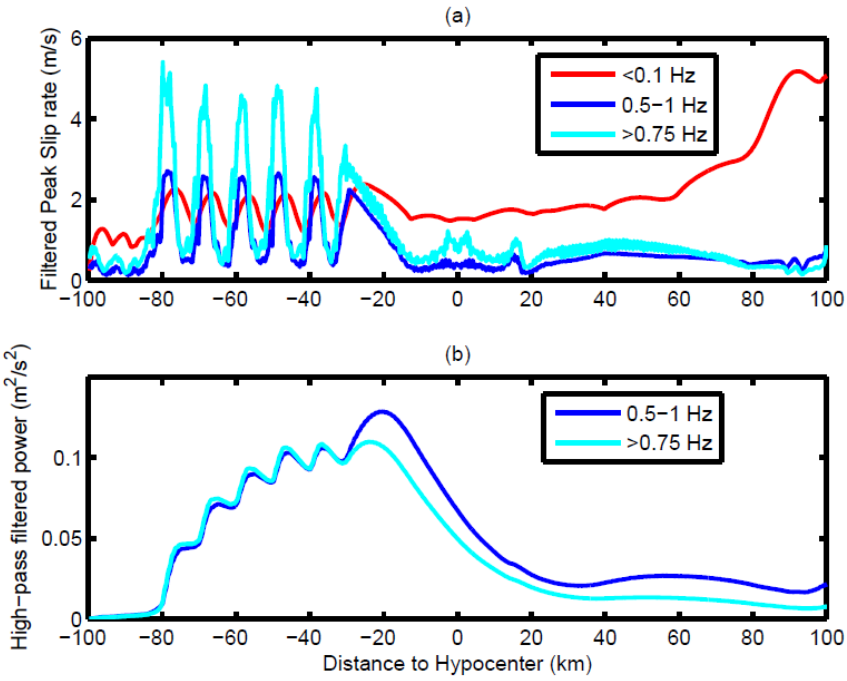

Figure 2.4: (a) Low-pass filtered (<0.1 Hz) and high-pass filtered (0.5-1.0 Hz and >0.75 Hz) peak slip rates as a function of distance to the hypocenter. (b) Calculated power of the high-pass filtered peak slip rates.

2.5 Conclusion and Discussion

We present a 2D dynamic rupture simulation that incorporates multiple deep asperities and depth-dependent initial stress. The simulation successfully reproduces the following first-order observations of the rupture process of the 2011 Tohoku-Oki earthquake: a large portion of the final slip in the shallower region, the spatial separation between sources of low-frequency and high-frequency slip, a period of slow down-dip rupture propagation punctuated by high-frequency bursts. We develop an estimate of the ratio of slip rate power in the shallower versus the deeper regions

based on the MUSIC back projection analysis, which we then reproduce in our dynamic rupture simulations.

Our results indicate that the stress state is very different between the shallower and deeper regions. Though the initial stress in the shallower region is barely above the dynamic strength, the reflected waves inside the front wedge induce high transient stress drop and large final slip, but no significant overshoot is found. Based on the consistency of our result and the observations, we infer that the initial stress in the shallower region is very low compared to static strength. Thus, it would be difficult to nucleate an earthquake in the shallower region, but the final slip will always be amplified once the rupture propagates through. This behavior should naturally exist in shallow subduction events. Lower initial stress (e.g. equal to dynamic strength) still allows the rupture to break up to the trench, but leads to small final slip (< 50m) in the shallower region.

In the deeper region, the stress state inside and outside the asperities is also distinct. To reproduce the slow average down-dip rupture speed, the initial stress needs to be lower than the dynamic strength in the regions between the asperities. These regions conceptually represent the places where overshoot occurred in the previous earthquakes. Hence, though stress accumulated in the interseismic period, the initial stress still lies below the dynamic strength, which acted as a barrier and lowered the rupture speed during the Tohoku-Oki earthquake. We have explored a range of models of the deep fault region defined by the size of asperities, their density (the inverse of their spacing), their stress drop, and the background initial stress in between. Slow rupture is favored by low values of these parameters, but values that are too low lead to rupture arrest. Large HF radiation requires large values of these parameters, but values that are too large lead to fast rupture and large slip. Hence the family of viable models is somewhat constrained.

Our assumption of slip-weakening friction leads to crack-like rupture instead of pulse-like rupture [Heaton, 1990]. It is still difficult to identify if the Tohoku-Oki earthquake is dominated by crack or pulse behavior. Mechanisms for pulse-like rupture, such as thermal pressurization, in faults with heterogeneous mechanical or hydraulic properties [Noda and Lapusta, 2010] might provide an alternative interpretation of the variable frequency content of slip rate.

The back-propagating slip front emerging from the interaction of dynamic rupture on a dipping fault and the free surface might have contributed to the reactivation of the Tohoku-Oki earthquake rupture at about 100 s. However, the accompanying strong HF radiation near the trench is not

observed. In our simulation, this is suppressed by the tapered initial stresses towards the trench. Alternatively, this might also be achieved by velocity-strengthening or velocity-neutral friction, but at the expense of reducing too much final slip near the trench. Other mechanisms left for future simulations are the anelastic deformation of the frontal wedge and dynamically triggered slip on splay faults [Kanamori and Yomogida, 2011].

C h a p t e r 3

SLIP-WEAKENING MODELS OF THE 2011 TOHOKU-OKI EARTHQUAKE AND CONSTRAINTS ON STRESS DROP AND FRACTURE ENERGY

Huang, Y., J.-P. Ampuero, H. Kanamori (2013), Slip-weakening models of the 2011 Tohoku-Oki earthquake and constraints on stress drop and fracture energy. Pure and Applied Geophysics, 1-14, doi:10.1007/s00024-013-0718-2.

Supplementary materials are included in Appendix A.

We present 2D dynamic rupture models of the 2011 Tohoku-Oki earthquake based on linear slip-weakening friction. We use different types of available observations to constrain our model parameters. The distribution of stress drop is determined by the final slip distribution from slip inversions. As three groups of along-dip slip distribution are suggested by different slip inversions, we present three slip-weakening models. In each model, we assume uniform critical slip distance eastward from the hypocenter, but several asperities with smaller critical slip distance westward from the hypocenter. The values of critical slip distance are constrained by the ratio of deep to shallow high-frequency slip-rate power inferred from back projection source imaging. Our slip-weakening models are consistent with the final slip, slip rate, rupture velocity and high-frequency power ratio inferred for this earthquake. The average static stress drop calculated from the models is in the range of 4.5 MPa to 7 MPa, though large spatial variations of static stress drop exist. To prevent high-frequency radiation in the region eastward from the hypocenter, the fracture energy needed there is in the order of 10 MJ/m^2, and the average up-dip rupture speed cannot exceed 2 km/s. The radiation efficiency calculated from our models is higher than that inferred from seismic data. We find that the structure of the subduction wedge contributes significantly to the up-dip rupture propagation and the resulting slip there.

3.1 Introduction

Analyses of a wealth of data generated by the 2011 Tohoku-Oki earthquake have unveiled several unique features: (1) Rupture propagated through the shallow region (defined here as the region up-dip of the hypocenter), and resulted in large slip. This is supported by slip inversions [Simons et al., 2011; Ide et al., 2011; Yue and Lay, 2011; Yagi and Fukahata, 2011; Lee et al., 2011; Wei et al.,

2012; Iinuma et al., 2012] and static measurements by ocean-bottom pressure gauges and bathymetric data [Fujiwara et al., 2011; Ito et al., 2011; Sato et al., 2011; Kido et al., 2011; Kodaira et al., 2012]. Several slip models are schematically shown in Figure 3.1a. (2) High-frequency ($\sim 1\ Hz$) energy radiation was mostly concentrated down-dip from the hypocenter. Under the assumption that the advancing front of high-frequency radiation coincides with the rupture front, the down-dip rupture velocity was estimated to be as low as ~ 1 km/s [Meng et al, 2011; Kiser and Ishii, 2012].

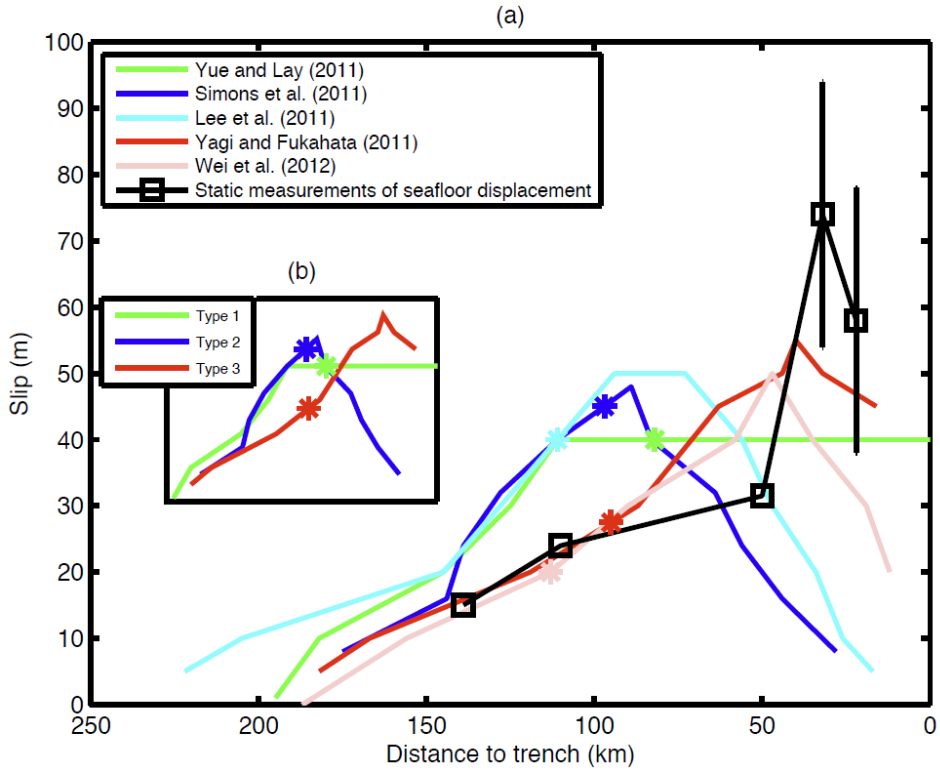

Figure 3.1: (a) The along-dip slip distributions across the hypocenter inferred from five slip inversions. The hypocenter used in each inversion is shown as a star. The displacement of sea floor is shown in black, including five measurements at or near the latitude of hypocenter from Sato et al., 2011, Ito et al., 2011 and Kido et al., 2011. (b) The three types of along-dip slip distributions.

The extensive observations available for this event warrant efforts to understand the basic physics responsible for these unique observations. To this end, we carry out dynamic rupture simulations for this earthquake. Previous studies suggest that heterogeneities of fault friction or stress are needed to explain the spatial variations of rupture behavior during this earthquake [Kato and Yoshida, 2011;

Aochi and Ide, 2011; Duan, 2012; Goto et al., 2012; Huang et al., 2012] as well as the complex temporal characteristics of historical earthquakes [Igarashi et al., 2003; Tajima et al., 2013]. Furthermore, a key question is what causes the rupture to propagate through the shallow region. Numerical simulations suggest that waves reflected inside the subduction wedge induce large transient stress changes on the fault, which promote the up-dip rupture propagation [Huang et al., 2012] despite the stable, velocity-strengthening frictional behavior expected in fault zones at shallow depth [Kozdon and Dunham, 2013]. Other models invoke fault weakening mechanisms in the shallow region, such as shear heating of pore fluids, to promote unstable slip [Yoshida and Kato, 2011; Noda and Lapusta, 2013].

In this paper, we attempt to find numerical models that can provide some useful constraints on the overall physical properties of the earthquake, such as stress drop and fracture energy. To keep the number of assumptions as few as possible, we use a simple elastic model with slip-weakening friction. We will focus on the along-dip rupture process near the latitude of the hypocenter and will try to explain the various observations in the shallow and deep regions, such as variations of slip, radiation frequency spectrum and rupture velocity.

3.2 Model Setup and Observational Constraints on Model Parameters

We consider a shallow-dipping fault with a dip angle of 14^{o} embedded in a 2D elastic half space. The fault is 200 km long in along-dip direction. The hypocenter is located in the middle. Material properties such as density ρ ($3000\,kg/m^3$), Poisson's ratio ν (0.25), and shear modulus μ ($30\,GPa$) are uniform throughout the medium. We solve the problem using a 2D spectral element code (SEM2DPACK, http://www.sourceforge.net/projects/sem2d/) and the unstructured mesh shown in Figure 3.2a [Huang et al., 2012]. We prescribe an artificial nucleation procedure in the hypocentral region. The friction coefficient is forced to drop over a certain time scale from static to dynamic levels inside a region with time-dependent size [Andrews, 1985]. After reaching a critical nucleation size which is much shorter than the total rupture length, the rupture propagates spontaneously to both up-dip and down-dip directions. The linear slip-weakening friction law governs the remaining part of the fault, and the model contains five free parameters: initial shear stress τ_0, normal stress σ_n, static friction coefficient μ_s, dynamic friction coefficient μ_d and critical slip distance D_c (Figure 3.2(b)). We constrain these model parameters using several observations, as described next.

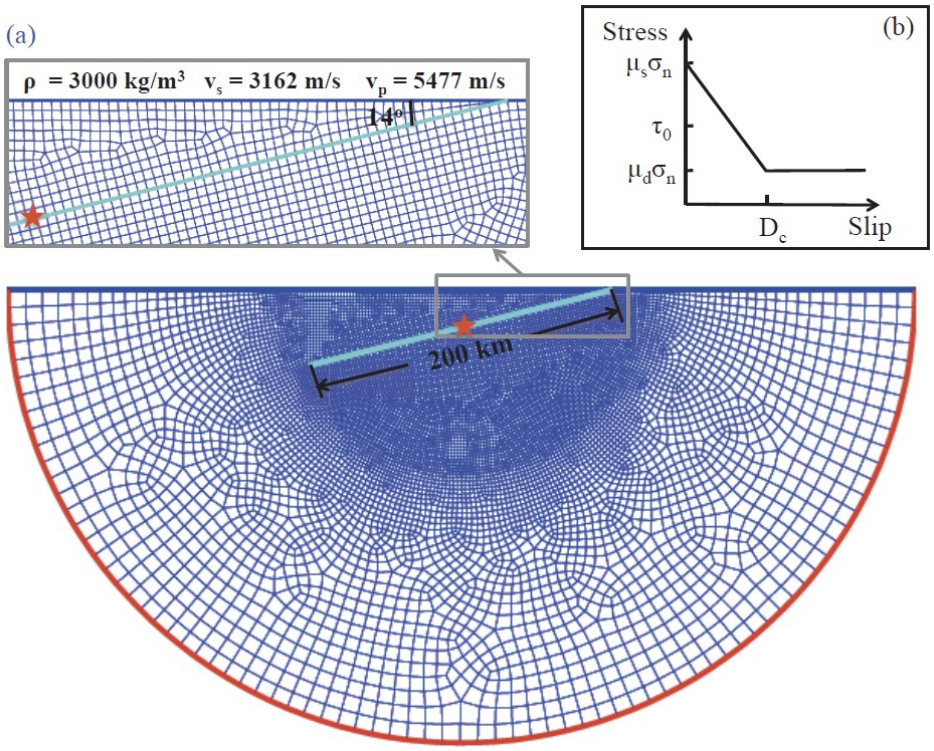

Figure 3.2: (a) The unstructured mesh with a free boundary on the top (blue line) and a semicircular absorbing boundary (red line). The hypocenter is in the middle of the 200-km-long fault (turquoise line). The zoom-in picture shows the mesh around the fault and the dip angle of the fault. The density, S velocity and P velocity are indicated on the top of the zoom-in picture. (b) Linear slip-weakening law. Stress jumps from initial shear stress τ_0 to static strength $\mu_s\sigma_n$ first, and then decreases linearly to dynamic strength $\mu_d\sigma_n$ when slip reaches the critical slip distance D_c. The shear stress then remains at the dynamic strength level.

Normal stress σ_n and friction coefficients μ_s and μ_d

We adopt a normal stress profile from the Nankai region, which has an effective normal stress of about 10 MPa up to a horizontal distance of 20 km from the trench [Tobin and Saffer, 2009]. Further away from the trench, the normal stress is increased to 100 MPa by a vertical gradient of 6 MPa/km, and kept constant in deep regions (Figure 3.3). We initially assume a constant static friction coefficient $\mu_s = 0.6$ and dynamic friction coefficient $\mu_d = 0.2$. As we will illustrate in Section 3.3, the friction coefficients have to be modified in some regions to reproduce the observations.

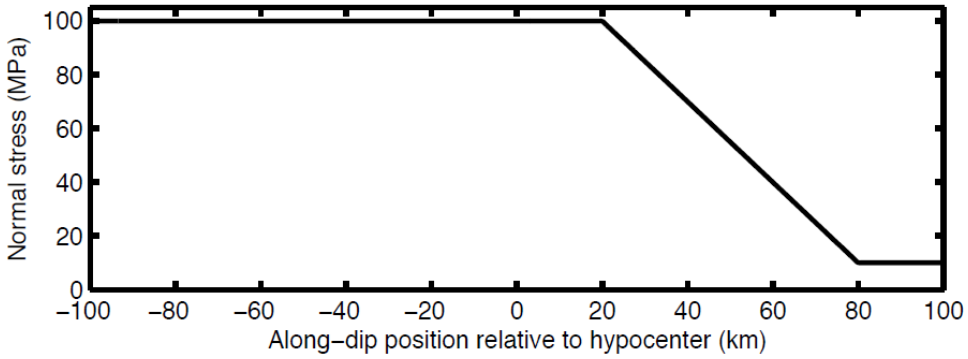

Figure 3.3: The along-dip distribution of normal stress in all three models.

Stress drop $\tau_0 - \mu_d\sigma_n$

The distributions of stress drop $\tau_0 - \mu_d\sigma_n$ are inferred from the coseismic final slip distributions shown in Figure 3.1a. The static stress drop that results from our calculations is different from $\tau_0 - \mu_d\sigma_n$ due to overshoot, and we will discuss the distribution of static stress drop later in Section 3.4. For each slip inversion, we measured roughly the slip at several locations in the along-dip direction across the hypocenter. The figure aims to show the overall differences of the inferred slip profiles, rather than reproduce the details of each model. We find that although in all models large slip is concentrated in the shallow region, the slip profiles are highly variable up-dip from the hypocenters, which are shown by stars. Overall, they fall into three types (Figure 3.1b): (1) almost constant slip in the shallow region (green line in Figure 3.1a), (2) peak slip near the hypocenter (blue and turquoise lines in Figure 3.1a) and (3) peak slip between the hypocenter and the trench (red and pink lines in Figure 3.1a). Static measurements of seafloor displacements (black line in Figure 3.1a) seem to favor large slip near the trench, but have large uncertainties (Ito et al., 2011) and possibly involve post-seismic deformations. Hence, we consider the three possible slip profiles in our numerical models.

Critical slip distance D_c

The results from back-projection source imaging constrain the high-frequency slip-rate power in the deep region. Huang et al. [2012] found that the ratio between deep and shallow high-frequency slip-rate power is at least 10. In order to generate high-frequency radiation in dynamic rupture models, heterogeneities of either fracture energy or initial stress are needed [Madariaga, 1983]. However,

only stress concentrations such as the residual stresses at the edge of a previous slip event can be as efficient as an abrupt change of fracture energy. For computational convenience, we choose to set heterogeneities of fracture energy by varying the value of D_c in our slip-weakening model. To reproduce the spatial contrast of high-frequency radiation, we set a uniform D_c in the shallow region, but several small asperities with much smaller D_c in the deep region. In reality the deep region may have variations of both fault strength and stress, which in combination can give rise to strong high-frequency radiation. A deep region with small asperities also agrees with the fact that earthquakes have repeatedly occurred there in the past [e.g., Igarashi et al., 2003; Tajima et al., 2013]. The spacing of small asperities in our model is conceptual rather than corresponding directly to earthquakes of specific magnitude. However, given the same stress conditions, the spacing needs to be large enough to prevent the down-dip rupture to propagate faster than 1 km/s.

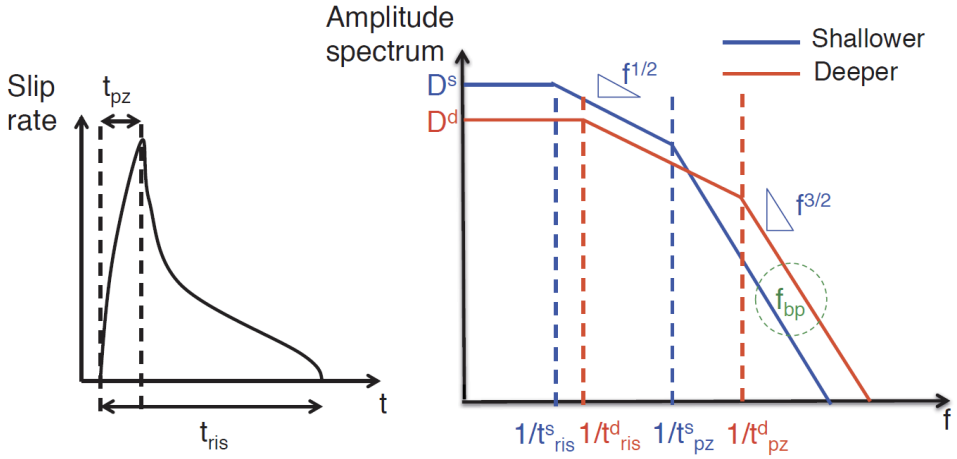

Figure 3.4: Slip rate function with two time scales: rise time t_{ris} and process zone time t_{pz} (left). Amplitude spectrum of the slip rate functions for shallow and deep regions, respectively, denoted by subscript 's' and 'd' (right). The frequency of back projection f_{bp} is also indicated in a dot circle.

It is noteworthy that in such an asperity model the deep/shallow D_c ratio is determined by the high-frequency slip-rate power ratio, as illustrated in Figure 3.4. The amplitude spectrum of slip rate at a certain location on the fault tends to the final slip D at very low frequency. Figure 3.4 shows two amplitude spectra, one for a deep region with final slip D^d and the other for a shallow region with final slip D^s. Each amplitude spectrum has two corner frequencies: the lower one is related to the time required for slip to reach its final value, or rise time t_{ris}; and the higher one is related to the time required for slip to reach D_c, or process zone time t_{pz} (see also Figure 5c in Kaneko et al.,

2008). The latter can be approximated as $t_{pz} \sim \frac{\mu D_c}{(1-\nu)\Delta\tau_s A_{II}(v_R) v_R}$, where ν is Poisson's ratio, v_R is rupture velocity, $\Delta\tau_s$ is the strength drop, i.e. the difference between static and dynamic strength $(\mu_s - \mu_d)\sigma_n$, and A_{II} is a function of rupture speed in mode II given by Equation 5.3.11 in Freund (1990). As D^d, D^s, t_{ris}^d and t_{ris}^s can be inferred from the slip inversions, and the high-frequency slip-rate power ratio from the back projection, the ratio t_{pz}^d / t_{pz}^s can be determined, and so is the deep/shallow D_c ratio D_c^d / D_c^s. Besides, the back projection is carried out in a certain frequency band (e.g., 0.5-1 Hz in Meng et al., 2011). The center of the back-projection frequency band, f_{bp}, should be larger than the second corner frequency in the shallow region, $f_{bp} > \frac{1}{t_{pz}^s}$. This provides a lower bound for D_c^s. We show a detailed mathematical derivation of deep/shallow D_c ratio in terms of high-frequency slip-rate power ratio in Appendix A.

3.3 Results from the Three Models

In this section, we will present dynamic rupture simulations for the three different models that reproduce the three types of along-dip slip profiles (Figure 3.1b).

1st model (constant slip in shallow region)

To reproduce the first slip profile that has a constant slip in the shallow region, we keep the static and dynamic friction coefficients constant. The distributions of model parameters are shown in Figure 3.5. Rupture is forced to propagate bilaterally at $800\ m/s$ inside the nucleation region (Figure 3.6a). After about $20\ s$, the down-dip rupture starts to propagate spontaneously and accelerates until it reaches the low stress-drop region at $30\ km$ from the hypocenter. It then propagates at a speed of about $1\ km/s$ and generates high frequency bursts when it propagates through the small asperities (Figure 3.5). Due to the uniform frictional properties assumed eastward of the hypocenter, the up-dip rupture propagates smoothly. It reaches an average speed of about $2\ km/s$ and produces an almost constant slip in the shallow region (Figure 3.6b). To quantify the distribution of high-frequency radiation we compute at each fault location the peak value of the slip rate high-pass filtered above $0.75\ Hz$. The resulting high-frequency peak slip rate is much larger in the deep region than in the shallow region (Figure 3.6c). In contrast, the peak values of the slip rate low-pass filtered below $0.1\ Hz$ are more uniform. Their values are in the range of 1 to 2 m/s, consistent with the average slip rate from slip inversions [Lee et al., 2011; Wei et al., 2012], except

in the region near the trench. To compare with the high-frequency power ratio in the back projection, we compute the power of the high-pass filtered slip rate over a 10 s sliding window and apply a spatial Gaussian smoothing with a half width of 50 km, a conservative estimate of the spatial smearing in the back-projection source imaging. This leads to a deep/shallow power ratio of about 10.

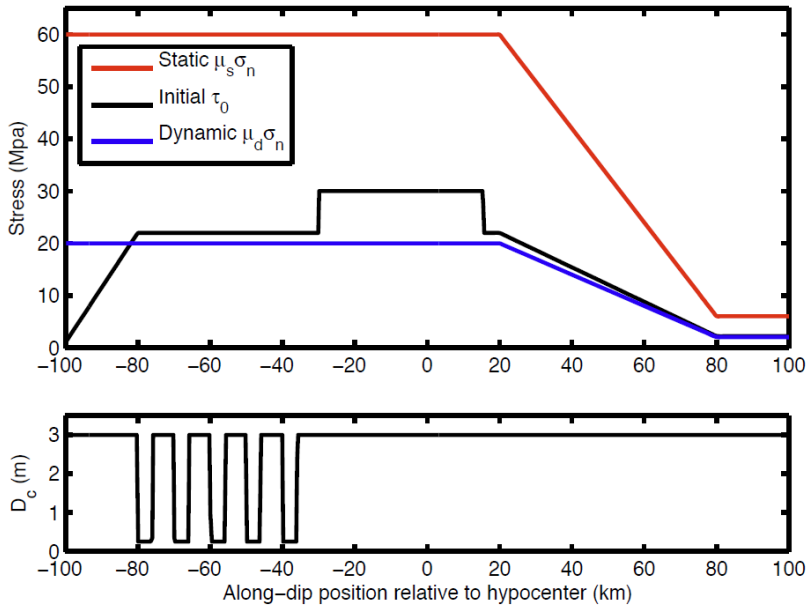

Figure 3.5: The along-dip distributions of initial shear stress, static strength, dynamic strength (top) and critical slip distance (bottom) in the first model.

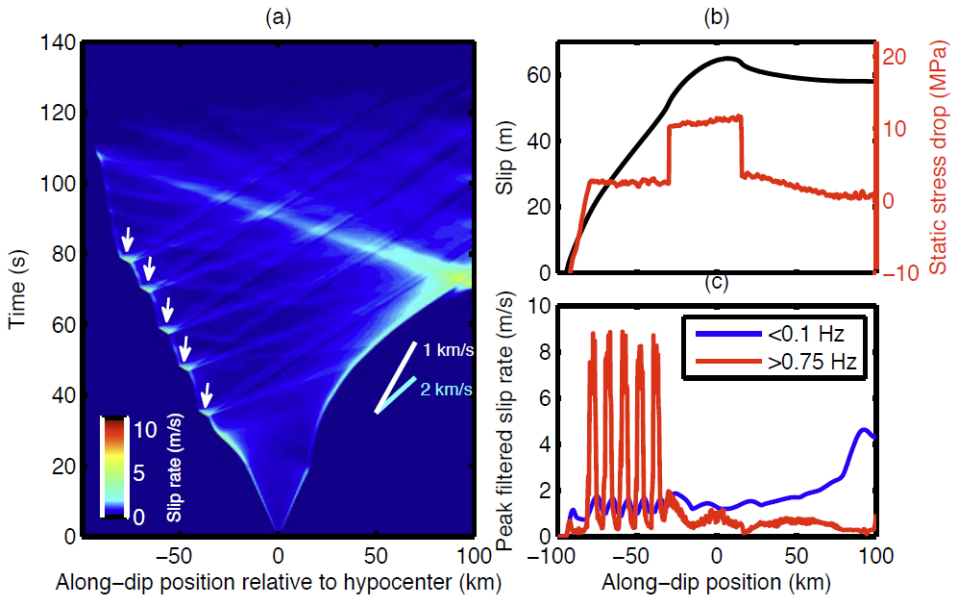

Figure 3.6: The spatial temporal distribution of slip rate (left), the along-dip distribution of final slip and static stress drop (top right), and the along-dip distribution of low-pass filtered (< 0.1 Hz) and high-pass filtered peak slip rates ($> 0.75\ Hz$) (bottom right) in the first model. The white arrows in the left figure denote the regions of high-frequency bursts.

2nd model (peak slip in hypocentral region)

In the second model, peak slip near the hypocenter indicates a larger stress drop there (Figure 3.7), which can promote rupture acceleration. Thus, we reduce the initial shear stress in the deep region to keep the rupture velocity as low as $1\ km/s$. We found that the steep decrease of slip from the hypocenter to the trench (Figure 3.1b) can only be achieved by a negative stress drop. This suggests that either the initial shear stress is lower or the dynamic friction coefficient is higher than in our first model. However, since the normal stress near the trench is very low and so is the dynamic strength, it is not possible to reduce the initial shear stress enough while keeping its sign consistent with thrust faulting. We hence increase the dynamic friction coefficient linearly in the shallow region, which produces a curved profile of dynamic strength (Figure 3.7). The resulting dynamic rupture (Figure 3.8a) is similar to our first rupture model, except for the shorter nucleation stage. The final slip distribution (Figure 3.8b) and high-frequency power ratio (Figure 3.8c) are also consistent with the observations.

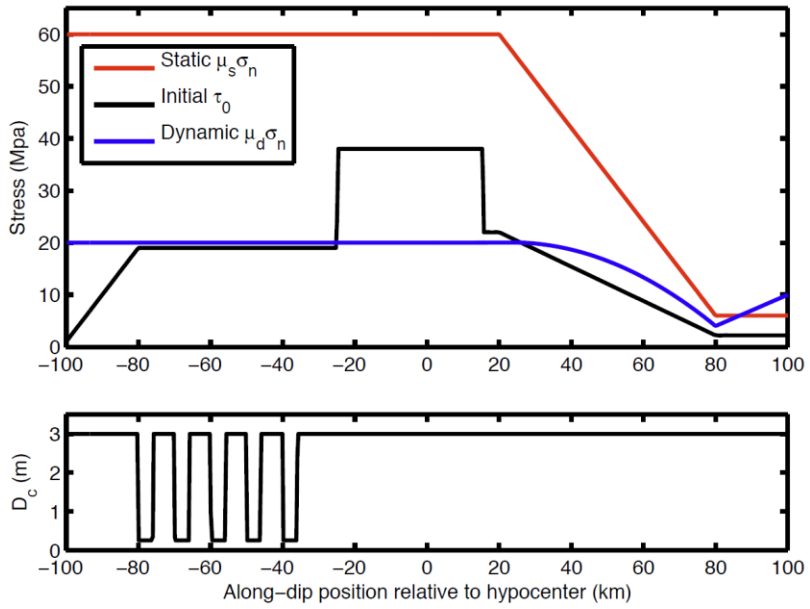

Figure 3.7: The along-dip distributions of initial shear stress, static strength, dynamic strength (top) and critical slip distance (bottom) in the second model.

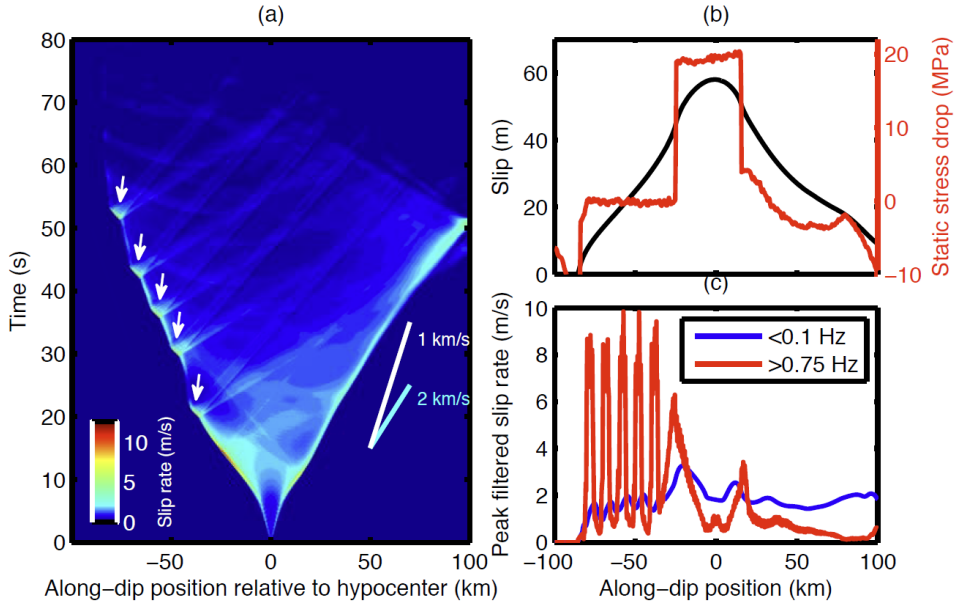

Figure 3.8: The spatial temporal distribution of slip rate (left), the along-dip distribution of final slip and static stress drop (top right), and the along-dip distribution of low-pass filtered (< 0.1 Hz) and high-pass filtered peak slip rates ($> 0.75\ Hz$) (bottom right) in the second model. The white arrows in the left figure denote the regions of high-frequency bursts.

3rd model (peak slip in shallow region)

The third model features peak slip between the hypocenter and the trench, as suggested by many slip inversion studies. In this model, the largest stress drop is located up-dip from the hypocenter and decreases in both directions along-dip. Because of the lower stress drop in the nucleation region compared to our previous two models, the static friction coefficient and D_c are reduced there to achieve rupture nucleation (Figure 3.9). Successful down-dip rupture requires the region with reduced D_c, which is as low as within the small asperities, to extend 40 km down-dip from the hypocenter. The small asperity located from 36 to 40 km down-dip from the hypocenter in the previous two models is hence not present in the third model. To avoid significant slowing down of the down-dip rupture, the value of D_c in between the small asperities is smaller than in the previous two cases. As large stress drop promotes high-frequency radiation, we also increase D_c in the shallow region. The details of the resulting rupture are shown in Figure 10a. The rupture reaches a down-dip speed of about 1 km/s and an up-dip speed of about 2 km/s. Again, the down-dip rupture generates much stronger high-frequency radiation than the up-dip rupture (Figure 3.10c).

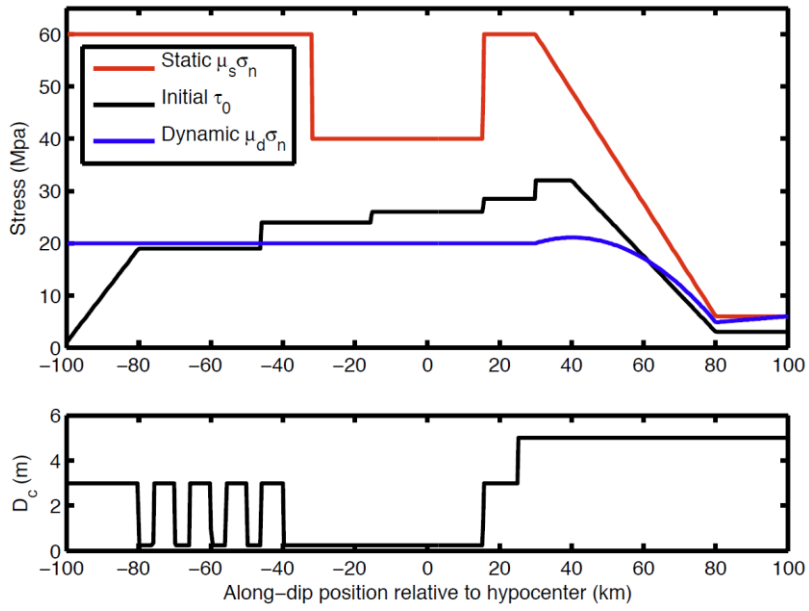

Figure 3.9: The along-dip distributions of initial shear stress, static strength, dynamic strength (top) and critical slip distance (bottom) in the third model.

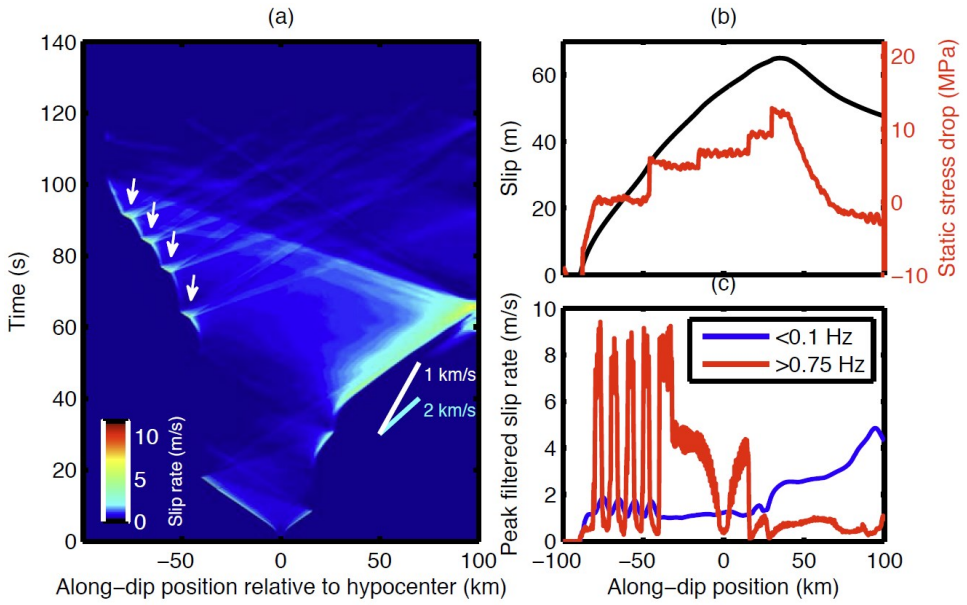

Figure 3.10: The spatial temporal distribution of slip rate (left), the along-dip distribution of final slip and static stress drop (top right), and the along-dip distribution of low-pass filtered ($< 0.1\,Hz$) and high-pass filtered peak slip rates ($> 0.75\,Hz$) (bottom right) in the third model. The white arrows in the left figure denote the regions of high-frequency bursts.

3.4 Constraints on Static Stress Drop, Fracture Energy and Energy Partitioning

Static stress drop

The average static stress drops inferred from different slip inversions of the Tohoku-Oki earthquake are 4.8 MPa [Koketsu et al., 2011], 6 MPa [Yagi and Fukahata, 2011] and 7 MPa [Lee et al., 2011], respectively. We compare these values to $\Delta\tau_E = \frac{\int \Delta\tau D ds}{\int D ds}$, the slip-weighted average of the static stress drop distributions obtained in our rupture models. This averaging procedure is appropriate for energy estimates [Noda and Lapusta, 2012]. The values of $\Delta\tau_E$ thus calculated for the three models are 4.5 MPa, 7 MPa and 4.6 MPa, similar to the average static stress drop inferred from slip inversions. Note that the static stress drop can vary in space by almost two orders of magnitude, e.g., from 12 MPa in the peak-slip region to 0.2 MPa near trench in the first model (Figure 3.6b). In the other two models the stress drop near the trench is negative but the overall stress drop is still positive (Figures 3.8b and 3.10b). The first and second models provide the two end members of the distributions of static stress drop in the Tohoku-Oki earthquake. In the first

model, the static stress drop in the shallow region is rather small and almost zero near the trench. The large stress drop around the hypocenter pushed the whole shallow region eastwards and the resulting slip is large but almost constant. This behavior is somewhat similar to block sliding. In contrast, the second model requires large negative stress drop in the shallow region. The large stress drop around the hypocenter still pushes the shallow region eastwards, but the final slip decreases due to the resistance caused by the larger dynamic friction prescribed there, resulting in the negative stress drop. The third model is similar except that the region with large stress drop is located eastward from the hypocenter.

The negative stress drops in the second and third models can result from velocity-strengthening materials in nature. The shallow velocity-strengthening region is usually considered as the upper limit of the seismogenic zone, defined as the zone where earthquakes can nucleate. Our numerical models show that ruptures can break through this region and result in a large slip there. Our models constrained by observed slip profiles (Figure 3.1) show that the velocity-strengthening region needs to reach at least 40 km down-dip from the trench, or even more than 70 km as suggested by the slip profiles from Lee et al. [2011] and Simons et al. [2011]. Usually the upper limit of the seismogenic zone on subduction megathrusts is at a depth of 5-15 km [Hyndman et al., 1997], or at an along-dip distance of 20-60 km given the subduction geometry in our models. However, the different in-situ pressures, temperatures and minerals make it hard to determine the upper limit of the seismogenic zone in specific subduction zones. Resolving this question in the Tohoku region requires a reliable identification of the interplate seismicity and determination of the coseismic slip profile of the Tohoku-Oki earthquake at shallow depth. While multiple observations point to large slip close to trench, whether they involve significant postseismic deformation is still an open question. Studies of early postseismic deformation are necessary to understand this better.

Fracture energy

A significant product of our models is the constraint on fracture energy or D_c in the shallow region. As discussed in Section 3.2, the back-projection frequency f_{bp} should be larger than the second corner frequency in the shallow region, which suggests:

$$D_c^S > \frac{(1-\nu)\Delta\tau_s^S v_R^S A(v_R)}{\mu f_{bp}} \tag{3.1}$$

For example, when $f_{bp} = 0.75\ Hz$, $\Delta\tau_s^s = 22.5\ MPa$ and $v_R^s = 2\ km/s$, we find $D_c^s > 1.9\ m$ in the first model. Thus, for a given D_c^d, we can find a D_c^s that satisfies the deep/shallow high-frequency power ratio (Appendix A) and the lower bound given by f_{bp} (Equation 3.1). Figure 3.11 summarizes the deep/shallow high-frequency slip-rate power ratio ($> 0.75\ Hz$) obtained in the first model for a range of values of fracture energy and D_c^s in a 80 km wide region, 20 km eastward from the hypocenter and beyond. This result shows that if $D_c^d = 0.25\ m$, D_c^s needs to be larger than $\sim 2.7\ m$, or the fracture energy larger than $\sim 60\ MJ/m^2$, in order to satisfy a high-frequency power ratio of at least 10. The large fracture energy in the shallow region also prohibits the acceleration of up-dip rupture, limiting the rupture speed to about 2 km/s except in the region near the trench where supershear rupture tends to occur.

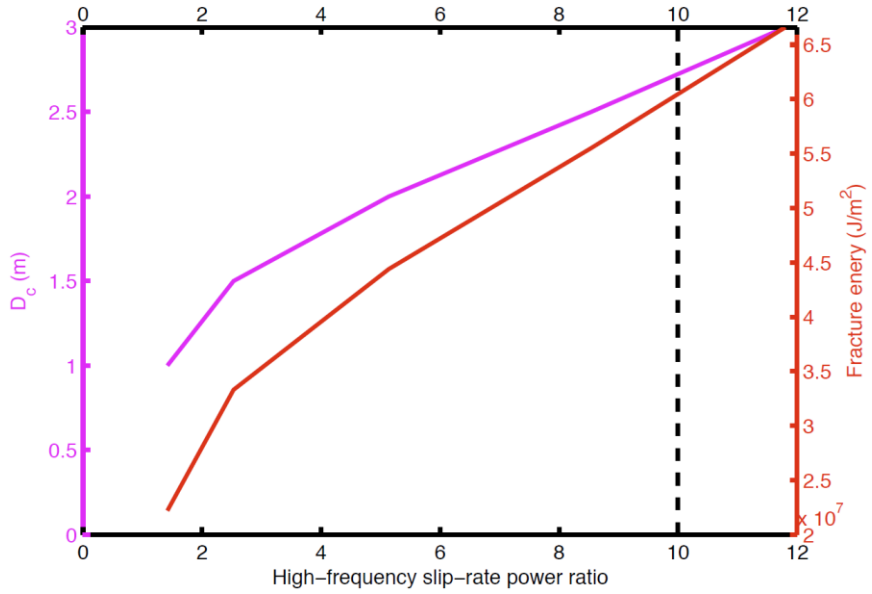

Figure 3.11: The high-frequency slip-rate power ratio for different values of D_c and fracture energy in an 80-km-wide region 20 km eastward from the hypocenter, when D_c in the deep region is kept at 0.25 m.

Energy partitioning

The nature of an earthquake is controlled by partitioning of energy between the radiated energy, E_R, and the fracture energy, E_G (which is the energy used for advancing the fracture against resistance at the fault tip). Depending on whether E_R/E_G is large or small, we expect rapid or slow earthquakes, respectively. (Here, rapid earthquake is an earthquake with strong seismic radiation,

and slow earthquake means an earthquake deficient in high frequency energy, like tsunami earthquakes.) We define the total available energy by $E_{T0} = E_R + E_G$, and call the ratio $\eta_R = E_R/E_{T0}$ the radiation efficiency [e.g., Kanamori and Rivera, 2006]. In seismology, we can directly determine E_R from observations. We cannot estimate the total available energy directly from seismic observations, but if the friction follows the simple slip-weakening curve and if overshoot or undershoot is not very large, we can approximate E_{T0} by $\Delta\tau DS/2$, where $\Delta\tau$ is stress drop, D is average slip and S is fault area.

We compare η_R estimated from seismological observations with that estimated from the dynamic models studied here. Using the relation for the total available energy, the radiation efficiency can be written as $\eta_R = \left(\frac{2\mu}{\Delta\tau}\right)\left(\frac{E_R}{M_0}\right)$ which can be estimated from the shear modulus μ, the stress drop $\Delta\tau$, the radiated energy E_R, and the moment M_0. We use the CMT moment $M_0 = 5.31 \times 10^{22}\ Nm$, which is determined at a depth of 20 km, and $\mu = 44.1\ GPa$ at this depth in PREM. The estimation of radiated energy by different investigators ranges from 3 to $9 \times 10^{17}\ J$ [Ide et al., 2011; Newman, written communication, 2011; Lay et al., 2012]. Then as the estimated stress drop varies from 4.8 MPa to 10 MPa [Koketsu et al., 2011; Lay et al., 2011; Lee et al., 2011; Yagi and Fukahata, 2011], the radiation efficiency η_R ranges from 0.05 to 0.31.

In the dynamic models, we can compute E_R and E_{T0} directly using the stress parameters and slip in the models:

$$E_{T0} = \frac{1}{2}\int_0^L \left(\tau_0(x) - \tau_1(x)\right) D(x)dx \tag{3.2}$$

$$E_R = E_{T0} - \int_0^L \left(\int_0^D \left(\tau\left(\widetilde{D}, x\right) - \tau_1(x)\right) d\widetilde{D}(x)\right) dx \tag{3.3}$$

where $\widetilde{D}$, D and $\tau_1$are the slip, final slip and final stress, respectively, at a given location x. The radiation efficiencies of the first, second and third models thus calculated are 0.33, 0.39 and 0.5, respectively. These values are higher than current seismological estimates of η_R. Including energy dissipation mechanisms such as off-fault plasticity may help reduce the radiation efficiency [Ma, 2013], but it can also diminish the final slip near the trench. Considering the many assumptions we made for our dynamic models (2-dimensionality and the specific dissipation mechanism) and the uncertainties in the seismological parameters, we consider the values of η_R to be in agreement only

approximately. Our objective here is to illustrate how dynamic models can be compared with the real earthquake through energy partitioning. As seismological methodology improves, we expect the uncertainties in seismological parameters to decrease significantly. Also, incorporating more realistic 3-dimensional structure and fault zone constitutive laws in dynamic modeling may eventually enable more meaningful comparisons between the physical models and real earthquakes. What is presented here is an illustration of how to make such comparisons.

Effects of the subduction wedge

One unexpected feature of the Tohoku-Oki earthquake is its propagation to the shallow region and the resulting large slip. To find how the subduction wedge (the structure between free surface and plate interface) with shallow dipping angle can affect the rupture propagation, we first compare our results to a rupture simulation on a fault with a dip angle of 90^o. The hypocenter is 100 km deep, and model parameters are the same as those prescribed in the first model (Figure 3.5). We find that on the vertical fault the rupture stops when it reaches the region with small stress drop at ~ 27.5 km upward from the hypocenter. In contrast, the up-dip rupture reaches the trench in our models of shallow dipping fault. This indicates that without the subduction wedge the rupture is unable to propagate to the shallow region, unless stress drop is increased or fracture energy is reduced there.

We also run a rupture simulation on a horizontal fault at a depth of 25 km (the hypocentral depth in our models of the Tohoku-Oki earthquake) from the free surface. Given the same model parameters, we find that the rupture can propagate as far as where the trench would be (100 km eastward from the hypocenter). This shows that the effect of the free surface enables rupture to the trench despite the small stress drop in the shallow region. The structure of the subduction wedge is even more favorable for rupture propagation as the shallow region is closer to the free surface than the hypocenter is. Waves reflected by the free surface induce transient reduction of normal stress and increase of shear stress on the fault that lead to large transient stress drop [Kozdon and Dunham, 2013], which promotes the rupture propagation.

Our assumed fault geometry is simplified with a constant dip angle of 14^o, while the real plate interface starts at a much smaller angle 4.6^o [Kimura et al., 2012] and steepens with depth. As the subduction wedge can amplify the final slip, the real stress drop in the region near trench needs to be much smaller than in our models. The subduction wedge also leads to rupture acceleration, which produces high-frequency radiation. This effect is expected to be stronger in a subduction

wedge with smaller dipping angle. Thus, fracture energy (or D_c) may also need to be larger in order to inhibit the high-frequency radiation in the shallow region. Our models provide an upper bound for the average stress drop and a lower bound for the fracture energy in the shallow region.

3.5 Conclusions

We presented dynamic rupture models of the Tohoku-Oki earthquake by integrating key observational constraints. We assume a fault governed by slip-weakening friction, with asperities of different frictional properties, and use the final slip distribution and the high-frequency radiation to constrain the stress drop and D_c. We use three models to reproduce the three typical along-dip slip profiles obtained by finite fault source inversions. Rupture properties estimated by our dynamic modeling such as rupture velocity and slip rate are consistent with the observations, though variations do exist in different models. Overall, in our models the average static stress drop of the event is in the range of 4.5 MPa to 7 MPa, and fracture energy in the shallow region is in the order of 10 MJ/m^2. Stress drop reaches values of order 10 MPa in the regions of maximum slip, as also suggested by slip inversions [Yagi and Fukahata, 2011]. The coseismic slip distributions constrain the size of the shallow region of negative stress drop, which can be associated with strengthening materials that delineate the upper limit of the seismogenic zone. We find that the radiation efficiency computed for our models is larger than 0.3, somewhat larger than that inferred from seismic data. This may indicate that additional forms of energy dissipation are needed.

C h a p t e r 4

PULSE-LIKE RUPTURES INDUCED BY LOW-VELOCITY FAULT ZONES

Huang, Y. and J.-P. Ampuero (2011), Pulse-like ruptures induced by low-velocity fault zones. Journal of Geophysical Research, 116, B12307, doi: 10.1029/2011JB008684.

Supplementary materials are included in Appendix B.

Low-velocity fault zones (LVFZ) are found in most mature faults. They are usually 100-400 m wide and have ~20%-60% wave velocity reductions relative to the country rock. To study the effect of LVFZs on earthquake rupture and the radiated wavefield, we conducted 2D simulations of dynamic rupture on faults that bisect an LVFZ, considering a range of velocity reductions and widths. Most earthquakes apparently have slip rise times much shorter than their overall rupture duration. A number of dynamic mechanisms for such pulse-like ruptures have been proposed, including frictional self-healing, fault strength heterogeneities and bimaterial effects. We find that ruptures in LVFZs with strong enough wave velocity contrast behave as pulses. These pulses are generated by fault locking induced by waves reflected from the boundaries of the LVFZ. This mechanism of pulse generation is robust to variations of initial stress, smoothness of the LVFZ structure, rupture mode and exclusion of frictional healing. Moreover, we find that LVFZs can generate complex rupture patterns. LVFZs with low velocity reduction induce multiple rupture fronts involving co-existing pulses and cracks. LVFZs with certain widths can accelerate the transition to supershear rupture speed. These additional effects of LVFZs on dynamic rupture can contribute to the complexity of high-frequency ground motions.

4.1 Introduction

Faults are usually surrounded by damaged rocks that are more compliant and have lower seismic wave velocities than the country rock. The properties of such low-velocity fault zones (LVFZ) have been widely studied in different areas such as the San Andreas [Li and Leary, 1990; Li et al., 2006; Lewis and Ben-Zion, 2010], San Jacinto [Lewis et al., 2005; Yang and Zhu, 2010], Landers [Li et al., 1994; Peng et al., 2003; Li et al., 2007], Hector Mine [Li et al., 2002], Calico [Cochran et al., 2009; Yang et al., 2011], Nojima [Mizuno et al., 2008] and North Anatolian [Ben-Zion et al., 2003]

fault zones. Travel times and waveform attributes of fault zone trapped waves and head waves can be exploited to determine the seismic wave velocity reduction and the width of the LVFZ, although there are trade-offs between these two properties. LVFZs usually have a width of 100-400 m (e.g., ~200 m in the San Andreas fault, ~300 m in the Landers fault), although some are much wider (e.g. ~1.5 km in the Calico fault). The velocity reductions within the LVFZ, relative to the country rock, vary in the range of 20%-60%. The borehole data of the SAFOD drilling project reveals similar fault zone structures with a ~200 m LVFZ and velocity reduction of ~25% at the depth of ~3.2 km [Hickman et al., 2005]. The Hirabayashi borehole across the Nojima fault also shows a velocity reduction of ~40% for P waves and ~60% for S waves at a depth of ~630 m (Figure 4.1).

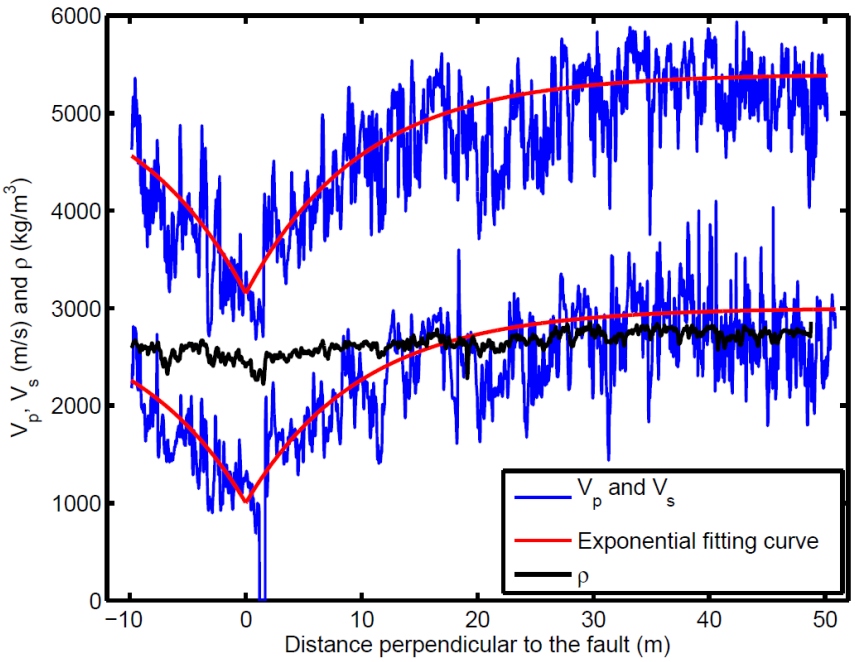

Figure 4.1: P wave speed, S wave speed and density from a log in the Hirabayashi borehole crossing the Nojima Fault Zone, Japan, at about 630 m depth (data courtesy from Hisao Ito). The red curves are exponential distributions.

In kinematic source models inferred from seismological and geodetic data the rise time, i.e. the duration of slip at a given fault location, is generally much shorter than the whole earthquake duration and than the wave travel time across the seismogenic thickness [Heaton, 1990; Beroza and Mikumo, 1996]. This is in contrast to the long rise times produced by classical crack models of

earthquake dynamics, like those that assume slip-weakening friction and homogeneous media [Andrews, 1976]. Many mechanisms for the generation of short-duration slip pulses are known: self-healing under velocity-dependent friction [Perrin et al., 1995; Beeler and Tullis, 1996, Zheng and Rice, 1998], the generation of healing phases by heterogeneities of strength or initial stress on the fault [Beroza and Mikumo, 1996; Oglesby and Day, 2002; Aagaard and Heaton, 2008] or by the boundaries of the seismogenic fault region [Day, 1982a], and dynamic changes of normal stress induced by bi-material effects [Andrews and Ben-Zion, 1997; Cochard and Rice, 2000; Shi and Ben-Zion, 2006; Rubin and Ampuero, 2007; Ampuero and Ben-Zion, 2008].

When an earthquake breaks in a fault embedded in an LVFZ, the trapped waves can alter the shear stress on the fault plane and affect the dynamic rupture process. Harris and Day [1997] studied dynamic ruptures on planar faults that bisect 100 to 4000 m wide LVFZs with 17% and 33% velocity reductions relative to the country rock. In their simulations based on slip weakening friction, the arrival of waves reflected from the edge of the LVFZ produced a complex pattern of slip rate. Others have studied earthquake nucleation, dynamic rupture and earthquake cycles on LVFZs [Ampuero et al., 2002; Ben-Zion and Huang, 2002; Brietzke and Ben-Zion, 2006; Kaneko et al., 2011]. None of these previous studies found the LVFZ to induce slip pulses, except when bimaterial effects were at play.

An extremely compliant LVFZ is equivalent to an elastic slab of finite thickness with fixed displacement boundary conditions. In such configuration analytical solutions of steady state rupture have exponentially decaying slip rate behind the rupture front, behaving practically like pulses [Broberg, 1999]. This conceptual end-member case suggests that a highly damaged LVFZ (perhaps more than in previous studies) might favor pulse-like rupture. Given the existence of an LVFZ in most mature faults, it seems natural to further investigate if it can contribute to short rise times. Here we performed dynamic simulations of 2D inplane rupture on slip-weakening faults that bisect an LVFZ. Our model assumptions and methods are described in Section 4.2. We show, in Section 4.3, that the reflected waves in an LVFZ with low enough velocities indeed provide an efficient mechanism for the generation of pulse-like ruptures. We further analyze the influence of the velocity reduction and width of the LVFZ on the rupture process. We also show the robustness of our findings with respect to variations in the model, namely the effects of the initial stress, of the smoothness of the velocity distribution within the LVFZ, of mode III rupture and of frictional

healing. In Section 4.4, we discuss the properties of slip pulses in an LVFZ and their potential effects on ground motions.

4.2 Model Setup

We consider a planar fault that bisects an LVFZ of finite width W embedded in an infinite medium (Figure 4.2). We consider this symmetric problem to avoid the interference between two mechanisms that can generate short rise times: dynamic changes of normal stress in asymmetric configurations [Harris and Day, 1997; Ben-Zion and Huang, 2002; Brietzke and Ben-Zion, 2006] and unloading shear stresses from reflected waves. Our paper focuses on the latter mechanism. Both the LVFZ and the country rock are linear elastic isotropic materials. We performed simulations with different wave velocity reductions inside the LVFZ while assuming uniform density and Poisson's ratio. We define the relative velocity reduction as $\Delta v = 1 - v_{lvfz} / v_{country}$.

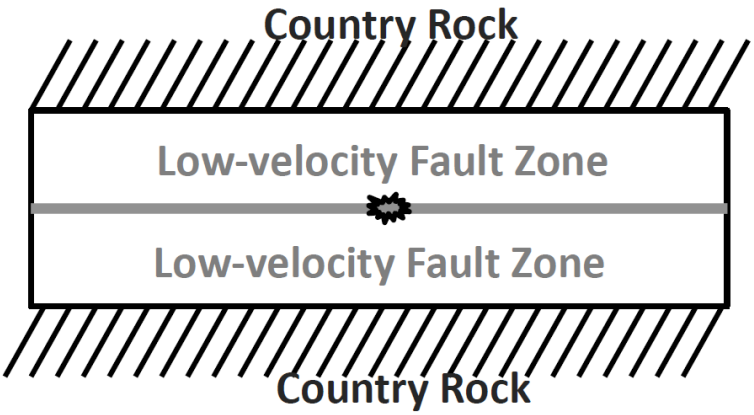

Figure 4.2: Model setup of 2D dynamic rupture on a fault bisecting a low velocity fault zone (LVFZ).

We assume a modified slip-weakening friction law, which combines linear slip-weakening friction and instantaneous healing, in order to exclude the mechanism of pulse generation that operates under more realistic velocity-dependent friction laws even without an LVFZ [Perrin et al., 1995; Beeler and Tullis, 1996, Zheng and Rice, 1998]. In the linear slip-weakening friction law [Andrews, 1976], the friction coefficient μ is a function of cumulative slip D :

$$\mu = \max\left\{\mu_d, \mu_s - (\mu_s - \mu_d) D / D_c\right\} \tag{4.1}$$

where μ_d is the dynamic friction coefficient, μ_s the static friction coefficient and D_c the critical slip. The static and dynamic friction coefficients in our simulations are 0.6 and 0.1 respectively. This low value of dynamic friction is consistent with the lack of heat flux anomaly on the San Andreas Fault [Kanamori et al., 2000; Boullier et al., 2001; Kano et al., 2006]. In our assumed instantaneous healing mechanism, the friction coefficient is locally reset to its initial value as soon as slip stops (in practice, if slip rate becomes smaller than a very small value). We will discuss in Section 4.3.7 how the results differ if the fault remains at the dynamic strength level.

We artificially initiate ruptures by imposing a time-weakening nucleation zone that expands at constant speed [Andrews, 1985], one quarter of the S wave speed of the country rock. The rupture starts propagating spontaneously when it reaches a certain critical size. Shortly after, the nucleation procedure is removed and the friction coefficient is allowed to heal. The prescribed nucleation speed is slow enough to avoid abrupt perturbations on dynamic rupture and fast enough to allow efficient computations. Selected simulations with much slower nucleation produced similar results during spontaneous rupture growth. Simulations initiated by an overstressed region, a more abrupt nucleation procedure, produced short rise times more systematically, reinforcing our main result described in Section 4.3. For a given initial shear stress, we found the critical size for spontaneous rupture to be rather independent of the LVFZ width. Indeed, for the relatively low initial stress levels and narrow LVFZs considered here, the critical size is expected to be more sensitive to the country rock.

We solve the dynamic rupture problem in 2D plane strain (Figure 4.2) using a spectral element method [SEM2DPACK, Ampuero, 2009]. We verified the code on a 2D version of the SCEC TPV3 benchmark problem [Harris et al., 2009]. We found that the SEM has the same convergence rate as the DFM [Day, 1982b; Rojas et al., 2008]. We also verified the numerical convergence of the SEM in problems involving an LVFZ. We discuss the benchmark and convergence tests in the appendices. In all the simulations reported here we set, by trial and error, a spectral element size small enough to sample the process zone with more than three Gauss-Lobatto-Legendre nodes.

In order to apply our results to a wide range of material properties, we adopt dimensionless quantities for slip, space, time, slip rate and stress:

$$D^* = D / D_c \tag{4.2}$$

$$x^* = x/L_c \tag{4.3}$$

$$t^* = tv_s/L_c \tag{4.4}$$

$$(V)^* = VL_c/D_c v_s \tag{4.5}$$

$$\sigma^* = \sigma/\Delta\tau_s \tag{4.6}$$

where $\Delta\tau_s = \sigma_0(\mu_s - \mu_d)$, $L_c = GD_c / \Delta\tau_s$, G is shear modulus, and v_s is S wave velocity. The normalized density, critical slip and shear modulus are all 1. As a result, the normalized S wave speed and P wave speed are 1 and 1.732 respectively. The normalized normal stress is 2. We quantify the initial stress level by the non-dimensional relative strength parameter S defined by Das and Aki [1977a] as the ratio of initial strength excess to stress drop: $S = (\mu_s - \mu_0)/(\mu_0 - \mu_d)$.

4.3 Results

4.3.1 Low Velocity Fault Zones Can Induce Pulse-Like Ruptures

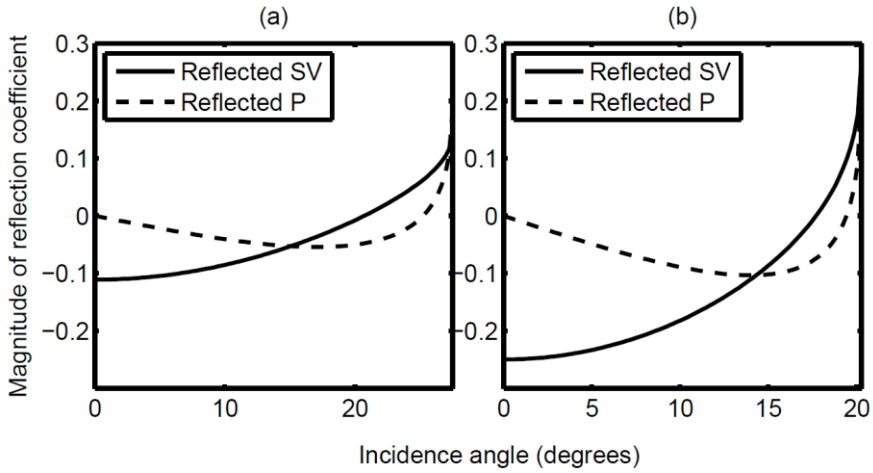

Figure 4.3: Reflection coefficients for incident SV waves at the boundary between country rock and LVFZs with velocity reductions of (a) 20% and (b) 40% respectively, as a function of incidence angle. Incidence is from the LVFZ. Both P and SV reflected waves are considered. The incident angles of SV waves are plotted below the first critical angle. The phase is zero for this range of incident angles. Formulas of reflection coefficients are taken from Aki and Richards [2002].

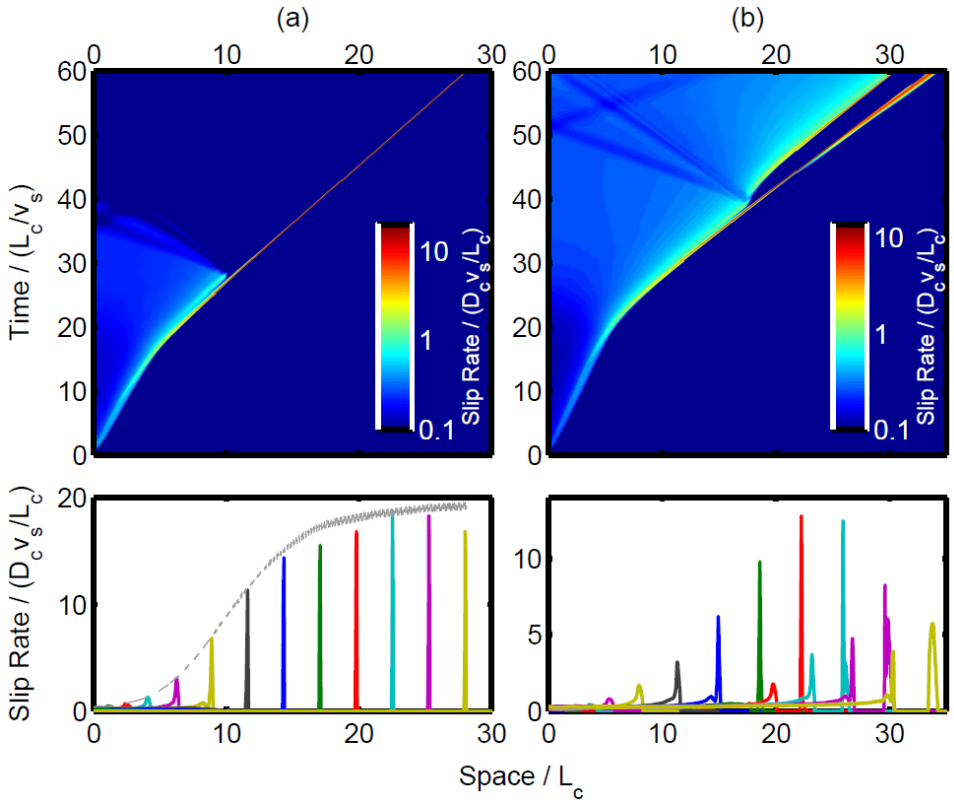

Figure 4.4: Spatio-temporal distributions of slip rate (top) and its spatial distributions at time intervals of 5 for LVFZs of width 1 with velocity reductions of (a) 40% and (b) 20%. In both simulations the S ratio is 2.33.

The amplitude of a wave reflected back to the fault from the boundary of an LVFZ has sign opposite to that of the incident wave for a certain range of incidence angles (Figure 4.3). Thus, it is conceivable that under certain conditions the reflected wave can unload the fault and heal the rupture, generating a slip pulse. Figure 4.4a shows the spatial-temporal distribution of slip rate in a simulation with $W = 1$ and $S = 2.33$. The rupture starts as a crack, which is the expected behavior for slip-weakening models in homogeneous media. However, at a certain distance a back-propagating healing front emerges spontaneously. This feature is similar to the stopping phase that would arise from the abrupt arrest of a crack, but we note that the simulation does not contain any stopping barrier. Subsequently, the rupture transforms into a pulse and continues propagating. The pulse soon reaches steady state. Its rise time (~0.3) is comparable to the travel time of P and S waves across the LVFZ. Its rupture speed is close to the Rayleigh wave speed of the LVFZ. The peak slip rate increases during the initial crack-like propagation and becomes stable once the rupture becomes a steady state pulse.

In the following sections we assess the robustness of the pulse generation mechanism illustrated by this example, by exploring how the rupture style is affected by the wave speed in the LVFZ, the width of the LVFZ and the initial stress. The main effects on rupture speed and style are summarized in Figure 4.6. We further consider variations about the basic model, including a smoother distribution of wave speed in the LVFZ, rupture in mode III and exclusion of frictional healing.

4.3.2 Effect of the Velocity Reduction in the LVFZ.

The velocity reduction in natural LVFZs typically ranges from 20% to 60%. We conducted simulations with a range of velocity reductions (Δv = 0.2, 0.3, 0.4 and 0.5) and found pulses in all cases. The pulse emerges sooner in LVFZs with larger Δv , as expected due to their larger reflection coefficients inducing unloading reflected waves of higher amplitude (Figure 4.3). We found, however, distinct rupture styles and speeds at high and low Δv . For Δv = 0.4 and 0.5 ruptures eventually propagate as pure pulses (Figure 4.4a) with speed approaching the Rayleigh wave speed of the LVFZ material (hereafter called "LVFZ Rayleigh"). Their short rise time (~0.3 for Δv = 0.4 and ~0.35 for Δv = 0.5) is comparable to the wave travel time across the LVFZ. Slip and slip rate are larger in the case with higher wave speed reduction. For Δv = 0.2 and 0.3 ruptures feature a pulse followed by a crack (Figure 4.4b). Their rupture speed eventually approaches the Rayleigh speed of the country rock (hereafter called "country Rayleigh"). The peak slip rate increases during the initial crack-like propagation but decreases to a much lower level after the onset of the country-Rayleigh pulses. While these pulses are supershear with respect to the LVFZ material, they are not generated by the Burridge-Andrews mechanism, which requires high initial shear stress [Andrews, 1976], but by the multiple reflected waves from the boundary of the LVFZ. Their rise time (~1.5 for Δv = 0.2 and ~2 for Δv = 0.3) is much longer than for the LVFZ-Rayleigh pulses.

4.3.3 Effect of the LVFZ Width

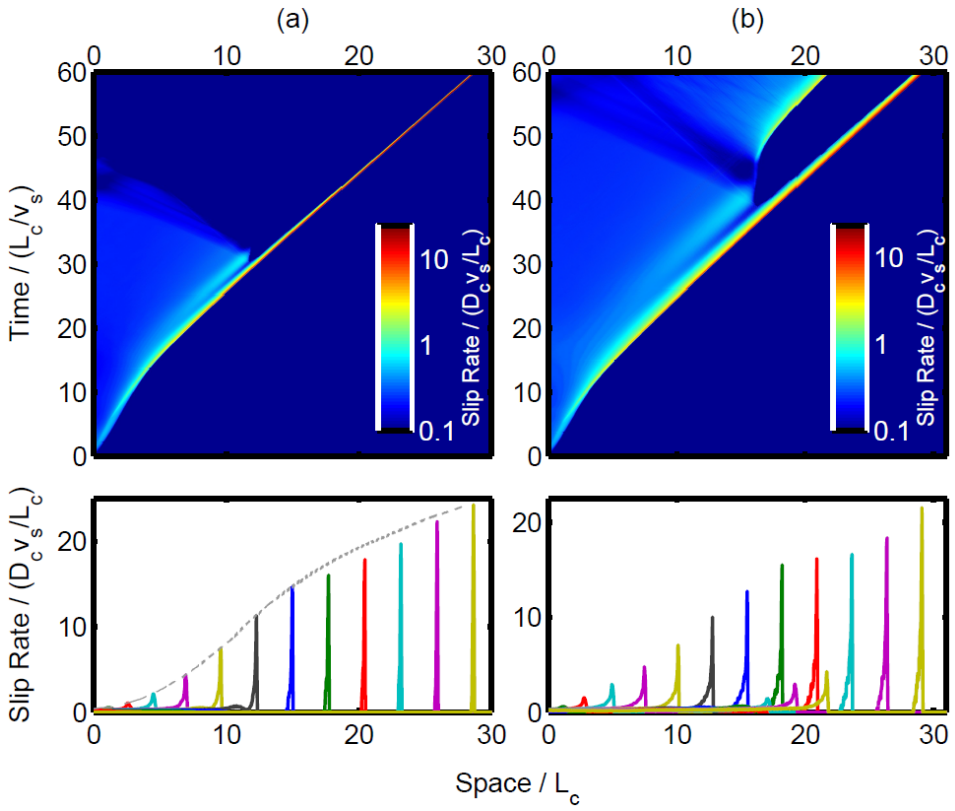

Figure 4.5: Slip rate (same representation as in Figure 4.4) for S ratio of 2.33 and LVFZs with velocity reduction of 40%. The LVFZ widths are (a) 2 and (b) 4 respectively.

We explored the effect of the LVFZ width by varying W from 1 to 4, while keeping all the other parameters the same as in our previous simulations. For an LVFZ of $\Delta v = 0.4$, the rupture speed stays at LVFZ-Rayleigh level, while the rupture style changes. When W = 1 and 2, the rupture starts as a crack and later transforms into an LVFZ-Rayleigh pulse (Figures 4.4a and 4.5a). When W = 4, pulses and cracks coexist simultaneously: the pulse is followed by a crack (Figure 4.5b). For wider LVFZs the onset of pulse-like rupture happens later; the pulses reach steady state later and their rise time at steady state is roughly proportional to W. These observations are consistent with the proportionality between W and the travel time of the fault zone reflected waves. Figure 4.6a summarizes the effects of the velocity and width of LVFZs on the rupture style and rupture speed.

4.3.4 Effect of Initial Stress and LVFZ Width on Rupture Speed

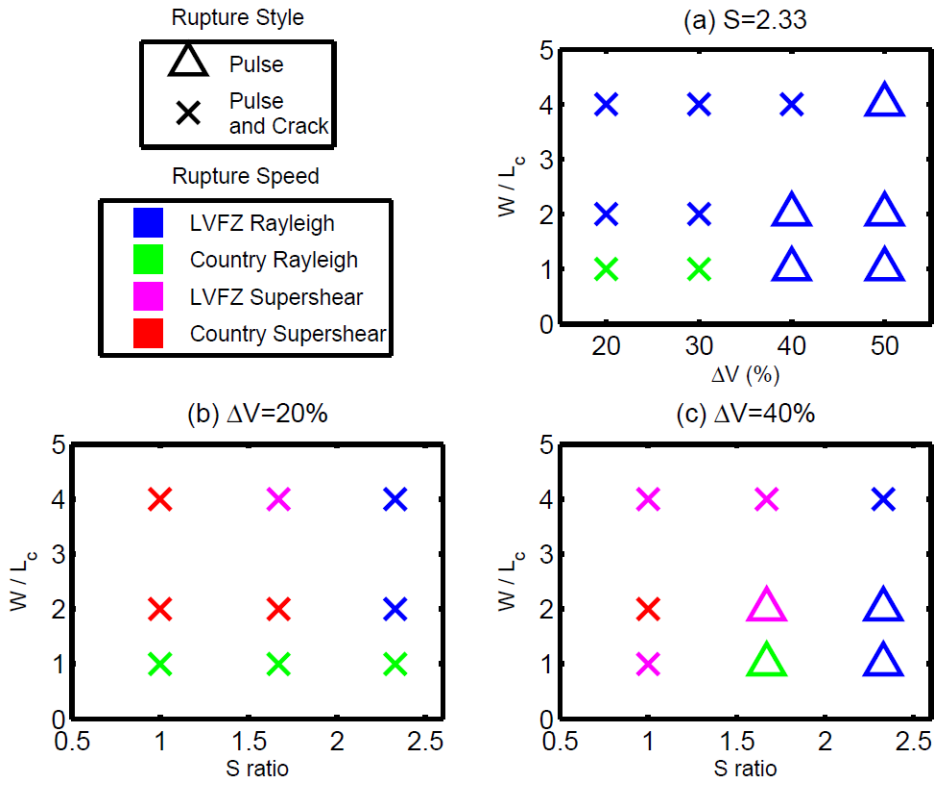

Figure 4.6: Summary of rupture style and rupture speed (a) as a function of velocity reduction and LVFZ width for S ratio of 2.33, and as a function of S ratio and LVFZ width for velocity reductions of (b) 20% and (c) 40%.

In a 2D homogeneous medium, ruptures can run at supershear speed only if $S < 1.77$ [Andrews, 1985]. As expected, when $S = 2.33$ we observed only subshear ruptures, LVFZ Rayleigh or country Rayleigh. When $S = 1.67$ we observe a range of rupture speeds on LVFZs with $\Delta v = 0.2$ (Figure 4.6b). When $W = 1$ the rupture runs faster than the S wave speed of the LVFZ, approaching the country Rayleigh speed (Figure 4.7a). When $W = 2$ the rupture undergoes the transition from LVFZ Rayleigh to supershear speed relative to the country rock, faster than the P wave of the LVFZ (hereafter called "country supershear"). When $W = 4$ the rupture speed approaches the P wave speed of the LVFZ (hereafter called "LVFZ supershear"). When $W = 8$ (not shown here) the rupture speed is near the LVFZ Rayleigh. The distance at which the supershear

transition would happen in a homogeneous medium when $S = 1.67$ is much larger than the size of our simulation domain. Hence, for a certain range of LVFZ widths we find that the presence of the LVFZ allows the supershear transition to happen sooner than expected. This phenomenon is also present in the simulations of Harris and Day [1997]. We observe similar effects when $\Delta v = 0.4$ (Figure 4.6c). In addition, LVFZs of $\Delta v = 0.4$ still favor pure pulse-like rupture for $W = 1$ (Figure 4.7b) and 2. When $S = 1$ the supershear transition happens very early and the effect of the LVFZ is less marked. Biegel et al., [2008] also found a dependence of rupture speed on the damaged zone width in laboratory experiments, with a transition from country-Rayleigh to LVFZ-Rayleigh as a function of W. Some of their experiments ran significantly slower than the LVFZ-Rayleigh speed, which they attributed to anelastic dissipation in the damaged zone, a mechanism ignored in our simulations.

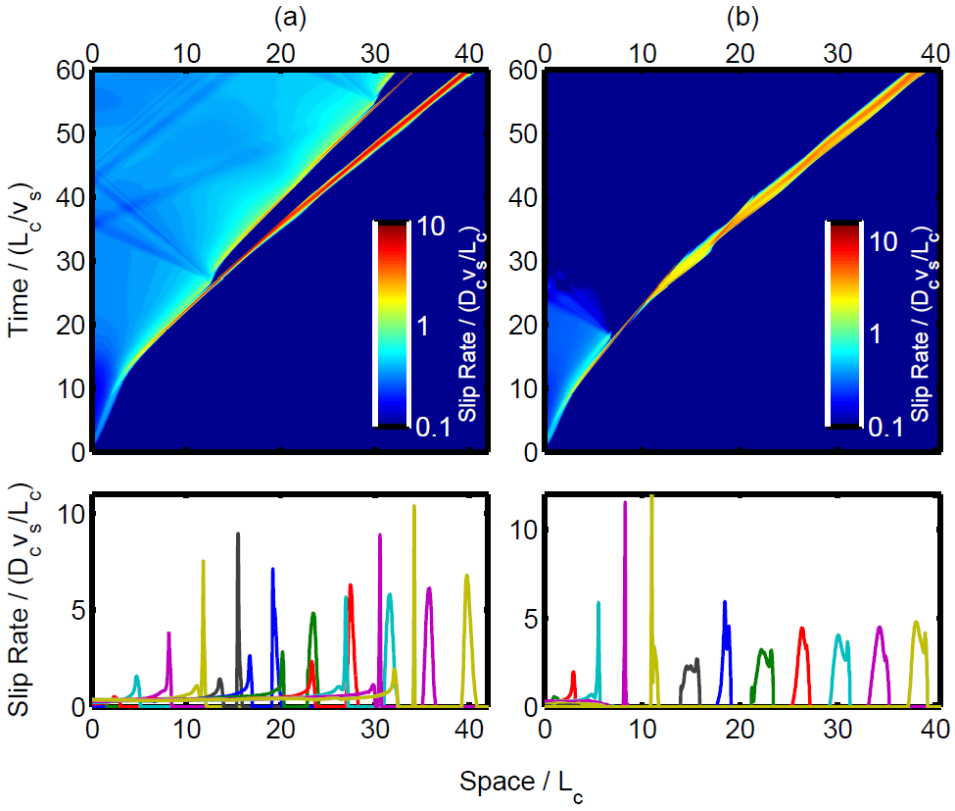

Figure 4.7: Slip rate (same representation as in Figure 4.4) for S ratio of 1.67 and LVFZs of width 1 with velocity reductions of (a) 20% and (b) 40%.

4.3.5 Effect of the Smoothness of the LVFZ Structure

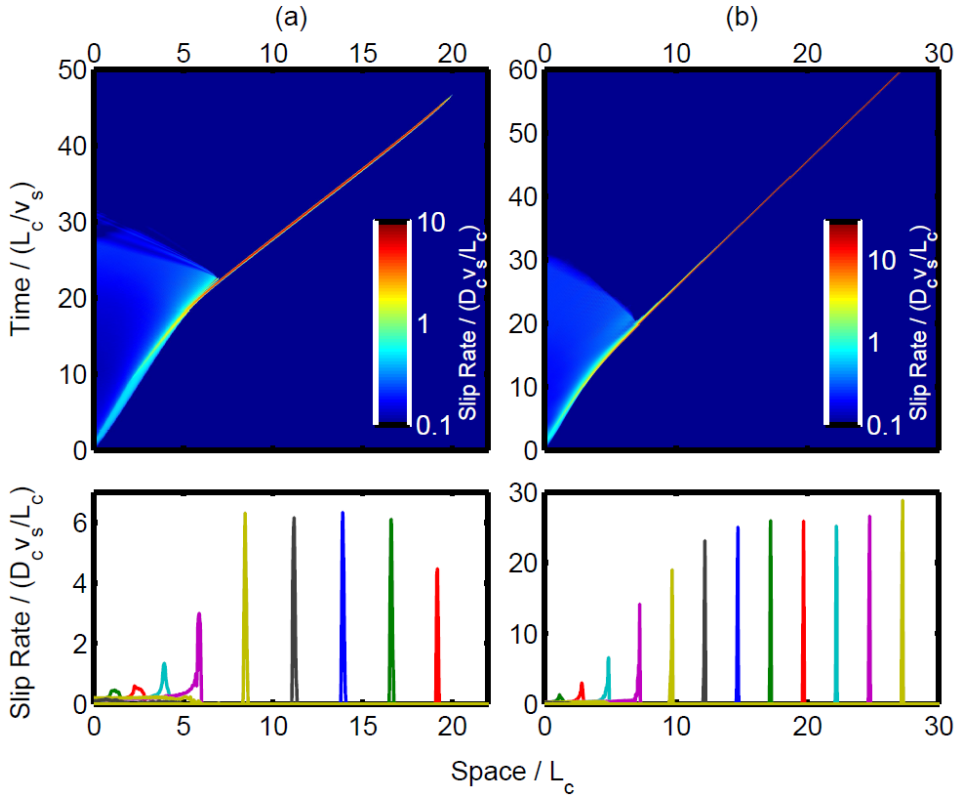

Figure 4.8: (a) Slip rate (same representation as in Figure 4.4) for S ratio of 2.33 and LVFZ with exponential distribution of wave speeds in inplane mode. The LVFZ is 1 wide with maximum velocity reduction of 60%. (b) Slip rate (same representation as in Figure 4.4) for S ratio of 2.33 and LVFZ of width 1 with velocity reduction of 50% in antiplane mode.

Wave velocities do not necessarily change abruptly inside natural LVFZs but rather decrease progressively as exemplified by the Nojima Fault Zone seismic log (Figure 4.1). A smoother LVFZ structure is expected to be less efficient at reflecting and trapping waves than an LVFZ with abrupt velocity contrasts. To assess how the smoothness of the LVFZ structure competes with the pulse generation mechanism, we consider an LVFZ with an exponential distribution of wave speeds as a function of distance z to the fault plane: $v(z) = v_0(1-\Delta v \exp(-5z/W))$, where v_0 is the country rock velocity, Δv is the relative velocity change and W is the width of the zone where more than 92% of the total velocity reduction is achieved, i.e. $(v(W/2)-v(0))/v_0 \sim 0.92\Delta v$. We found that simulations with $W = 1$ and $\Delta v = 0.4$, 0.5 and 0.6 can still produce pulses. Their rupture speed

increases as Δv decreases and remains higher than the lowest S wave speed inside the LVFZ but lower than the country Rayleigh speed. As Δv increases, the ruptures behave in a more pulse-like than crack-like fashion. For Δv = 0.6 (Figure 4.8a), a pure pulse with an average rise time of ~0.5 eventually emerges, leaving a dying crack behind. Interestingly, after some propagation distance the pulse stops spontaneously.

4.3.6 Effect of the Rupture Mode

Our study has considered so far the inplane rupture mode (mode II), relevant to along-strike rupture propagation on strike-slip faults or to along-dip propagation on dip-slip faults. We found that antiplane rupture (mode III) in an LVFZ with Δv = 0.5 and W = 1 (Figure 4.8b) has a similar behavior as inplane rupture (mode II): an initial crack stops after spawning a pulse. In this case the pulse propagates at almost the S wave speed of the LVFZ and its rise time (~0.3) is comparable to the travel time of SH waves inside the LVFZ. This proves that the generation of slip pulse does not necessarily require the conversion between P and S waves.

4.3.7 Effect of Frictional Healing

The rate of fault strength recovery immediately after slip arrest, over timescales shorter than the rupture duration, still lacks constraints from observations and laboratory experiments. In our previous simulations we considered the end-member model of instantaneous healing, in which the friction coefficient recovers to its static value immediately after slip arrest. We consider now the opposite end-member model, in which frictional healing is absent (or extremely slow at coseismic timescales). Assuming that the friction coefficient remains at its dynamic level even after slip arrest, we found that the rupture in an LVFZ with Δv = 0.4 and W = 1 (Figure 4.9a) propagates as a pulse followed by multiple cracks with much lower slip rates. The rupture speed experiences a transition from LVFZ Rayleigh to the country Rayleigh speed.

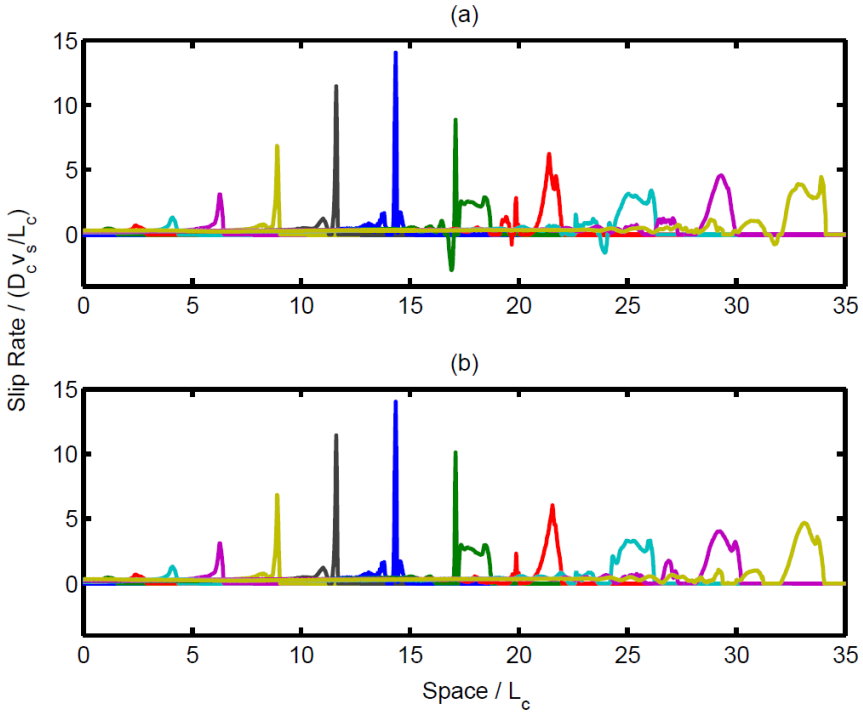

Figure 4.9: Spatial distributions of slip rate at time intervals of 5 for S ratio of 2.33 and LVFZs of width 1 with velocity reduction of 40%. The dynamic friction coefficients are (a) 0.1 and (b) 0.3 respectively. Both simulations are without frictional healing.

Interestingly, this example features negative slip rates, i.e. in the direction opposite to the main slip direction. Indeed, the reflected waves can drop the fault shear stress to negative values and, if the fault does not heal instantaneously, the stress can reach the dynamic strength again but with opposite sign. The fault can then slip backwards until the stress rises up again once the reflected waves are past. The low dynamic friction coefficient assumed here (0.1) is consistent with the absence of large frictional heat produced by narrow principal slip zones in many natural faults [e.g. Kanamori and Heaton, 2000; Boullier et al., 2000; Kano et al., 2006]. However, the possibility of wide slip zones and high dynamic friction cannot be excluded. In a simulation with dynamic friction of 0.3, keeping the same stress drop and strength drop as previously, the negative shear stress is no longer large enough to reach the dynamic strength (Figure 4.9b). Thus, the fault does not slip backwards if the dynamic fault strength is high enough. Overall, these two simulations with low and high friction yield very similar ruptures. The reverse slip rate remains a small-scale feature. Given the resolution limitations of current seismic source inversions, obtaining seismological evidence of reverse slip rates in natural earthquakes is challenging.

4.4 Discussion

4.4.1 Correlation between LVFZ and Short Rise Time

Source inversion studies inferred very short rise time (~0.3 s) from the strong motion data of the Morgan Hill earthquake [Hartzell and Heaton, 1986; Beroza and Spudich, 1988]. According to the relation (rise time) = (seismogenic thickness) ÷ (2 × rupture speed) proposed by Day [1982a], Beroza and Spudich [1988] found the short rise time implied a seismogenic thickness of 1 km, an unreasonably low value. Cormier and Spudich [1984] modeled a wedge-shaped low velocity zone of 1 - 2 km wide in the Calaveras fault, which may have contributed to the short rise time of the 1984 Morgan Hill earthquake. Spudich and Olsen [2001] also pointed out that a 30-100 m wide damage zone is possibly embedded in the 1-2 km-wide low velocity zone in Calaveras.

We further analyze two earthquakes, 1992 Landers and 1999 Hector Mine, for which both LVFZ properties and rise time are well studied. Using techniques based on fault zone guided waves, the Landers LVFZ is 150-250 m wide [Li et al., 1994], while other waveform techniques suggest a 270-360 m wide zone of 35%-60% velocity reduction [Li et al., 2007]. The width of Hector Mine LVFZ inferred from guided wave studies is 75-100 m and the S velocity is reduced by 40%-50% [Li et al., 2002]. Our simulations suggest that narrower LVFZs like Hector Mine should lead to shorter rise time. Ji et al. [2002] compared the average rise time of 1999 Hector Mine to that of 1992 Landers [Wald and Heaton, 1994], and found that they are similar to each other (~3.6 s for Hector Mine and ~4 s for Landers). However, the initiation region of Hector Mine, which is probably well-resolved, shows an average rise time of ~1s, much shorter than that of other regions. Limited by the seismic data and by other mechanisms that possibly contribute to short rise time, e.g. self-healing and bimaterial effect, we cannot conclude that there is a simple correlation between LVFZ properties and rise time. Thus, it is still significant for future study to enrich the database of fault zone properties and rise times, and analyze the relative contributions of other pulse generation mechanisms.

4.4.2 Slip Pulses and Rupture Speed

The shape of a slip pulse is strongly related to the rupture speed. For inplane problems, the rupture speed could either approach the Rayleigh wave speed (subshear) or P wave speeds (supershear). In the presence of an LVFZ we found four rupture speed ranges: LVFZ-Rayleigh, country-Rayleigh,

LVFZ-supershear and country-supershear. Overall, LVFZ-Rayleigh pulses have much shorter rise time and higher maximum slip rate than pulses with higher rupture speed (compare Figure 4.4a to Figure 4.4b). Unlike the usual almost singular shape at the rupture front, the country-Rayleigh pulses for lower velocity reductions (Figures 4.4b and 4.7a) have a much smoother, almost sinusoidal shape. This suggests that the effect of an LVFZ on dynamic ruptures is a possible physical justification for the smooth slip-rate time function assumed in some kinematic earthquake source inversions [Ji et al., 2003]. Country-Rayleigh pulses are dominant in narrow LVFZs (W = 1) with velocity reductions under 30% and for a wide range of initial stresses (Figures 4.6a and 4.6b). Given a shear modulus of 30 GPa and normal stress of 100 MPa, W = 1 corresponds to real LVFZ widths of a few 100 m for critical slip-weakening distances typical of large earthquakes (D_c of a several 10 cm). Hence, our results indicate that LFVZs of mature faults might tend to smooth the slip rate during large earthquakes.

4.4.3 LVFZ Width and Rupture Style

Usually the LVFZ has a width of 100 ~ 400 m, but some faults could accumulate a much thicker damage layer. Savage and Brodsky [2011] summarize fault zone properties from different studies and conclude that the total fault zone thickness is positively related to fault maturity, quantified by the accumulated fault displacement. The Calico fault is an exceptional example, which has a ~1.5 km wide LVFZ. Our results show proportionality between LVFZ width and rise time. The crack-to-pulse transition also occurs later in wider LVFZs (Figures 4.5a and 4.5b). For W = 4 we found a complicated rupture pattern with coexisting cracks and pulses. Assuming scale-dependency of the (apparent) slip-weakening distance D_c , our results suggest that this complexity might be present in large earthquakes (D_c of order 0.5 m) on wide LVFZs like the Calico fault zone, or in smaller events (D_c shorter than 10 cm) on LVFZs of order 100 m wide. For a given LVFZ width our models predict a decreasing degree of rupture complexity as a function of earthquake magnitude. Obviously, in natural faults the effects described here compete with other processes that contribute to rupture complexity.

4.4.4 Ground Motion

LVFZs can trap waves [Li et al., 1994] and amplify ground motions. Spudich and Olsen [2001] found a large 0.6 - 1.0 Hz frequency pulse at a station located 1.2 km away from the Calaveras LVFZ in the records of the 1984 M_w 6.2 Morgan Hill earthquake (source on the Calaveras fault) but not in the records of the 1989 M_w 6.9 Loma Prieta earthquake (source outside the Calaveras fault). They concluded that the large pulse is likely due to the amplification effect of the LVFZ.

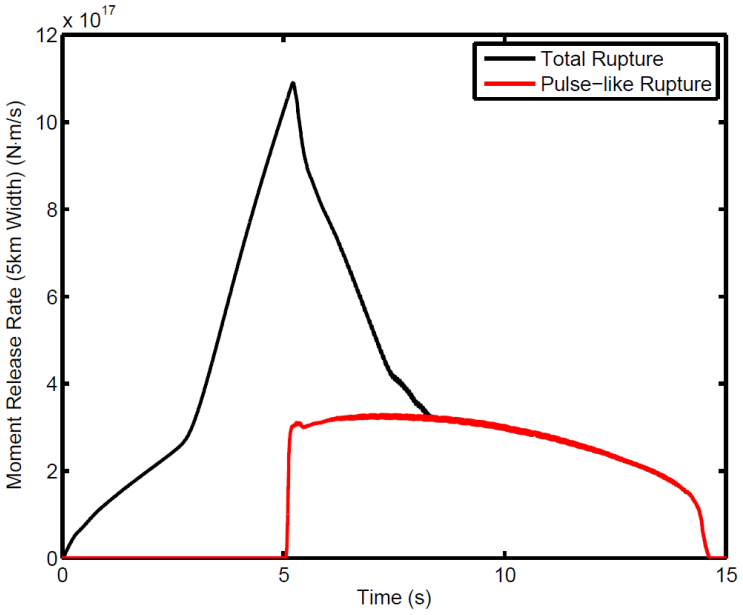

Figure 4.10: Moment release rate as a function of time for a 25 km long rupture inside a 600 m wide LVFZ with velocity reduction of 40%. The red curve is the contribution from the pulse.

We examine here some effects of the LVFZ on dynamic rupture that might have observable implications on ground motions. We consider a rupture that runs for a distance of 25 km until stopped by a high strength barrier. The density, S and P wave velocity are 2670 kg m^{-3}, 3464 m s^{-1} and 6000 m s^{-1} respectively. We assume a 600 m wide LVFZ with velocity reduction of 40%. The normal stress is 100 MPa and the initial shear stress is 25 MPa. The rupture undergoes a crack-to-pulse transition at a distance of about 6 km and then propagates as a pure pulse. Assuming a 5-km-wide seismogenic zone, we calculate the moment release rate generated by the whole rupture and by the contribution of the pulse (Figure 4.10). The crack-to-pulse transition generates a strong high-frequency phase. The pulse-like rupture exhibits a flattened distribution of moment release rate. Its

contribution to the seismic moment is comparable to that of the initial crack. In some of our simulations a crack triggers multiple pulses at regular intervals (Figure 4.11a). Each of these pulse onsets radiates a strong high-frequency phase (Figure 4.11b). Their regular sequence could contribute characteristic frequencies to the earthquake spectrum, although in less idealized situations this regularity might be broken by other complexities. Simulations by Harris and Day (1997, Figure 7) and Ben-Zion and Huang (2002, Figure 12) showed that multiple reflected waves in the LVFZ can generate oscillations of slip rate behind the rupture front. Ben-Zion and Huang (2002, Appendix A) also discussed the effect of a single reflection on the rupture front. Our results reveal an effect of multiple reflections on the rupture front, which has a stronger signature on ground motions than the slip rate oscillations found by Ben-Zion and Huang [2002] and Harris and Day [1997]. Overall, our results show that the effect of LVFZ on dynamic rupture has a significant impact on the radiated wavefield.

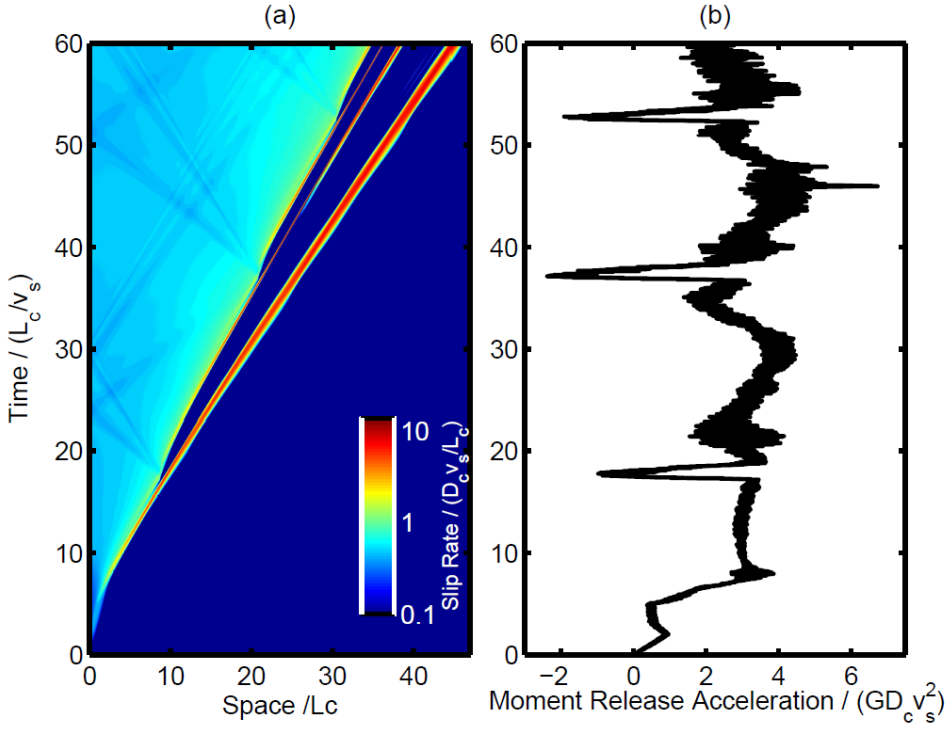

Figure 4.11: (a) Spatio-temporal distribution of slip rate and (b) moment release acceleration as a function of time for S ratio of 1 and LVFZ of width 1 with velocity reduction of 20%.

4.5 Conclusions

The earthquake source has a number of complexities, among which the existence of an LVFZ plays a significant role. It introduces multiple wave reflections that induce stress perturbations on the fault plane. We presented here dynamic rupture simulations on faults that bisect LVFZs of different velocity reductions and widths. We found that the LVFZ reflected waves can unload the fault and induce pulse-like rupture (short rise time). The mechanism is most efficient when the time scale for frictional healing is sufficiently short. Our results show how the pulse shape, rise time, rupture speed and complexity of the rupture process depend on the LVFZ properties. Pure pulse-like rupture is favored by high velocity reduction and narrow width of the LVFZ. The rise time of slip pulses is proportional to the wave travel time across the LVFZ. The effect of the LVFZ can accelerate the transition to supershear rupture speed. Ruptures combining pulses and cracks are typical of LVFZs with lower velocity reduction. These effects of the LVFZ on dynamic rupture have characteristic signatures on the radiated wavefield, contributing especially to high-frequency ground motions. Given the natural existence of LVFZ and the generality of the pulse generation mechanism presented here, it seems unlikely for earthquakes to propagate as pure cracks. However, a mixed crack-pulse rupture might not be distinguishable from a pure crack rupture at the low resolution of current seismological source observations.

C h a p t e r 5

EARTHQUAKE RUPTURES MODULATED BY WAVES IN DAMAGED FAULT ZONES

Huang, Y., J.-P. Ampuero and D. V. Helmberger (2014), Earthquake ruptures modulated by waves in damaged fault zones. Journal of Geophysical Research, doi: 10.1002/2013JB010724.

Supplementary materials are included in Appendix C.

Faults are usually surrounded by damaged rocks, which have lower elastic moduli and seismic wave velocities than their host rocks. Such damaged fault zones are usually several hundred meters wide and develop a complex yet interesting wave field when earthquakes happen inside them. If the interface between the fault zone and host rock is sharp enough, waves are reflected and head waves are generated. Each wave can cause either increase or drop of fault stress, depending on its polarity. These waves can interact with earthquake ruptures and modulate rupture properties, such as rupture speed, slip rate and rise time. We find through 2D dynamic rupture simulations that: (1) Reflected waves can induce multiple slip pulses. Fault zone properties have a stronger control on their dominant rise time than frictional properties. (2) Head waves can cause oscillations of rupture speed and, in a certain range of fault-zone widths, a permanent transition to supershear rupture with speeds that are unstable in homogeneous media. (3) Large attenuation smears the slip rate function and delays the initial acceleration of rupture speed, but does not affect significantly the rise time or the period of rupture speed oscillations. (4) Fault zones cause a rotation of the background stress field and can induce plastic deformations on both sides of the fault. The plastic deformations are accumulated both inside and outside the fault zone, which indicates a correlation between fault zone development and repeating ruptures. Spatially periodic patterns of plastic deformations are formed due to oscillating rupture speed, which may leave a permanent signature in the geological record. Our results indicate that damaged fault zones with sharp boundaries promote multiple slip pulses, short rise times and supershear ruptures.

5.1 Introduction

The kinematics of earthquake ruptures can be represented by three key parameters: slip rate, rise time (the duration of slip at a given point) and rupture speed. Seismic observations suggest that these parameters are highly variable. Rise time can either be comparable to the overall duration of the event as suggested by the crack model [Madariaga, 1976], or much shorter than the overall duration, which leads to the so-called slip pulse model [Heaton, 1990]. Several mechanisms have been proposed to explain the generation of slip pulses, including self-healing due to velocity-dependent friction [Perrin et al., 1995; Beeler and Tullis, 1996] and healing fronts induced by stress heterogeneities [Day, 1982; Beroza and Mikumo, 1996]. Ruptures can also become supershear, i.e. reach a speed faster than the shear wave speed, as observed in the 1979 Imperial Valley earthquake [Archuleta, 1984; Spudich and Cranswick, 1984], the 1999 Izmit earthquake [Bouchon et al., 2001, 2002], the 2001 Kunlunshan earthquake [Bouchon and Vallee, 2003; Walker and Shearer, 2009] and the 2002 Denali earthquake [Dunham and Archuleta, 2004; Ellsworth et al., 2004; Walker and Shearer, 2009]. Theoretical and laboratory models of supershear ruptures require the shear stress on the fault to be close enough to the static frictional strength, relative to the stress drop [Andrews, 1976; Xia et al., 2004; Dunham, 2007].

Table 5.1 Summary of material properties of main fault zones (the same as Table 1.1)

Fault Zones	Width (m)	Velocity Reduction (%)	Q_s	References
San Andreas	~ 150	30-40	10-40	[Lewis and Ben-Zion, 2010]
	~ 200			[Li et al., 2006]
San Jacinto	125-180	35-45	20-40	[Lewis et al., 2005]
	150-200	25-60		[Yang and Zhu, 2010]
Landers	270-360	35-60		[Li et al., 2007]
	150-200	30-40	20-30	[Peng et al., 2003]
Hector Mine	75-100	40-50	10-60	[Li et al., 2002]
Calico	~ 1500	40-50		[Cochran et al., 2009]
	~ 1300	40-50		[Yang et al., 2011]
Nojima	100-220			[Mizuno et al., 2008]
Anatolian	~ 100	50	10-15	[Ben-Zion et al., 2003]

Current models of slip-pulses and supershear ruptures have been developed under the simplifying assumption of a uniform elastic medium or a bimaterial interface. However, faults are often surrounded by damaged fault zones [Chester and Logan, 1986; Sibson, 1986; Scholz, 1987;

Chester and Chester, 1998; Ben-Zion and Sammis, 2003; Savage and Brodsky, 2011; Rowe et al., 2013] caused by either aseismic deformation [Cowie and Scholz, 1992; Chester and Chester, 2000; Childs et al., 2009; Faulkner et al., 2011] or by coseismic processes [Rice et al., 2005; Ben-Zion and Ampuero, 2009; Sagy and Korngreen, 2012; Xu et al., 2012; Rempe et al., 2013; Johri et al., 2014]. A typical manifestation of damage is a reduced seismic wave velocity (Table 5.1). Due to the significant velocity reductions inside fault zones, these structures can trap seismic waves that can continuously perturb stresses on the fault during earthquakes. Previous numerical modeling of dynamic ruptures inside fault zones, assuming ideal elastic media, indicates that these low-velocity structures can cause the generation of slip pulses and accelerate the transition to supershear rupture [Harris and Day, 1997; Huang and Ampuero, 2011], which otherwise do not exist in a uniform medium given the same initial conditions and friction parameters. These results suggest that in the regions where damaged fault zones are observed (Table 5.1), earthquake ruptures can have complexities such as short rise time and supershear rupture speed due to the influence of fault zones.

Previous findings also pose several new questions: Which waves cause the generation of slip pulses and the rapid transition to supershear rupture? Can these waves exist in fault zones despite large attenuation and off-fault plasticity? What are the differences between slip pulses and supershear ruptures induced by fault zone waves and those generated by other mechanisms? In this paper, we aim to answer these questions through dynamic rupture modeling. We focus on fault zones bounded by sharp material interfaces, as an end member class of fault zone structures in which the phenomena described are exacerbated. We describe our model assumptions and methods in Section 5-2. In Section 5-3, based on dynamic rupture simulations on faults in a homogeneous medium and in fault zones, we show how the velocity reduction and width of elastic fault zones affect the slip rate, rise time and rupture speed. In Section 5-4, by comparing the results of dynamic rupture simulations with the stress wave field induced by a point source, we identify the waves that cause variations of rise time and rupture speed in fault zones. The effects of inelasticity within the fault zone are examined in Section 5-5. Implications for earthquake ruptures in natural fault zones are discussed in Section 5-6.

5.2 Model Description

We consider a 2D inplane rupture on a planar fault that bisects a fault zone (Figure 5.1). The fault zone is embedded in an infinite medium composed of a host rock. We define the width of the fault zone as W^{FZ} and the relative velocity reduction as $\Delta v = 1 - v^{FZ}/v^{host}$ (%), where v^{FZ} and v^{host} are wave speeds inside the fault zone and host rock, respectively. Subscripts 'p' and 's' denote P and S waves. For example, v_s^{host} denotes the S wave speed in the host rock. We assume that Δv is the same for P and S waves unless otherwise specified.

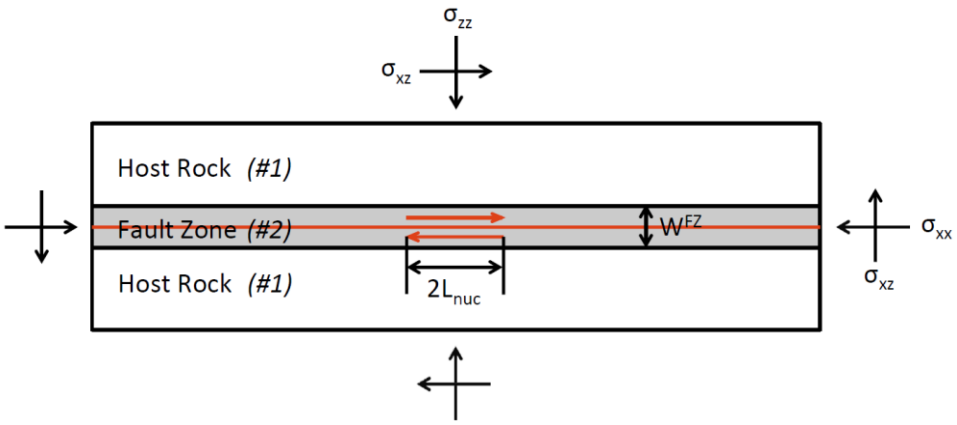

Figure 5.1: Model setup of the 2D inplane rupture on a fault that bisects a fault zone embedded in a host rock. The host rock and fault zone are composed of material #1 and #2, respectively. The rupture is nucleated by an overstressed patch in the middle, which has a width 2 L_{nuc}.

We adopt a strongly velocity-weakening friction law, which reproduces the dramatic weakening of friction at seismic slip rates (> 0.1 m/s) observed in high-speed rock experiments [Reches and Lockner, 2010; Goldsby and Tullis, 2011]. The friction law agrees with laboratory data in that the steady-state friction drop is proportional to $1/v$ when the slip rate, v, is larger than a critical velocity scale v_c. This feature is also predicted by theoretical models of weakening by flash heating [Rice, 2006; Beeler et al., 2008]. The sliding friction μ_f and the evolution of a state variable θ are controlled by the static friction coefficient μ_s, the critical slip distance D_c, the characteristic velocity scale v_c and the two positive coefficients α and β [Ampuero and Ben-Zion, 2008; Gabriel et al., 2012]:

$$\mu_f = \mu_s + \alpha \frac{v}{v+v_c} - \beta \frac{\theta}{\theta+D_c} \tag{5.1}$$

$$\frac{d\theta}{dt} = v - \frac{v_c \theta}{D_c} \tag{5.2}$$

The value of v_c is in the range of 0.05 to 2 m/s based on theoretical models [Beeler et al., 2008], while Goldsby and Tullis [2011] suggest a value of ~ 0.1 m/s from laboratory experiments. The dynamic friction coefficient μ_d is defined as the steady-state sliding friction at infinitely high slip velocity: $\mu_d = \mu_s + \alpha - \beta$. The state evolution equation (5.2) encapsulates two physical ingredients: slip-weakening and time-dependent healing. The state variable relaxes exponentially towards its steady-state value, $\theta = vD_c/v_c$, over a characteristic time scale D_c/v_c. In the limit of fast sliding well above steady state $v \gg \theta v_c/D_c$, the state is proportional to slip and the evolution effect of the friction law (the last term in Equation 5.1) yields slip-weakening with characteristic slip scale D_c. At very low sliding speed well below steady state $v \ll \theta v_c/D_c$, and the friction evolution is dominated by exponential time-dependent healing.

Due to the symmetry of the problems considered here, the normal stress σ_0 remains constant. We assume a spatially uniform normal stress. We artificially start ruptures by setting an over-stressed nucleation patch of width 2 L_{nuc} around the hypocenter. Inside the nucleation patch, the initial shear stress τ_0 is slightly above the static strength $\tau_y = \sigma_0 \mu_s$. Outside the nucleation patch, τ_0 is chosen to be uniform and small enough to ensure subshear rupture in a homogeneous medium, but large enough to nucleate rupture successfully by using a nucleation patch of reasonable size. Specifically, we set the nominal relative strength parameter [Das and Aki, 1977a] as S = $(\tau_y - \tau_0)/(\tau_0 - \tau_d)$ = 1.7, where $\tau_d = \sigma_0 \mu_d$ is the steady-state dynamic strength at very high slip rate. We will discuss the influence of different τ_0 in Section 5.6. Given a certain v_c, a transition from dying ruptures to sustained ruptures occurs as L_{nuc} is increased in a homogeneous medium [Ampuero and Ben-Zion, 2008]. In our simulations we set the value of L_{nuc} large enough to get sustained ruptures for the range of v_c we considered.

We solve the problem of dynamic rupture in fault zones numerically with a 2D spectral element method (SEM2DPACK, http://www.sourceforge.net/projects/sem2d/). The numerical method is described (in 3D) by Kaneko et al. [2008] and has been applied in previous work [e.g., Madariaga et al., 2006; Kaneko et al., 2011; Huang and Ampuero, 2011; Gabriel et al., 2012, 2013; Xu et al., 2012]. The element size is set small enough to ensure well-resolved results based on a priori criteria described by Ampuero and Ben-Zion [2008] and on a posteriori verification that the

process zone is resolved by more than five grid nodes. Numerical convergence as a function of element size is demonstrated in Appendix C.

5.3 Ruptures in Elastic Fault Zones

5.3.1 Dimensionless Quantities and Reference Simulation in Homogeneous Media

Table 5.2 Dimensionless model parameters

Parameter	Description	Value
$\boldsymbol{\rho}$	Density	1
$\boldsymbol{v_p^{host}}$	P wave speed in the host rock	1.732
$\boldsymbol{v_s^{host}}$	S wave speed in the host rock	1
$\boldsymbol{\sigma_0}$	Normal stress	2
$\boldsymbol{\tau_0}$	Initial shear stress	0.57
$\boldsymbol{\mu_s}$	Static friction coefficient	0.6
$\boldsymbol{D_c}$	Critical slip distance	1
$\boldsymbol{v_c}$	Characteristic velocity scale	0.04/0.1
$\boldsymbol{\alpha}$	Direct effect coefficient	0.005
$\boldsymbol{\beta}$	Evolution effect coefficient	0.505

We show the results of dynamic rupture models in elastic media in this section. We first illustrate, for reference, the behavior of ruptures in the absence of fault zones. We then show the changes of rupture behavior induced by fault zones with different widths and velocity reductions. To preserve the generality of the problem, we use dimensionless quantities for space x, time t, slip D, slip velocity D' and stress τ throughout Section 5.3:

$$\tilde{x} = x/L_c \tag{5.3}$$

$$\tilde{t} = tv_s^{host}/L_c \tag{5.4}$$

$$\widetilde{D} = D/D_c \tag{5.5}$$

$$\widetilde{D'} = D'/v_{dyn} \tag{5.6}$$

$$\tilde{\tau} = \tau/\Delta\tau_s \tag{5.7}$$

Given shear modulus G^{host}, we define the following parameters:

$$L_c = G^{host} D_c / \Delta\tau_s \tag{5.8}$$

$$v_{dyn} = v_s^{host} D_c / L_c \tag{5.9}$$

$$\Delta\tau_s = (\mu_s - \mu_d)\sigma_0 = \tau_y - \tau_d \tag{5.10}$$

Our results can be applied to a variety of initial conditions by converting these dimensionless quantities. For example, when $G^{host} = 30\,GPa$ and $\Delta\tau_s = 30\,MPa$, we find $L_c = 100\,m$ for $D_c = 0.1\,m$ and $L_c = 1\,km$ for $D_c = 1\,m$. The values of dimensionless parameters are summarized in Table 5.2. Among them, α needs to be a small but positive number to avoid ill-posedness, while β is given by the equation $\mu_d = \mu_s + \alpha - \beta$.

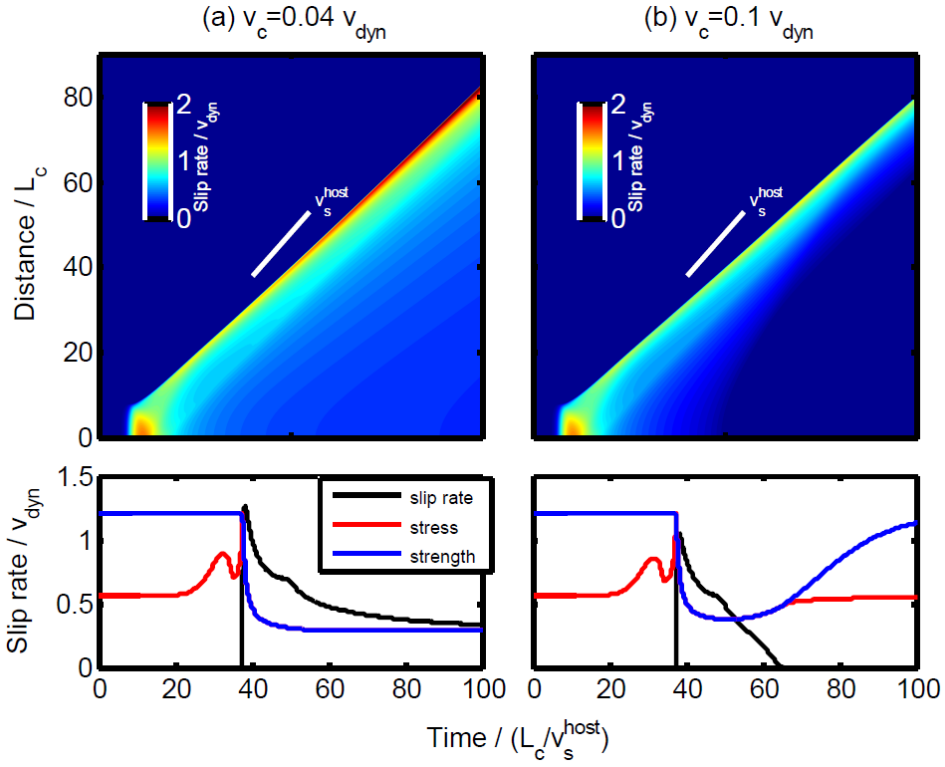

Figure 5.2: Spatiotemporal view of slip rate (top) and slip rate, stress and frictional strength at a distance of 30 L_c from the hypocenter (bottom) for ruptures in a homogeneous medium with two different values of the characteristic velocity of frictional weakening, v_c. The white solid lines in the top figures denote v_s^{host}. Rupture speed v_r^{host} is about 0.8 v_s^{host}.

In a homogeneous medium, rupture behavior is controlled by friction parameters and initial stresses on the fault. Notably, increasing the critical velocity scale v_c induces a transition from crack-like rupture to pulse-like rupture (Figure 5.2). At a certain value of v_c (which depends on the initial stress) the rise time becomes shorter than the total rupture time, and then decreases with increasing v_c [Ampuero and Ben-Zion, 2008]. The characteristic time scale D_c/v_c in the strong-velocity weakening friction law (Equation 5.2) controls the time scale for frictional strength to increase, and hence the emergence of healing fronts and the crack-to-pulse transition. For small values of v_c (Figure 5.2a), the friction law functions more like slip weakening [Shaw and Rice, 2000; Ampuero and Ben-Zion, 2008], and the rupture propagates as a crack. A large v_c (Figure 5.2b) favors pulse-like ruptures and shorter rise time.

5.3.2 Multiple Pulses and Rise Times

In the presence of fault zones, a second characteristic time scale, W^{FZ}/v^{FZ}, is provided by the waves reflected at the interfaces bounding the fault zone. Waves with pre-critical incidence angles continuously leak energy out of the fault zone, while waves with post-critical incidence angles are trapped inside due to total reflections. Constructively interfering trapped waves can modulate stresses on the fault and strongly affect ruptures, especially if they reach the rupture front. We refer to all these waves inside fault zones as *fault-zone waves*. These waves will be described in detail in Section 5.4. In summary, ruptures in fault zones with strongly velocity-weakening friction are controlled by two characteristic time scales: the time scale of wave propagation W^{FZ}/v^{FZ} and the time scale of frictional healing D_c/v_c.

Next we will show results of dynamic rupture simulations under fixed friction parameters ($D_c = 1$ and $v_c = 0.1\ v_{dyn}$, as in the homogeneous example shown in Figure 5.2b) but varying the time scale of wave propagation.

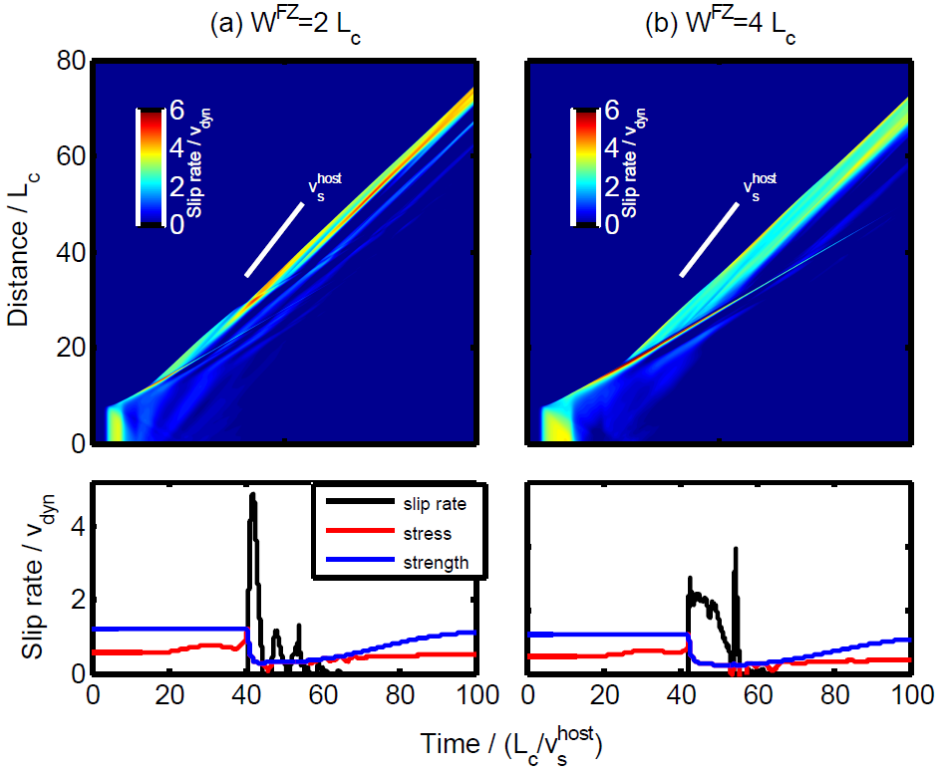

Figure 5.3: Spatiotemporal view of slip rate (top) and slip rate, stress and frictional strength at a distance of 30 L_c (bottom) of ruptures in fault zones of 50% velocity reduction with two different fault-zone widths ($v_c = 0.1\ v_{dyn}$). The white solid lines in the top figures denote v_s^{host}.

We have shown before that fault zones can induce slip pulses and control their rise time [Huang and Ampuero, 2011]. The same effects of fault zones appear in our current study, but our new simulations allow for a deeper insight into the rich range of phenomena and their underlying mechanisms. We first consider ruptures in fault zones of 50% velocity reduction (Δv =50%) for W^{FZ}/L_c= 2 and 4. When W^{FZ}=2 L_c, we find slip rate is highly oscillatory compared to ruptures in a homogeneous medium, leading to multiple short pulses (Figure 5.3a). Depending on their polarity, fault-zone reflected waves induce fault stress perturbation that may be favorable or unfavorable for slip. Slip stops upon the arrival of each fault zone reflected wave that carries an unfavorable stress perturbation, and may resume multiple times when each reflected wave with favorable stress arrives. The rise time of the first pulse is near 5.5 L_c/v_s on average, almost one fourth of that in a homogeneous medium (Figure 5.2b). When W^{FZ}=4 L_c, the rupture evolves into a large pulse with sharp healing front, followed by shorter pulses (Figure 5.3b). The rise time of the first large pulse is about 11 L_c/v_s on average, still shorter than in a homogeneous medium but

twice as long as in the case of W^{FZ}=2 L_c. As we will show later in Section 5.4, the rise time of the first pulse is controlled by reflected waves in fault zones and thus proportional to W^{FZ}. Peak slip rate is larger than that in the homogeneous case by more than a factor of two. Note that in both cases the total rise time, defined as the time between the onset of the first pulse and the end of the last pulse, is still determined by self-healing caused by strongly velocity-weakening friction. Since it is hard to accurately measure the total rise time from observations, for practical purpose we only consider the rise time of the first pulse, which accomplishes more than 80% of the final slip in both cases after ruptures reach steady state. The above examples show that both rise time and slip rate of the first pulse are controlled by the structural and material properties of the fault zone, rather than by the friction parameters.

5.3.3 Oscillatory Rupture Speeds and Enhanced Supershear Transition

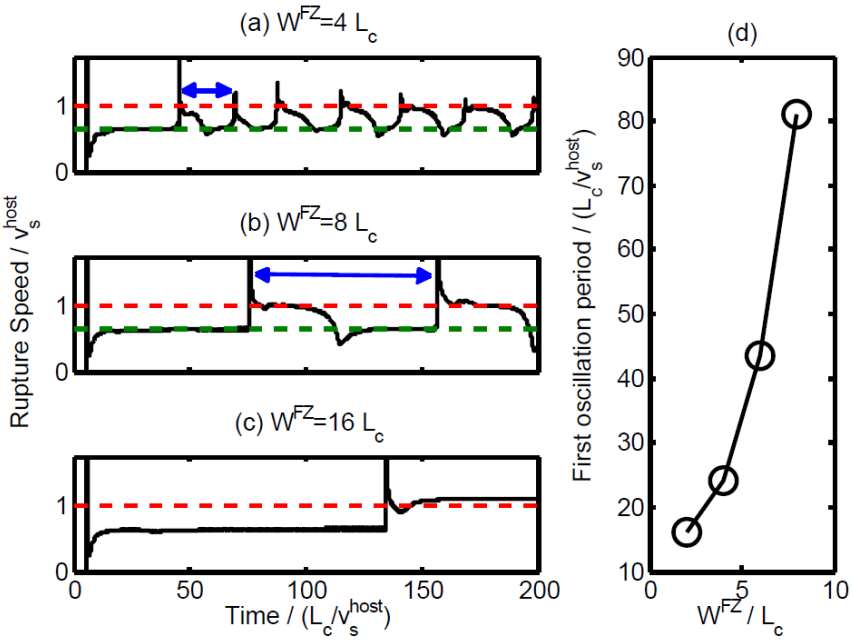

Figure 5.4: (a)-(c): Rupture speed as a function of time in fault zones of 30% velocity reduction with three different fault-zone widths. We calculate rupture speeds based on the position and timing of the tail of the process zone (defined as the location where slip equals D_c) to avoid ad hoc smoothing. Rupture front in a fault zone of 30% velocity reduction with a fault-zone width of 4 L_c is shown in Figures 10 and 11. Red dashed lines denote v_s^{host} and green dashed lines denote Rayleigh wave speed of the fault zone. Blue arrows mark the first rupture speed oscillation period. (d) Period of the first rupture speed oscillation in fault zones of 30% velocity reductions as a function of fault-zone width.

In a homogeneous medium, rupture approaches a speed $v_r^{host} \approx 0.8\, v_s^{host}$ quickly after the nucleation (Figure 5.2). The value of v_r^{host} depends primarily on the state of stresses (the S ratio) as discussed by Gabriel et al., [2012]. In the fault zones with Δv=50%, rupture speed approaches v_r^{host} for both values of W^{FZ} (Figure 5.3), but if Δv =30% rupture speed oscillates strongly instead (Figure 5.4). Rupture speed is calculated based on the position and timing of the tail of the process zone (defined as the location where slip equals D_c) to achieve stable estimates without ad hoc smoothing. The oscillations of rupture speed become more pronounced as W^{FZ} increases (compare the differences between maximum and minimum rupture speeds in Figures 5.4a and 5.4b). When W^{FZ}=4 L_c and 8 L_c, rupture speed oscillates between a minimum value slower than the Rayleigh wave speed of the fault zone material and a maximum value faster than v_s^{host}. Because of accelerations and decelerations of the rupture front, the rise time of the first pulse also oscillates, but the average rise time is still short compared to the total rupture time. The period of the first rupture speed oscillation (denoted by blue arrows in Figures 5.4a and 5.4b) increases as a function of fault-zone width W^{FZ}, and apparently diverges at a finite value $W^{FZ}/\, L_c \approx 10$ (Figure 5.4d).

For the case with W^{FZ}=16 L_c (Figure 5.4c), the rupture jumps to a speed faster than v_s^{host} and then remains at a speed near v_p^{FZ}. Note that the rupture is supershear relative to both the host rock and fault zone. This supershear rupture speed persists for a much longer time than that shown in Figure 5.4c. The disappearance of rupture oscillations at large fault-zone widths (Figure 5.4d) also indicates that the supershear transition is permanent. Given the assumed initial stresses, supershear ruptures do not exist in a homogeneous medium with the material properties of the host rock [Gabriel et al, 2012], as illustrated by our reference simulation (Figure 5.2). Fault-zone waves hence promote supershear ruptures, as first noted by Huang and Ampuero [2011]. For the limit case when W^{FZ} increases to infinity, the problem converges to another homogeneous case with the elastic properties of the fault zone material, and hence rupture speed approaches the Rayleigh wave speed of the fault zone and does not undergo oscillations anymore. Thus, there is an intermediate range of fault zone widths that promote supershear rupture. The disappearance of supershear ruptures as W^{FZ} increases beyond a certain level is related to the decay of the amplitude of fault-zone waves with propagation distance due to geometric spreading (Section 5.4). Moreover, we find that the supershear transition in fault zones operates through the same daughter crack mechanism as in homogeneous media [Andrews, 1976; Dunham, 2007]. Figures

5.5a and 5.5b show the slip rate, fault stress and fault strength before and after the supershear transition in the case of W^{FZ}=16 L_c. A wave-mediated shear stress peak travels ahead of the initial rupture front. When it overcomes the fault strength, a daughter crack nucleates and eventually propagates spontaneously at a supershear speed close to v_p^{FZ} (Figure 5.5b).

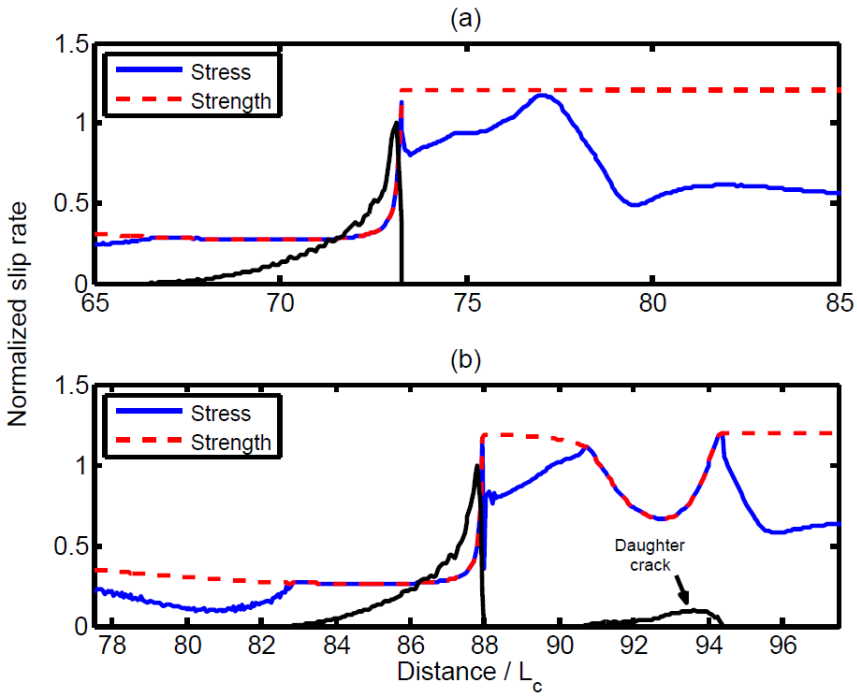

Figure 5.5: Slip rate, stress and frictional strength (a) before and (b) after the supershear transition for ruptures in fault zones of 30% velocity reduction with a fault-zone width of 16 L_c. Slip rate is normalized by the local peak slip rate.

5.3.4 Dependence of Rupture Speed, Rise Time and Rupture Complexity on Velocity Contrast

As shown above, the amount of velocity reduction within the fault zone influences the fundamental properties of earthquake ruptures, e.g., it controls whether a rupture behaves as a steady-state pulse or has oscillating rupture speed. To illustrate the fundamental differences between ruptures in fault zones and in homogeneous media, we summarize in Figure 5.6 the dependence of rupture speed and rise time on velocity reduction Δv when W^{FZ}= 4 L_c. We consider rupture speed and rise time beyond a distance of 5 L_{nuc} from the hypocenter, well beyond transients related to the artificial nucleation procedure. We consider the rise time of the

first pulse, which accomplishes more than 80% of the final slip after the initial oscillation of rupture speed or the transition to steady-state rupture.

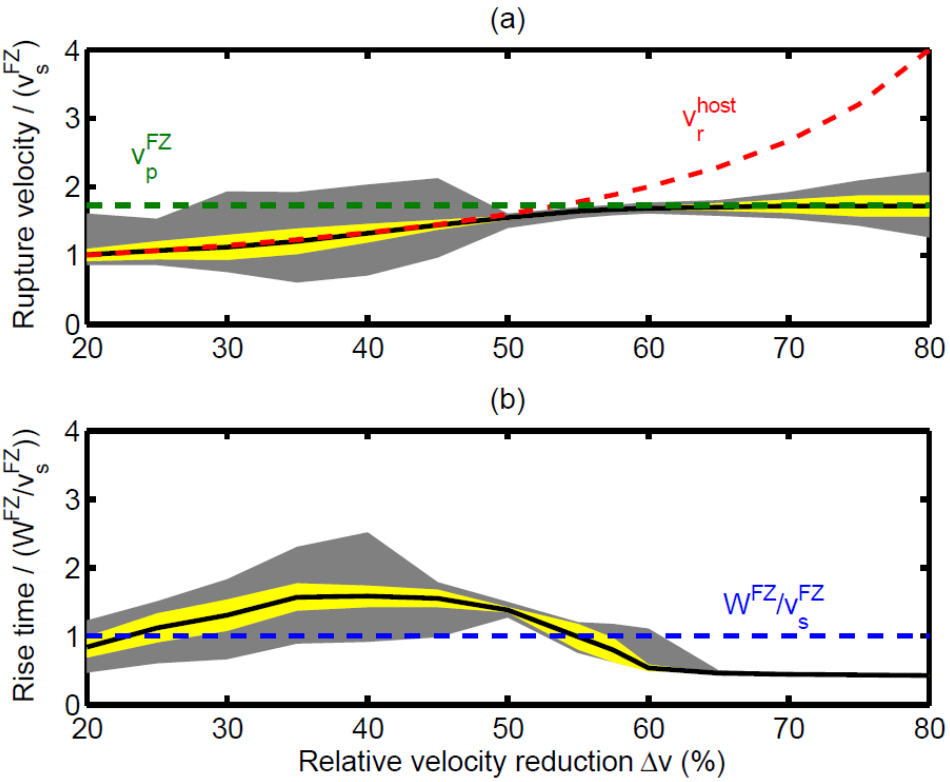

Figure 5.6: The total range (gray region), median (black solid line) and median absolute deviation (yellow region) of (a) rupture speed and (b) rise time in fault zones of different velocity contrasts when the fault-zone width is 4 L_c. Green dotted line denotes P wave speed in the fault zone v_p^{FZ} and red dotted line denotes rupture speed in a homogeneous medium v_r^{host}, as shown in the reference simulation (Figure 5.2). Rupture speed is normalized by the S wave speed in the fault zone v_s^{FZ}, and rise time is normalized by the travel time of fault-normal reflected S waves W^{FZ}/v_s^{FZ} (blue dotted line).

We identify two distinct rupture behaviors. When Δv =20%-40%, rupture speed and rise time are highly oscillatory throughout the whole rupture process (Figure 5.6). When Δv =60%-80%, rupture evolves to a steady state with rupture speed approaching v_p^{FZ} and rise time equal to about a half of W^{FZ}/v_s^{FZ} (Figures 5.6 and 5.7c). In the intermediate range, Δv =40%-60%, ruptures are complicated yet interesting. For Δv between 40% and 50%, ruptures display a transition from pronounced periodic oscillations to damped oscillations (Figure 5.7a), which occurs earlier at larger Δv. When Δv =50%-60%, rupture speed becomes steady very soon after rupture initiation

but rise time does not. Instead it drops (by less than a half) at a finite propagation distance (Figure 5.7b), which is shorter at larger Δv.

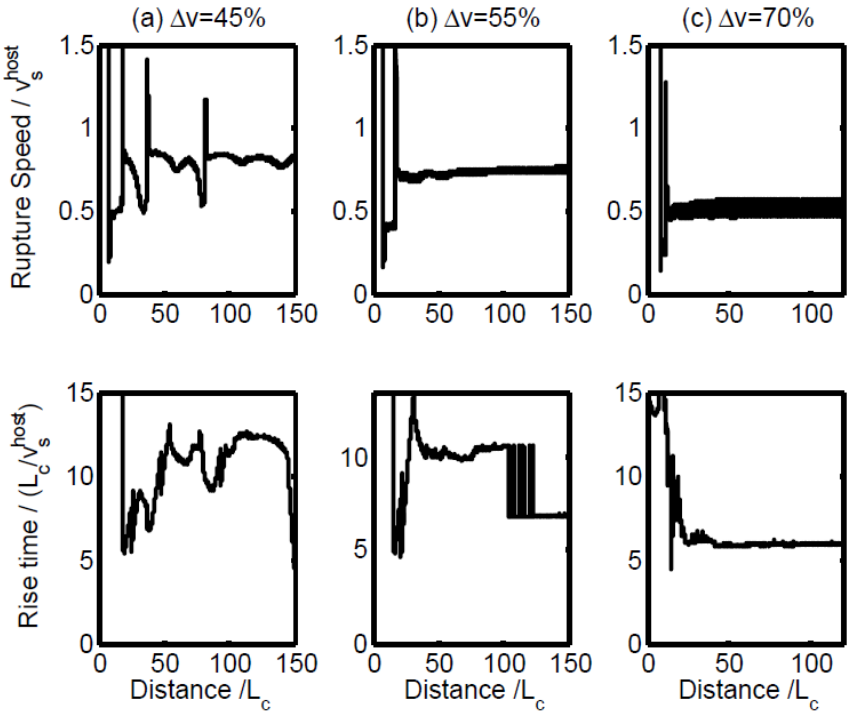

Figure 5.7: Rupture speed (top) and rise time (bottom) in fault zones of (a) 45%, (b) 55% and (c) 70% velocity reductions with a fault-zone width of 4 L_c.

Because the maximum rupture speed appears to reach ~2.1 v_s^{FZ} (or ~1.2 v_s^{host}), it is tempting to say that ruptures can accelerate to a speed faster than v_s^{host} during the oscillations (Figure 5.4a and 5.4b). However, some of these supershear episodes may be too short-lived to be seismologically observable. Moreover, the estimates of rupture speed and rise time in dynamic rupture simulations are somewhat dependent on the measurement method and the degree of smoothing. Given that rupture speed and rise time vary during rupture propagation, we assess the overall rupture behavior by reporting their median and median absolute deviation in each simulation (black solid lines and yellow regions in Figures 5.6a and 5.6b). We find that, when W^{FZ}= 4 L_c, ruptures are overall subshear with respect to the host rock, despite the oscillations of rupture speed: the median rupture speed stays at either v_p^{FZ} or v_r^{host}, whichever is lower (Figure 5.6a).

Because $v_r^{host} \approx 0.8 v_s^{host}$ in our reference model, the median rupture speed is expected to stay at v_r^{host} when $\Delta v < (1 - v_r^{host}/v_p^{host}) = 53.8\%$ and to approach v_p^{FZ} when $\Delta v > 53.8\%$. We can generalize this argument for different states of stress and friction parameters as long as v_r^{host} is known. For example, if the conditions are such that a rupture in a homogeneous medium propagates at the Rayleigh wave speed of the host rock ($\sim 0.92 v_s^{host}$), the rupture speed in a fault zone is controlled by v_p^{FZ} if $\Delta v > (1 - 0.92 v_s^{host}/v_p^{host}) = 46.9\%$. Rupture speed transition occurs at a higher Δv if the rupture in a homogeneous medium is slower. Given the most common range of Δv in natural fault zones (~30-50%), rupture is more likely to be controlled by v_r^{host} under subshear conditions.

5.4 Fault-Zone Waves and Their Influence on Rise Time and Rupture Speed

Our previous results indicate that fault-zone waves are the key to understanding the influence of fault zones on earthquake ruptures. To analyze the wave field developed inside fault zones, we impose a kinematic "point" source and record the resulting perturbations of shear stress on the fault. The point source is approximated by a Gaussian slip-rate function. The time duration of the slip-rate function is chosen to be short enough to resolve characteristic phases of fault-zone waves. The source amplitude is also spatially distributed as a Gaussian function with a width much smaller than the fault length yet large enough to ensure numerical resolution. For convenience of defining waves, we denote the material of the host rock as #1 and that of the fault zone as #2 (Figure 5.1). Thus, reflected waves that only involve S waves in the fault zone are referred to as S_2S_2, and S head waves that propagate at v_s^{host} along the boundary of the fault zone are referred to as $S_2S_1S_2$.

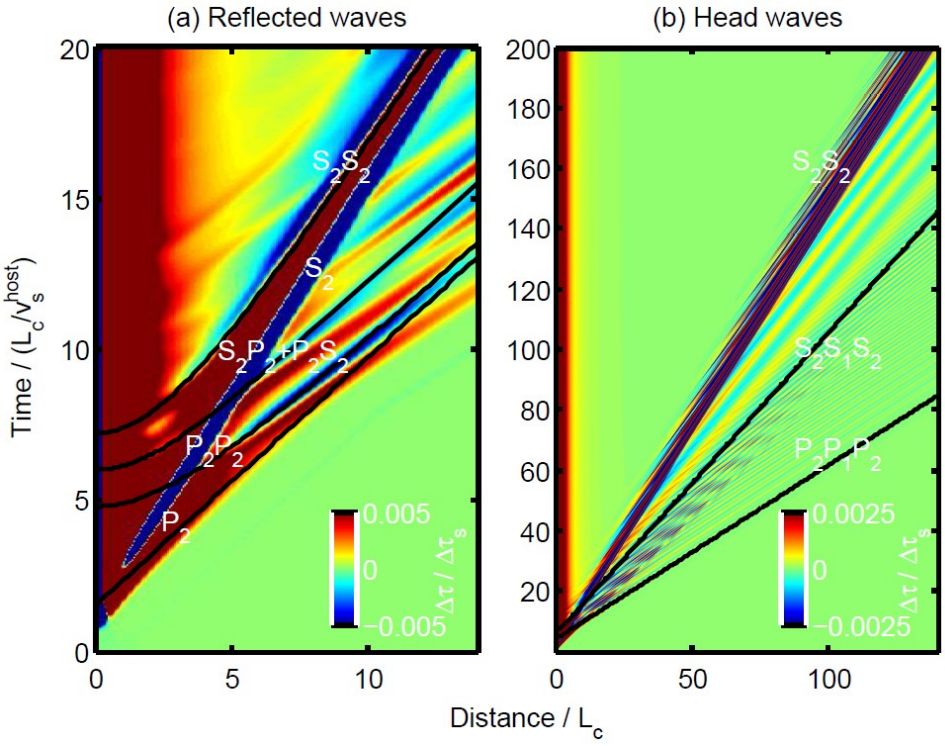

Figure 5.8: Spatiotemporal distribution of shear stress transient on the fault induced by a prescribed localized slip source at the hypocenter in a fault zone of 30% velocity reduction with a fault-zone width of 4 L_c. Different phases of (a) reflected waves and (b) head waves are indicated.

We identify different phases of reflected waves at early times (Figure 5.8a). The direct P_2 wave is followed by P_2P_2 reflected waves, and then S_2P_2 and P_2S_2 reflected waves. Their speeds all approach v_p^{FZ} far from the source. The direct S_2 wave, which induces larger amplitude of stress perturbation than the P phases, is followed by S_2S_2 reflected waves. Beyond the distance at which reflected waves reach critical angles, head waves are generated and interfere with reflected waves (Figure 5.8b). The interference causes the polarity of head waves to alternate. Generally speaking, S head waves have longer period than P head waves.

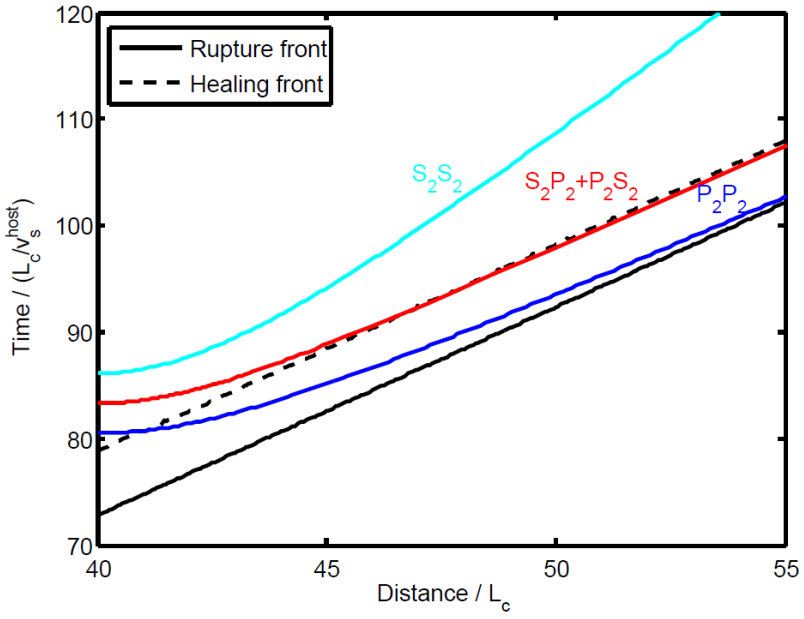

Figure 5.9: Rupture front and healing front of the rupture in a fault zone of 70% velocity reduction with a fault-zone width of 4 L_c. The time difference between rupture front and healing front is the rise time. Travel-time curves of reflected waves are shown in color.

We focus on the steady-state ruptures (Δv =60-80%) in order to understand the role of fault-zone waves in generating slip pulses. As the steady-state ruptures propagate at a speed of v_p^{FZ}, the waves that generate healing of the first pulse should approach the same speed in order to keep the rise time constant. Possible waves are P_2P_2, S_2P_2 and P_2S_2 reflected waves, and $S_2P_2S_2$ head waves. We measure the differences of travel time between the direct P_2 wave and the above waves. We find that only S_2P_2 and P_2S_2 reflected waves lead to a travel-time difference equal to the observed rise time of the first pulse (Figure 5.9). We also confirm that the stress perturbations caused by S_2P_2 and P_2S_2 reflected waves are unfavorable for slip, which is necessary to induce healing (Figure 5.8a). Thus, the S_2P_2 and P_2S_2 reflected waves generate the first pulses and control the rise time of steady-state pulse-like ruptures. Moreover, as S_2P_2 and P_2S_2 reflected waves are nearly critical when their apparent speeds approach v_p^{FZ}, we have $v_p^{FZ} \approx v_s^{FZ}/\sin(\theta)$, where θ is the incidence or reflection angle of S waves. The rise time can be approximated by the travel time difference between the rupture front and reflected wave. For nearly critical S_2P_2 and P_2S_2 reflected waves:

$$\tau_{ris} \approx \left(\frac{W^{FZ}}{2\cos\theta v_s^{FZ}} + \frac{2L - W^{FZ}\tan\theta}{2v_p^{FZ}}\right) - \frac{L}{v_r} \tag{5.11}$$

where L and v_r are rupture length and rupture speed, respectively. Given $v_r = v_p^{FZ}$ and $\sin\theta = \frac{v_s^{FZ}}{v_p^{FZ}}$,

$$\tau_{ris} = \frac{W^{FZ}}{2v_s^{FZ}}\sqrt{1 - \left(\frac{v_s^{FZ}}{v_p^{FZ}}\right)^2} \approx 0.41\frac{W^{FZ}}{v_s^{FZ}} \tag{5.12}$$

This equation is in good agreement with our numerical results, in which the rise time of steady-state ruptures is about a half of W^{FZ}/v_s^{FZ} (Figure 5.6b). Additional insight on dynamic stresses induced by steady pulses may be gained from the analytical work by Weertman [2014].

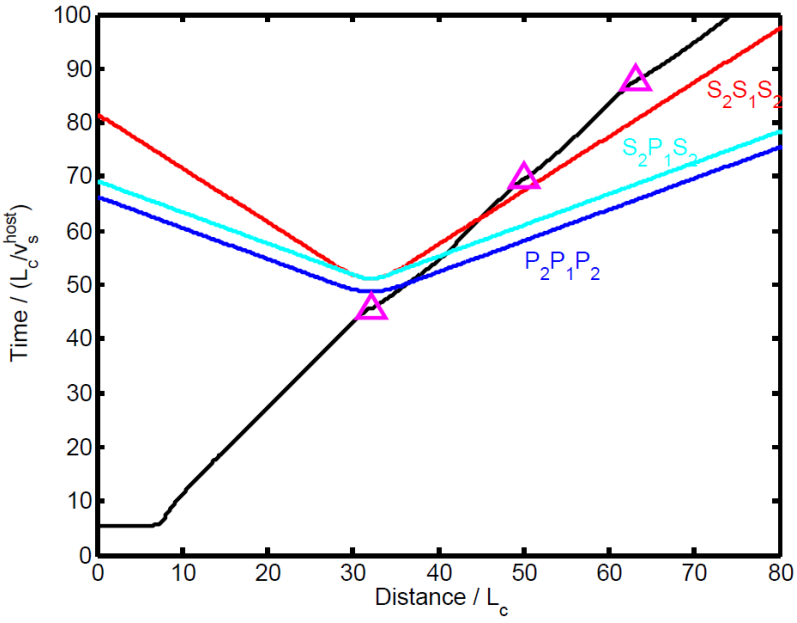

Figure 5.10: Rupture front of the rupture (black solid line) in a fault zone of 30% velocity reduction and fault-zone width of 4 L_c. Magenta triangles denote the rupture acceleration episodes. Travel-time curves of the first arrivals of head waves radiated from the first acceleration episode are shown in color.

Fault-zone waves can also accelerate and decelerate ruptures when Δv =20-40% (Figures 5.4a, 5.4b and 5.6a). We find that oscillations of the rupture front are caused by head waves. Accelerations of rupture front happen when head waves that carry a favorable stress perturbation

arrive, and decelerations occur when head waves with opposite polarity arrive. To understand whether P or S head waves control the period of oscillations, we mark each rupture acceleration episode on a space-time plot of the rupture front (W^{FZ}= 4 L_c, Figures 5.10 and 5.11), and then draw the travel-time curves of different head waves emanating from the first acceleration event. We find that the travel-time curve of the first arrival of $S_2S_1S_2$ head waves intersects the rupture front at a location closer to the second acceleration event than any of the other head waves (Figure 5.10). Such correlation is also valid for the other acceleration events (Figure 5.11). Note that we only plot the first arrivals of head waves based on ray theory, but the head waves with the largest amplitude actually arrive later (Figure 5.8b) with a delay influenced by the width of the fault zone and the characteristic frequency of the head waves. This explains why the period of oscillations increases nonlinearly with the increase of fault-zone width (Figure 5.5c). Even considering such complexity, it is clear that the $S_2S_1S_2$ head waves induce acceleration of the rupture front and control the period of oscillations. However, both P and S head waves contribute to the onset of rupture acceleration, as we will discuss later in Section 5.5.1.

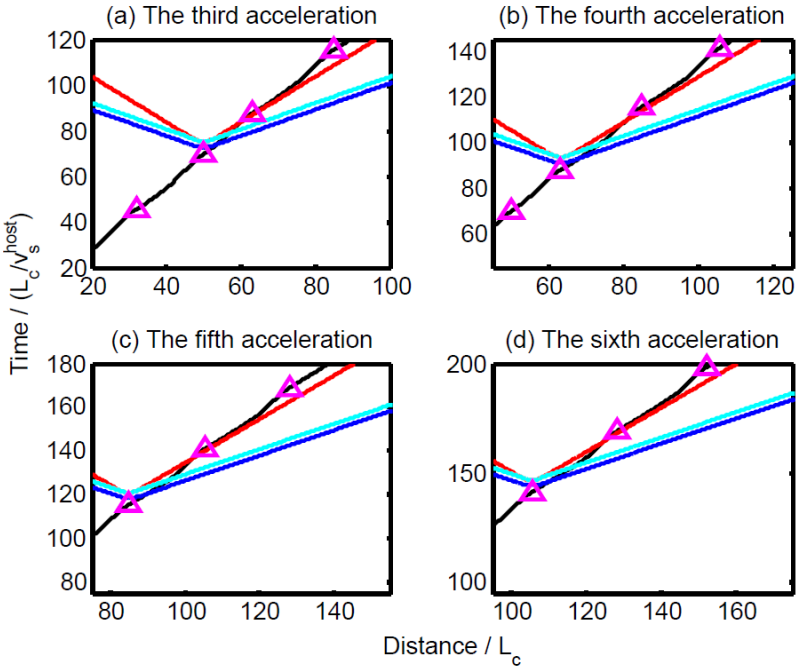

Figure 5.11: The correlation between the first arrivals of $S_1S_2S_1$ head waves (red solid lines) and the 3rd-6th acceleration events for the rupture in a fault zone of 30% velocity reduction and fault-zone width of 4 L_c. Travel-time curves of the first arrivals of $P_2P_1P_2$ and $S_2P_1S_2$ head waves are shown in blue and turquoise, respectively. Magenta triangles denote the rupture acceleration episodes.

The effects of the fault-zone velocity reduction on the wave field also lead to complicated rupture behaviors in the transition regime (Δv =40-60%). In addition to the $S_2S_1S_2$ head waves, $P_2S_1P_2$ head waves are also generated at the fault-zone interface and propagate at v_s^{host} when $v_p^{FZ} < v_s^{host}$ (Δv >42.3%). The interference of $P_2S_1P_2$ and $S_2S_1S_2$ head waves diminishes the amplitude of $S_2S_1S_2$ head waves and hence their capacity to induce oscillations of rupture speed. Thus, the oscillations become damped and finally disappear if the velocity reduction is larger than 50%. When Δv >53.8%, rupture speed is solely controlled by the P wave speed inside the fault zone, and waves that propagate at v_p^{FZ} and carry unfavorable stresses start to compete for rupture healing. When Δv >60%, the S_2P_2 and P_2S_2 reflected waves prevail and maintain the rise time equal to about a half of W^{FZ}/v_s^{FZ}.

5.5 Ruptures in Inelastic Fault Zones

5.5.1 Ruptures in Fault Zones with Attenuation

Natural fault zones have a more complex mechanical behavior than a purely elastic medium. Seismic waves propagating through damaged materials are attenuated due to scattering and absorption of energy. Seismic guided-wave studies suggest that Q inside fault zones is in the range of 10 to 60 for S waves (Table 5.1) although there is a trade-off between the estimations of fault-zone width, velocity and Q [Ben-Zion, 1998]. However, the potential effects of attenuation on earthquake rupture dynamics remain largely unexplored. Reflected waves in fault zones have a characteristic frequency of several Hz and may be severely attenuated if Q is low. Thus, it is crucial to assess the effects of attenuation on ruptures in fault zones.

Following Moczo et al., [2004], we incorporate attenuation by adding viscoelastic terms in the stress-strain relations:

$$\sigma(t) = M_u \cdot \varepsilon(t) - \sum_{l=1}^{n} M_u Y_l \zeta_l(t) \tag{5.13}$$

$$\dot{\zeta}_l(t) + \omega_l \zeta_l(t) = \omega_l \varepsilon(t) \tag{5.14}$$

where M_u, Y_l, $\zeta_l(t)$ and ω_l are the unrelaxed modulus, anelastic coefficient, anelastic function and relaxation frequency of the l^{th} viscoelastic mechanism, respectively. Seismic observations suggest that the quality factor Q is nearly constant over a certain frequency range [Aki and

Richards, 2002]. To realize an approximately flat Q in a numerical method, an adequate number of anelastic functions $\zeta_l(t)$ and relaxation frequencies ω_l are needed to cover the frequency range under interest. We find that three anelastic functions are sufficient to obtain a practically constant Q, with a relative error of less than 5%, over a broad frequency band with a maximum to minimum frequency ratio of 100. Anelastic coefficients can then be solved from the following equation given a certain frequency band ω:

$$Q^{-1}(\omega) = \sum_{l=1}^{n} \frac{\omega_l \omega + \omega_l^2 Q^{-1}(\omega)}{\omega_l^2 + \omega^2} Y_l \tag{5.15}$$

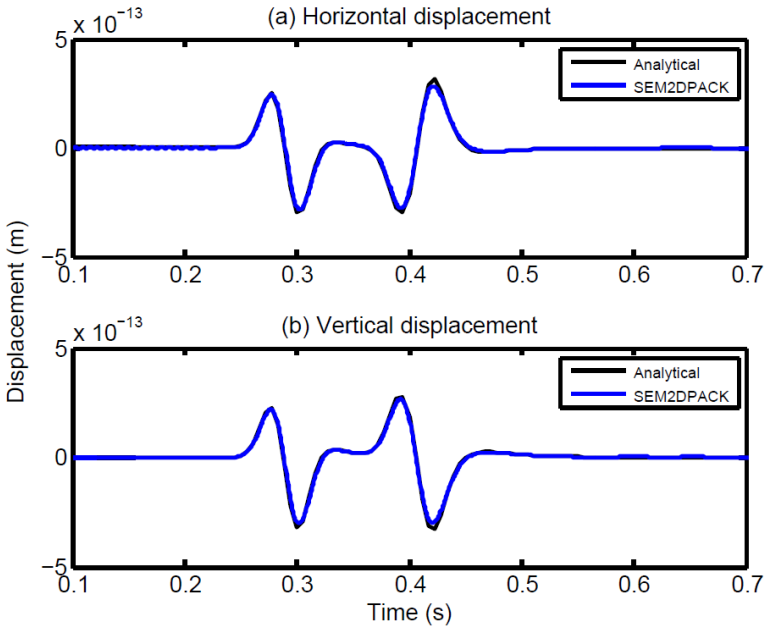

Figure 5.12: (a) Horizontal and (b) vertical displacements in a benchmark attenuation problem calculated by analytical solutions (black line) and SEM2DPACK with three inelastic functions (blue line). Given a vertical force source, the displacements are measured for a receiver located at $x = z = 500\ m$, when x and z are distances along and across the fault from the hypocenter, respectively.

The unrelaxed modulus is calculated from the anelastic coefficients and phase velocity [Equations (166) and (167) in Mozco et al., 2004]. We benchmarked our implementation by reproducing an example presented by Komatitsch and Tromp [1999], and compared our results to the analytical solutions by Carcione et al. [1988]. The benchmarked model has a constant Q_p=30 and

Q_s=20 over a frequency band of 1.8-180 Hz centered at 18 Hz, which is also the dominant source frequency. Overall, our numerical results agree well with the analytical solutions (Figure 5.12).

Table 3. Model parameters in models with attenuation

ρ (kg/m^3)	v_p^{host} (km/s)	v_s^{host} (km/s)	σ_0 (MPa)	τ_0 (MPa)	μ_s	D_c (m)	v_c (m/s)	α	β
2670	6.0	3.464	100	28.5	0.6	0.5	0.8	0.005	0.505

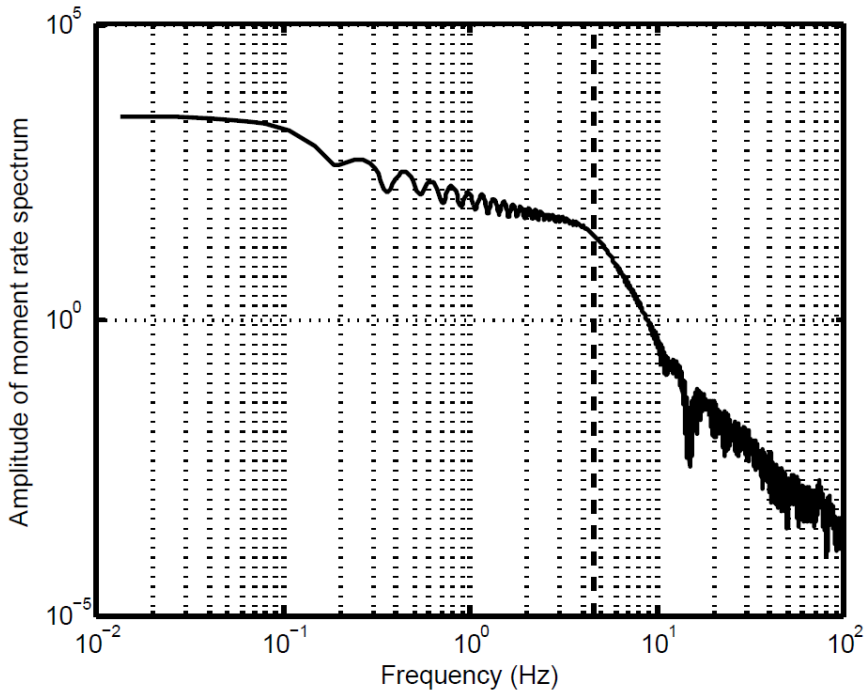

Figure 5.13: Moment rate spectrum of rupture in a 200 m wide fault zone with 50% velocity reduction when $Q = \infty$. The black dash-dot line denotes the frequency equal to 4.6 Hz.

We first illustrate the effects of attenuation on rise time by considering a 200 m wide fault zone with 50% velocity reduction. The material, stress and friction parameters are shown in Table 5.3. We present simulations with three different values of Q applied to both P and S waves: $Q = \infty$ (no attenuation), 40, and 10. When $Q = \infty$, the rupture has significant power up to ~4.6 Hz, above which the moment rate spectrum is less than 1% of its maximum (Figure 5.13). This corner

frequency is close to a half of the characteristic frequency of S waves in fault zones (v_s^{FZ}/W^{FZ}=8.66 Hz). For simulations with Q =40 and 10, we prescribe an almost constant Q from 0.1 to 10 Hz, which covers the dominant frequency range of the rupture. We find that rupture speeds hardly change with the decrease of Q: the reduction of rupture speeds is less than 2% from $Q = \infty$ to Q =10. Attenuation has a stronger effect on the shape of slip pulses (Figure 5.14). When $Q = \infty$ (equivalent to a purely elastic medium), slip alternately stops and resumes at the arrival of each group of reflected waves. When Q =10, the multiple slip-pulse episodes behind the first pulse merge into a single pulse modulated by damped oscillations. Thus, attenuation reduces the efficiency of reflected waves to unload the fault. However, peak slip rate of slip pulses in the three cases is still significantly larger than that in a homogeneous medium, and the period of the slip rate oscillations is largely unaffected by attenuation.

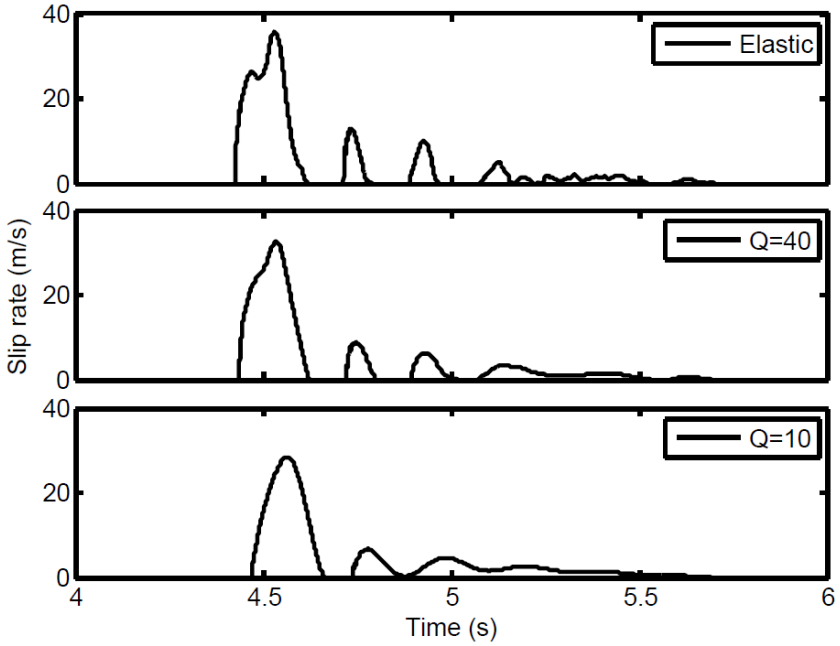

Figure 5.14: Slip rate functions at a distance of 14 km from the hypocenter for ruptures in 200 m wide fault zones with 50% velocity reduction and different Q.

Attenuation also influences the amplitude of head waves, which in turn can diminish their effect on oscillations of rupture speed. We illustrate this effect by considering a 1.6 km wide fault zone with 40% velocity reduction. As Q decreases, the first rupture acceleration episode beyond nucleation (marked by blue arrows in Figure 5.15) is postponed, but a reduced Q does not lead to

an obvious increase of the oscillation period (Figures 5.15a, 5.15b and 5.15c). The average oscillation period for different Q remain within 10% of each other. The amplitude of oscillations is severely reduced when Q =10. To find out how P and S head waves affect the first rupture acceleration episode, we examine cases when either Q_p or Q_s is reduced. By comparing Figures 5.15d and 5.15e to Figure 5.15a, we find that the first rupture episode beyond nucleation is postponed when either Q_p or Q_s is reduced, which suggests that both P and S head waves as well as their conversions contribute to the onset of rupture acceleration.

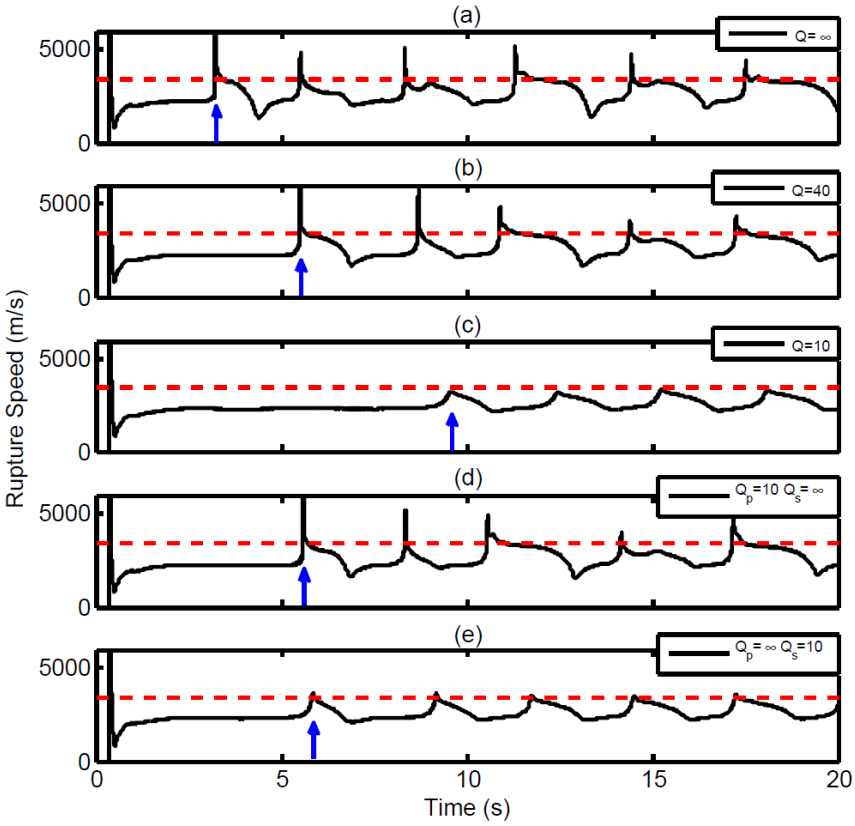

Figure 5.15: Rupture speed as a function of time for ruptures in fault zones of different Q. Similarly to the previous elastic cases, rupture speeds are measured based on the position and timing of the tail of the process zone. Red dashed lines denote v_s^{host} and blue arrows mark the first rupture acceleration beyond nucleation.

Overall, the strong effect of attenuation on the shape of the slip rate functions and its weak effect on rupture speed and rupture oscillation period is consistent with the fact that attenuation strongly affects wave amplitude but not wave speed.

5.5.2 Ruptures in Fault Zones with Off-Fault Plasticity

Damaged materials inside fault zones probably undergo plastic deformation during earthquakes. Previous simulations show that plastic deformation tends to occur on the extensional side of the fault in a homogeneous medium, except when the maximum principal compressive stress is oriented at an angle smaller than ~20° to the fault [Andrews, 2005; Templeton and Rice, 2008; Dunham et al., 2011a]. Duan [2008] studied the effect of fault zones with off-fault plasticity on dynamic ruptures and found plastic strain distributed on the extensional side. However, he assumed the same uniform background stress within and outside fault zones, which violates the boundary conditions at the interface between the fault zone and the host rock [Casey, 1980]. Reductions of elastic moduli in damaged fault zones in general induce rotation of the background stresses [Faulkner, 2006], which may generate different distributions of off-fault plastic deformation inside and outside fault zones. The generation of plastic deformation inside fault zones can affect rupture propagation and the mechanism of slip pulses. Also, plastic deformation can leave useful signatures on geological records and provide constraints on tectonic stresses [Di Toro et al., 2005; Ben-Zion et al., 2012]. Thus, it is worthwhile to reexamine dynamic rupture simulations inside fault zones with off-fault plasticity under mechanically consistent background stress.

We use the 2D Mohr-Coulomb failure criterion for the onset of off-fault yielding. For a given cohesion c and internal coefficient of friction $\tan\phi$, failure happens when the maximum shear stress $\tau_{max} = \sqrt{\sigma_{xz}^2 + [(\sigma_{xx} - \sigma_{zz})/2]^2}$ reaches the Coulomb threshold:

$$\tau_{max} \geq c\cos\phi - \frac{1}{2}(\sigma_{xx} + \sigma_{zz})\sin\phi \tag{5.16}$$

After the onset of off-fault yielding, plastic strain cumulates. Viscoplastic regularization is introduced to stabilize numerical solutions [Andrews, 2005; Xu et al., 2012; Gabriel et al., 2013]. The angle between the maximum principal compressive stress and the fault plane Ψ is determined by:

$$\Psi = \frac{1}{2}\tan^{-1}\left[\frac{2\sigma_{xz}}{\sigma_{zz} - \sigma_{xx}}\right] \tag{5.17}$$

When Ψ is fairly small (<~20°), off-fault plastic strain is concentrated in the compressive side of the fault. Otherwise, it mostly happens on the extensional side. This asymmetry of plastic deformation is valid when Ψ is uniform throughout the medium. However, stress is certainly not uniform in a medium with fault zones. The interface between the fault zone and host rock needs to satisfy the following conditions [Casey, 1980; Faulkner et al., 2006]:

$$\sigma_{zz}^{host} = \sigma_{zz}^{FZ} \tag{5.18}$$

$$\sigma_{xz}^{host} = \sigma_{xz}^{FZ} \tag{5.19}$$

$$\varepsilon_{xx}^{host} = \varepsilon_{xx}^{FZ} \tag{5.20}$$

where x and z are fault-parallel and fault-perpendicular directions, respectively (Figure 5.1). Thus, the boundary conditions require a rotation of regional stresses in the medium. This stress rotation causes a change of Ψ from the host rock to the fault zone, which can break the pure asymmetry of plastic deformations.

For simulations in this section, we employ a time-weakening nucleation procedure instead of an overstressed nucleation patch to avoid a discontinuity of Ψ along the fault. The size of the nucleation patch is prescribed to expand until half of the nucleation time and then shrink to zero [Andrews and Ben-Zion, 1997]. This nucleation procedure allows pulse-like ruptures to happen in a broad range of initial parameters [Gabriel et al., 2012]. Model parameters used in this section are shown in Table 5.4.

Table 5.4 Model parameters in models with off-fault plasticity

$\boldsymbol{\rho}$ $(\boldsymbol{kg/m^3})$	$\boldsymbol{v_p^{host}}$ $(\boldsymbol{km/s})$	$\boldsymbol{v_s^{host}}$ $(\boldsymbol{km/s})$	$\boldsymbol{\sigma_0}$ $(\boldsymbol{MPa})$	$\boldsymbol{\tau_0}$ $(\boldsymbol{MPa})$	$\boldsymbol{\mu_s}$	$\boldsymbol{D_c}$ $(\boldsymbol{m})$	$\boldsymbol{v_c}$ $(\boldsymbol{m/s})$	$\boldsymbol{\alpha}$	$\boldsymbol{\beta}$
2670	6.0	3.464	100	32.22	0.6	0.25	0.8	0.005	0.505

We first show a reference rupture simulation in a homogeneous medium with off-fault plasticity when Ψ=14.27°. Rupture in a homogeneous medium propagates as a self-sustaining pulse beyond ~3 km (Figure 5.16a), half of the prescribed nucleation size. An irregularly curved yielding zone grows solely on the compressional side, and saturates to a finite width (Figure 5.17a). This is

similar to previous findings concerning off-fault plastic deformation of a pulse-like rupture in a homogeneous medium [Xu et al., 2012].

We then consider a 200 m wide fault zone with 40% velocity reduction. The pre-stress angle Ψ rotates from 14.27° in the host rock to 45° within the fault zone. The rupture propagates as a sequence of multiple slip pulses (Figure 5.16b). Because Ψ =45° near the fault, the plastic yielding zone is located on the extensional side inside the fault zone (Figure 5.17b). This yielding zone also induces plastic deformation on the extensional side in the host rock, which forms a triangular-shaped yielding zone rather than a curvy-shaped one. Another yielding zone grows on the compressional side in the host rock, as expected for Ψ=14.27° from results in homogeneous media.

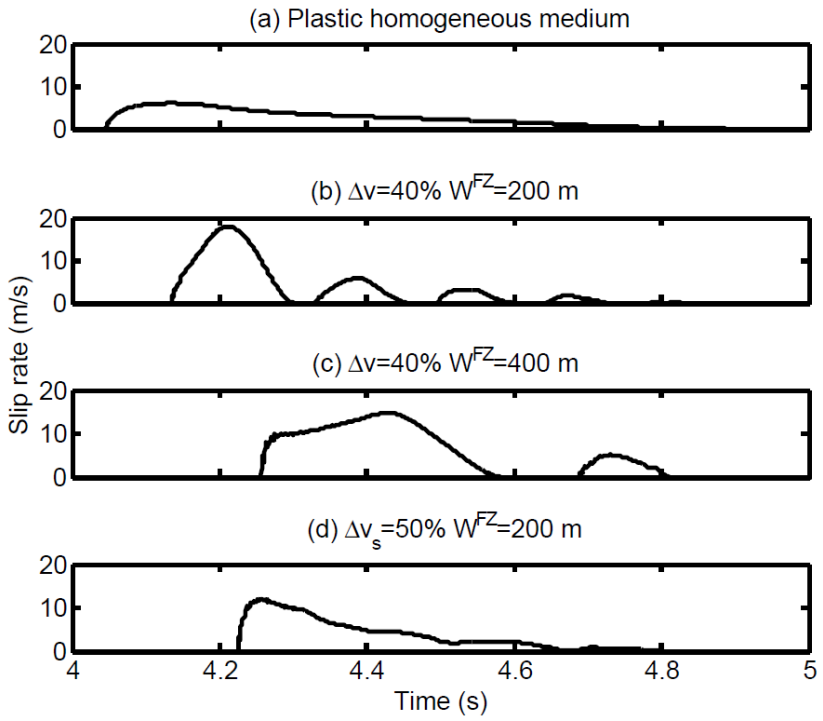

Figure 5.16: Slip rate functions at a distance of 9 km from the hypocenter for ruptures in (a) a homogeneous medium with off-fault plasticity and plastic fault zones of 40% velocity reduction with fault-zone widths of (b) 200 m and (c) 400 m, and (d) when only S wave velocity is reduced by 50% in the fault zone.

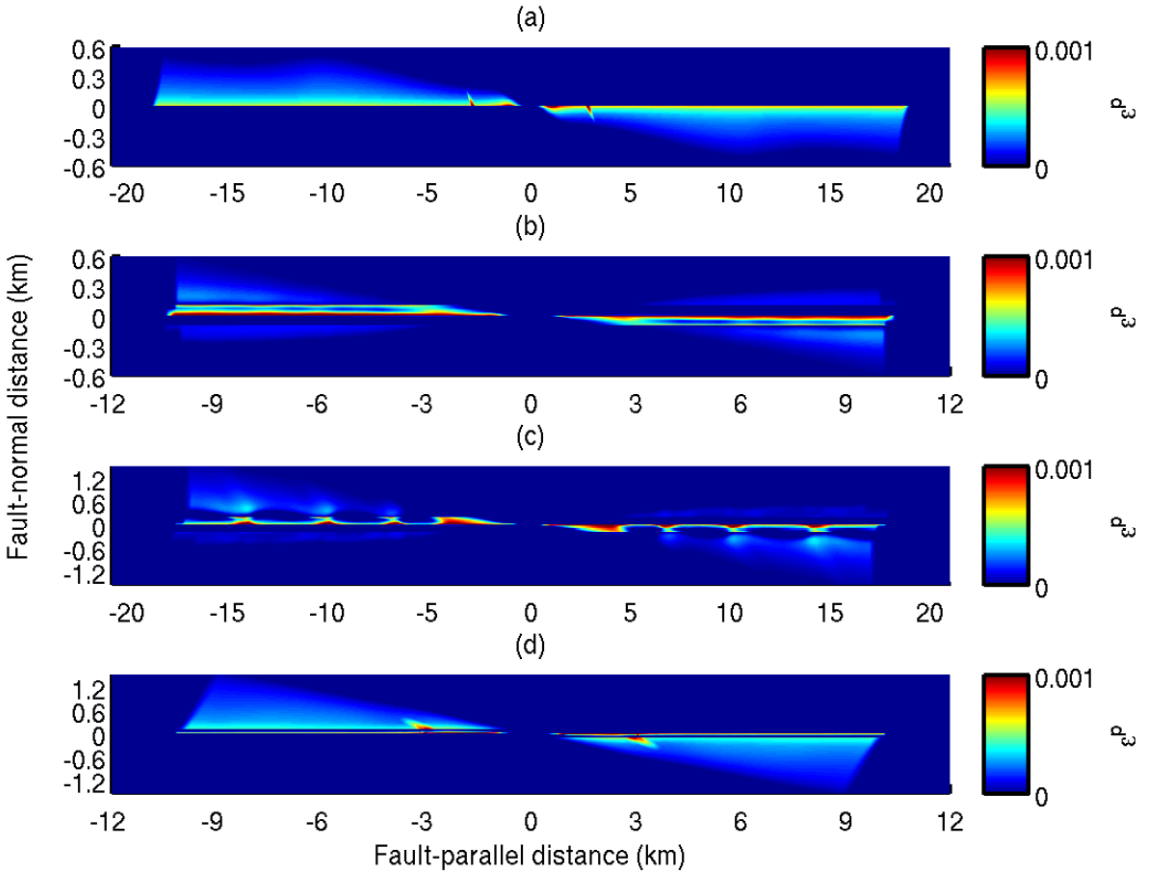

Figure 5.17: Plastic strain distributions in (a) a homogeneous medium and fault zones of 40% velocity reduction with fault-zone widths of (b) 200 m and (c) 400 m, and (d) when only S wave velocity is reduced by 50% in the fault zone.

We further investigate a 400 m wide fault zone with 40% velocity reduction. Rise time of the first slip pulse (Figure 5.16c) is twice of that in a 200 m wide fault zone (Figure 5.16b), suggesting again the proportionality between rise time and W^{FZ}, as found for ruptures in elastic fault zones. Similarly to the previous elastic cases, the oscillations of rupture speed become more pronounced as W^{FZ} increases. The intermittent accelerations of the rupture front induce highly concentrated off-fault plastic deformation, while decelerations only leave mild deformation (Figure 5.17c). Overall, the plastic yielding zone on the extensional side exhibits a spatially periodic pattern. This implies that ruptures in fault zones can leave a permanent and regular signature in the geologic record.

Seismic observations suggest that in natural fault zones the velocity reduction of S waves, Δv_s, is larger than that of P waves, Δv_p. For example, Li et al., [2007] suggest that Δv_p ≈42 % and Δv_s ≈58% at a depth of 4.5 km. We consider an extreme case when only v_s^{FZ} is reduced by 50% and Ψ=50.8° in the host rock. The Poisson's ratio increases from 0.25 in the host rock to 0.45 inside the fault zone. As a result, the principal stress rotates to a direction more parallel to the fault plane (Ψ=45°). Off-fault plastic deformation concentrates on the extensional side in both the fault zone and host rock (Figure 5.17d). The rupture propagates as a single pulse with damped oscillations instead of a train of multiple pulses (Figure 5.16d). This example shows the importance of Δv_p in the generation of slip pulses. Since the amplitude of P_2P_2 reflected waves is always favorable for slip, it also highlights the significant contributions of S_2P_2 and P_2S_2 reflected waves, as found for ruptures in elastic fault zones (Section 5.4).

5.6 Discussion

Our numerical and theoretical results indicate the significant potential effects of fault-zone waves on earthquake ruptures, even in the presence of attenuation and plasticity. Here we discuss these effects from the perspective of other plausible physical processes that may mitigate them or produce similar effects. We also highlight the significance of our findings from a broader perspective.

In our present study, we considered faults that bisect fault zones of uniform material properties. However, ruptures may also propagate along the boundary of fault zones [Brietzke and Ben-Zion, 2006] and, if the material contrast there is sharp, they can be viewed as bi-material ruptures. More generally, ruptures can run anywhere off the middle plane of the fault zone and the resulting asymmetric configuration can be viewed as a generalized bi-material rupture problem. Bi-material ruptures can propagate as slip pulses, due to the dynamic change of normal stresses at the bi-material interface [Weertman, 1980; Ben-Zion and Huang, 2002; Ampuero and Ben-Zion, 2008]. Thus, there is an inherent difference between our study and the studies of bi-material ruptures. Moreover, given a large enough nucleation size and no matter how wide the fault zone is, we obtain sustained slip pulses. In contrast, sustained bi-material pulses are found only when the nucleation size is smaller than the fault-zone width [Ben-Zion and Huang, 2002]. Although our study and the bi-material studies differ in some aspects, both find that fault zones can affect earthquake ruptures. For instance, the mild effect of fault zones on the modulation of slip rate was

also identified in the bi-material work of Ben-Zion and Huang [2002]. We note however that other fault zone effects studied here and in Huang and Ampuero [2011], including short rise times, oscillatory rupture speeds and enhanced supershear transitions, are more drastic and hence more amenable for observation of real earthquakes. Overall, bi-material ruptures and ruptures in symmetric fault zones studied in this paper are the two end members of ruptures in asymmetric fault zones [Dor et al., 2006]. More work is certainly warranted to develop a complete understanding of the interaction between bi-material effects and fault-zone wave effects. This topic is also relevant for subduction megathrusts overlain by low velocity sediment layers [Rowe et al., 2013].

Other mechanisms for the generation of slip pulses involve velocity-dependent friction [Perrin et al., 1995; Beeler and Tullis, 1996] and stress heterogeneities on the fault [Beroza and Mikumo, 1996]. Our current understanding of fault friction under seismic sliding velocity is mostly drawn from laboratory experiments as reviewed by Di Toro et al. [2011]. While laboratory results share some similarity with natural faulting, it is still a challenge to achieve the pressure, temperature, loading and fluid conditions of the natural environment. Hence, large uncertainties remain about the frictional constitutive equations and parameters of natural faults at seismogenic depth. Stress conditions on the fault can be inferred from either fault roughness, which is limited to the scale of field observations [Candela et al., 2011], or focal mechanism studies, from which only smoothed distributions of stresses are available due to limited resolution [Smith and Heaton, 2011]. Thus, it is challenging to relate the properties of slip pulses to friction parameters or stress heterogeneities in nature. In comparison, the properties of fault zone structures have been thoroughly studied in many faults (Table 5.1). As inferred from Figure 6b, the range of the rise time of ruptures in fault zones is ~ (0.5-2.5) W^{FZ}/v_s^{FZ}. Because natural fault zones are usually 100 to 400 m wide (except for the Calico fault zone, which is ~1.5 km wide), the rise time of slip pulses caused by fault-zone waves is in the order of 0.025-0.5 s given v_s^{FZ}=2 km/s. While this range is consistent with higher bounds inferred from seismological observations [Heaton, 1990], to resolve the short slip pulses induced by natural fault zones it is necessary to develop observations at frequencies of several Hz that overcome the obstruction by attenuation and scattering in the Earth's crust and the uncertainties of crustal structure.

Two other dramatic effects of fault zones are oscillations of rupture speed and the enhancement of supershear rupture transitions. Previous numerical simulations of ruptures in fault zones under

slip-weakening friction found supershear transitions enhanced within a certain range of fault zone widths [Harris and Day, 1997; Huang and Ampuero, 2011]. The current study, under strongly velocity-weakening friction, confirms this finding and suggests a richer behavior of rupture speed. Because ruptures are more sensitive to stress perturbations under strongly velocity-weakening friction, we see periodic oscillations of rupture speed in fault zones of 20%-40% velocity reductions. As the fault-zone width increases, we find a switch to supershear rupture speed caused by head waves. We confirm through simulations that supershear ruptures indeed happen in fault zones of 30%-42% velocity reductions. Supershear transition is expected to occur later than the simulation time in fault zones of 20%-30% velocity reductions. Although we showed that the supershear transition in fault zones operates via the same daughter crack mechanism as in homogeneous media, there are two main differences between supershear ruptures in a homogeneous medium and in fault zones. Firstly, in fault zones, supershear ruptures are possible even at stresses that are too low to allow supershear ruptures in a homogeneous medium. The increase of shear stresses caused by head waves is sufficient to trigger supershear rupture. Our work, combined with correlations between fault age and fault zone development [Savage and Brodsky, 2011], provides a mechanical rationale to interpret empirical correlations between the occurrence of supershear ruptures and other fault properties controlled by fault maturity, such as geometrical simplicity [Bouchon et al., 2010]. Specifically, our results suggest that supershear rupture is promoted by fault maturity because of the larger velocity reduction in the damaged fault zone. Secondly, as supershear ruptures happen in fault zones of 20-42% velocity reductions and approach v_p^{FZ}, they can propagate steadily at (1-1.39) v_s^{host}, which is an unstable range of supershear rupture speeds in a homogeneous medium [Das, 2010]. Such unexpected rupture speeds have been recently identified in real earthquakes within the Big Bear and Newport-Inglewood fault zones [Tan and Helmberger, 2010; Luo et al., 2010; Huang et al., 2013]. The implications of these theoretical and observational results on our macroscopic understanding of the earthquake energy balance remain to be developed.

Several additional complexities need to be considered for earthquakes in natural fault zones. One primary uncertainty in nature is the fault stress. To achieve healing, the stress change induced by reflected waves in the fault zone needs to overcome the dynamic stress drop, $\tau_0 - \tau_d$. Such insight can be gained through the relation between fault shear stress τ, initial stress τ_0 and slip rate D':

$$\tau(x,t) = \tau_0(x) + \phi(x,t) - \frac{G}{2v_s}D'(x,t) \qquad (5.21)$$

The term ϕ represents the stress transfer induced by elastodynamic waves radiated by previous slip [Zheng and Rice, 1998]. This term includes the stress induced by reflected waves in the fault zone. The last term is radiation damping [Rice, 1993], where G is shear modulus and v_s is shear wave speed. Well behind the rupture front $\tau \approx \tau_d$ and, in the absence of reflected waves, the mild slip rate gradient renders ϕ small. At the arrival of the reflected waves, ϕ becomes dominated by their unloading stresses, and the frictional strength remains near τ_d because slip decelerates too quickly for the state variable to evolve significantly. Slip arrest ($D' = 0$) then requires $\tau_0 < \tau_d$, and hence the stress perturbation induced by reflected waves must satisfy $-\phi > \tau_0 - \tau_d$. The peak stress carried by a wave radiated by the rupture front and reflected at the fault zone boundary scales with the strength drop in the process zone, $\tau_s - \tau_d$. It is further affected by factors controlled by fault zone properties, including reflection coefficient, geometrical spreading and attenuation. At background shear stresses lower than in the simulations presented here (relative to the strength drop), the stress drops that reflected waves need to counteract to enable healing are also smaller compared to the peak stresses carried by reflected waves, and thus the generation of slip pulses is more robust (Figure 4.6). For instance, we expect pulses at lower stress to be less affected by attenuation. Thus, the fault-zone wave mechanism for slip-pulses should be robust for natural faults that have mature fault zones and operate at low fault stress, e.g. the San Andreas Fault. We note however that the fault-zone pulse mechanism is not sufficient to achieve low absolute shear stresses consistent with the low heat flow near the San Andreas fault; that still requires severe frictional weakening.

Our findings of multiple slip pulses and oscillatory rupture velocity are based on a fault zone model with well-defined boundaries manifested by abrupt wave velocity contrasts. In natural fault zones, a seismological diagnostic of such sharp boundaries is the presence of multiple reflections in high-frequency body waves from small earthquakes, as observed in the Landers, San Jacinto and Calico fault zones [Li et al., 2007; Yang and Zhu, 2010; Yang et al., 2011]. Seismic wave velocity logs collected in the SAFOD borehole also indicate abrupt changes of both P and S waves in the San Andreas fault zone [Ellsworth and Malin, 2012]. However, not all fault zones have sharp interfaces. For instance, borehole data from the Nojima fault shows a progressive reduction of seismic wave velocities within the fault zone [Huang and Ampuero, 2011; Johri et al.,

2014]. In such fault zones multiple reflections and head waves do not exist, and hence multiple slip pulses and oscillatory rupture velocity are not expected. We conduct three simulations with fault zones that have an exponential distribution of both P and S wave speeds as a function of fault-perpendicular distance z: $v(z) = v^{host}(1 - \Delta v_{max} e^{-\frac{5z}{W^{FZ}}})$, where v^{host} is the P or S wave speed of the host rock and Δv_{max} is the maximum velocity reduction inside the fault zone (Figure 5.18). The three simulations have maximum velocity reductions of 40%, 60% and 80% when W^{FZ}= 2 L_c. We find ruptures in fault zones of larger velocity reductions feature lower rupture speeds and slip pulses with larger peak slip rate and longer rise time. Rupture speeds in all three simulations are steady and slower than the homogeneous rupture speed v_r^{host}. The peak slip rate of slip pulses in smooth fault zones is larger than that in a homogeneous medium due to reduced shear modulus. However, the periodicity of slip rate function and rupture speed does not exist in such fault zones with an exponential change of wave speeds.

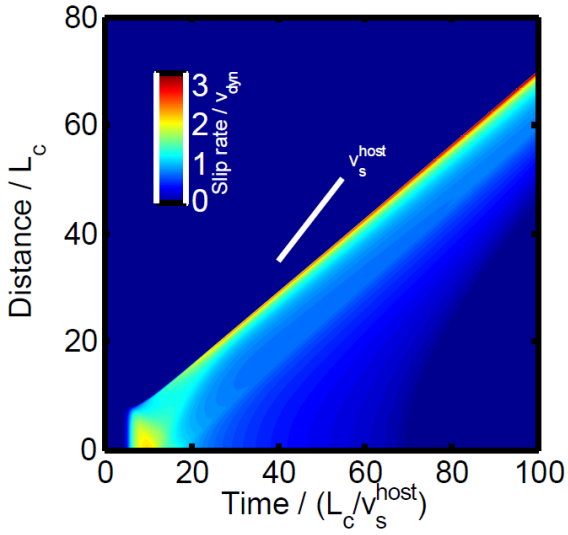

Figure 5.18: Spatiotemporal view of slip rate for a rupture in a fault zone with an exponential distribution of both P and S wave speeds as a function of fault-perpendicular distance. The simulation is for a fault zone with a maximum velocity reduction of 60% when $W^{FZ} = 2\ L_c$.

More work remains to be done to assess the effect of heterogeneous fault zone structures, with non-planar fault zone boundaries or non-uniform distributions of wave speed that may affect the constructive interference that controls the efficiency of the fault-zone trapped waves. The width of a fault zone can vary significantly along-strike, sometimes abruptly. The spatially periodic

pattern of plastic deformation presented in Section 5.5.2 also shows an example of coseismic inelastic process that can lead to along-strike variation of fault-zone width. Geometrical irregularities can scatter fault-zone waves away from the fault, but it may also produce focusing effects that contribute to rupture complexity. Scattering by small-scale 3D heterogeneities of highly anisotropic statistical properties, with longer correlation length in the direction of rupture propagation, may also help guide high-frequency waves, as proposed for subducting slabs [Furumura and Kennett, 2008; Chen et al., 2013], and promote pulse-like rupture in subduction earthquakes. Whether the heterogeneity of fault zone structure is enhanced or reduced by further earthquakes is an important question that requires multiple earthquake cycle simulations with off-fault damage.

Three-dimensional effects can also mitigate the efficiency of fault-zone waves. Unlike in 2D, the amplitude of fault-zone trapped waves in 3D decays with propagation distance due to geometrical spreading. However, this decay is inversely proportional to the square root of distance, which is much weaker than the exponential decay due to attenuation. Hence, our 2D simulations with attenuation contain a more severe mitigation ingredient than 3D geometrical spreading, and yet they present significant effects of fault-zone waves on rupture dynamics even with Q=10. A variety of 3D simulation results supporting these arguments will be reported elsewhere [Pelties et al., 2013].

Some of our results, for instance the conditions for supershear rupture, but not the rise time and the period of rupture oscillations, depend on fault zone width through its ratio to the (static) process zone size, $W^{FZ}/L_c = W^{FZ}\sigma_0(\mu_s - \mu_d)/G^{host}D_c$. In other words, some aspects of a rupture are only affected by fault zone structures whose width is larger than the process zone size. The most uncertain parameter in this non-dimensional number is D_c, the characteristic slip-weakening scale of the friction law. In elastic models, D_c may in reality represent a lumped parameter that encapsulates a variety of on-fault and off-fault dissipation processes, and could be scale-dependent (rupture-length-dependent), hence magnitude-dependent. This view would suggest that small and large ruptures are not equally sensitive to the presence of pre-existing fault zone structures [Huang and Ampuero, 2011] and that the sensitivity evolves during rupture growth. However, earthquake rupture can generate coseismically a damage zone whose width is sufficient to induce strong interactions with the rupture and affect the generation of slip pulses

[Xu et al., 2009]. This suggests that the fault zone effects described here are not restricted to pre-existing damage structures but their occurrence may be more universal.

5.7 Conclusions

Earthquakes are likely to happen in a heterogeneous medium. Fault zones are one form of heterogeneity that can have profound effects on earthquake ruptures. We find in this study that fault-zone waves in low-velocity fault zones with sharp boundaries are responsible for the following effects. Reflected waves can heal the ruptures and cause slip pulses. Their dominant rise time is controlled by the fault zone properties rather than by the friction parameters. Head waves can accelerate the ruptures periodically and induce supershear transitions. The supershear ruptures can run at speeds that would be forbidden for stable ruptures in a homogeneous medium. As the amplitudes of fault-zone waves depend on the velocity contrast of fault zones, we observe distinct rupture behavior as a function of the degree of fault zone damage. In fault zones with 20-40% velocity contrast, ruptures propagate with pronounced speed oscillations or undergo a supershear transition. In fault zones with 60-80% velocity reduction, ruptures propagate as steady-state pulses with constant rise time controlled by travel time across the fault zone width. We find that the fault zone effects are mildly affected by attenuation: it affects the shape of slip pulses and delays the supershear transition, but it hardly alters rise time, slip rate and rupture speed. The effects of fault-zone waves also persist in the presence of off-fault plasticity. Unlike in homogeneous media, the formation of yielding zones on both sides of the fault is facilitated by the rotation of background stresses inside the fault zone. The oscillations of rupture speed lead to spatially periodic patterns of plastic deformation. Our studies provide new mechanisms for the generation of slip pulses and supershear transition. Our findings make a contribution of considerable importance towards the understanding and future guidance of seismic and field observations. In regions where fault zone structures are well characterized, the effects of fault zones should be taken into account for future studies.

Chapter 6

SUPER-RAYLEIGH RUPTURES IN DAMAGED FAULT ZONES

Dynamic rupture theory predicts that in-plane shear cracks are unstable between the Rayleigh speed ($\sim 0.92\ v_s$) and $\sqrt{2}v_s$, where v_s is the S wave speed. However, detailed analyses of earthquakes suggest that some patches from large events as well as small events rupture at speeds within this unstable super-Rayleigh range. Here we show through dynamic rupture simulations that these rupture speeds become stable when earthquakes propagate in a damaged fault zone, a common feature of major faults. Moreover, supershear ruptures with speeds higher than the S wave speed are usually associated with large shear stresses on the fault. Here we find that supershear earthquakes may be more universal: in the presence of a fault zone, supershear ruptures occur even when fault stresses are low. Through detailed analysis of high-frequency data, we demonstrate that a damaged fault zone with laterally variable material exists for the 2003 Big Bear earthquake sequence in well-instrumented Southern California. Such heterogeneous fault zone structure results in variability of rupture speeds for small earthquakes. By linking the numerical simulations to detailed observations, we provide new insights into the basic physical processes of earthquake ruptures and also provide new ways to identify the fine structure of fault zones.

6.1 Introduction

Most earthquakes are reported to propagate well below the Rayleigh wave speed v_R ($\sim 0.7 - 0.9v_s$), but a few large earthquakes apparently ruptured segments with speeds higher than v_R (Figure 6.1). Dynamic rupture modeling and laboratory experiments conducted in homogeneous materials find stable ruptures can propagate at speeds less than v_R or greater than $\sqrt{2}v_s$ [Andrews, 1976; Das and Aki, 1977; Rosakis, 1999; Xia et al., 2004]. The latter speeds are referred to as stable supershear when in-plane shear cracks with a finite cohesive zone reach constant speeds between $\sqrt{2}v_s$ and v_p (P wave speed) as shown by the open squares and triangles in Figure 6.1. The range from v_s to $\sqrt{2}v_s$ is referred to as unstable supershear [Burridge et al., 1979; Samudrala et al., 2002a,b].

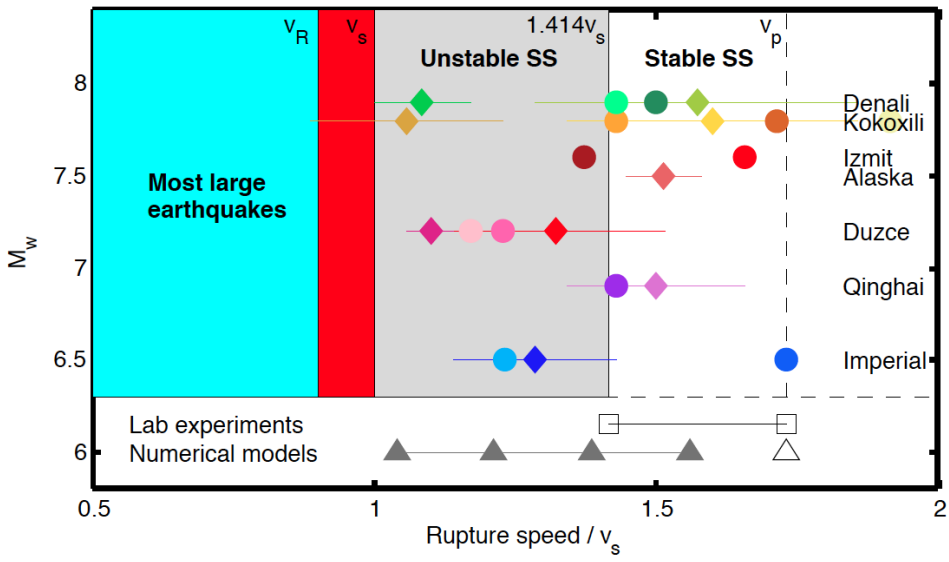

Figure 6.1: Supershear rupture speeds observed in large earthquakes (dots and diamonds), laboratory experiments (squares) and numerical models (triangles). For observed supershear earthquakes, each color corresponds to a separate study, a dot denotes a single estimation, a line denotes the range of estimated rupture speeds and a diamond indicates the mean value. The red strip shows the forbidden rupture speed range for in-plane shear cracks in homogeneous media. The grey patch lies in the region of unstable supershear (SS). For laboratory experiments, the two open squares display the limiting speeds: $\sqrt{2}v_s$ for strong interfaces and v_p for weak interfaces [Xia et al., 2004]. For numerical simulations, the open triangle shows that supershear rupture under slip-weakening friction law approaches v_p. Grey triangles display the supershear rupture speeds in fault zones of 10%, 20%, 30% and 40% wave velocity reduction relative to their host rock (also shown in Figure 6.2b).

However, segments of several large earthquakes are reported to propagate at speeds between v_s and v_p. Among them are 1979 M_w 6.5 Imperial Valley earthquake [Archuleta, 1984; Spudich and Cranswick, 1984], 1999 M_w 7.6 Izmit earthquake [Bouchon et al., 2001; Bouchon et al., 2002; Sekigchi and Iwata, 2002] and subsequent M_w 7.2 Düzce earthquake [Birgören et al., 2004, Bouin et al., 2004; Konca et al., 2010], 2001 M_w 7.8 Kokoxili earthquake [Antolik et al., 2004; Bouchon and Vallée, 2003; Robinson et al., 2006; Vallée et al., 2008; Walker and Shearer, 2009], 2003 M_w 7.9 Denali earthquake [Dunham and Archuleta, 2004; Ellaworth et al., 2004; Asano et al., 2005; Walker and Shearer, 2009], 2010 M_w 6.9 Qinghai earthquake [Wang and Mori, 2012] and 2013 M_w 7.5 Alaka earthquake [Yue et al., 2013]. The Kokoxili earthquake and Denali earthquake are likely to have propagated at speeds between $\sqrt{2}v_s$ and v_p, while the Imperial Valley earthquake and

Düzce earthquake probably ruptured more slowly with speeds in the range of unstable supershear. Moreover, the "red strip" between v_R and v_s in Figure 6.1a is the "forbidden speed range" for in-plane shear cracks [Burridge et al., 1979], but several moderate earthquakes have been observed to propagate at a speed near v_s [Luo et al., 2010; Tan and Helmberger, 2010] and possibly in the "forbidden speed range". We hereafter use super-Rayleigh ruptures to include both supershear ruptures and ruptures in the "forbidden speed range".

6.2 Dynamic Rupture Models with Damaged Fault Zones

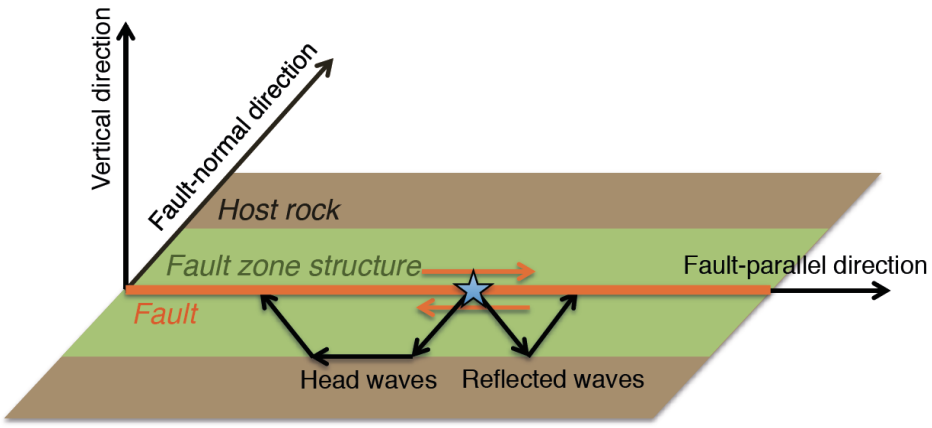

Figure 6.2: The cross section of a damaged fault zone (green) embedded in the host rock (brown) and bisected by a strike-slip fault (orange). Reflected waves and head waves are generated in the fault zone by the earthquake (blue star).

To explain these observations of super-Rayleigh ruptures, especially unstable supershear earthquakes, we take into account the damaged fault zones that encase many natural faults and feature lower elastic moduli compared to the host rock, as idealized in Figure 6.2. Structures of damaged fault zones are well characterized in several major faults (e.g., San Andreas, San Jacinto, Landers, Hector Mine, Calico, Nojima and North Anatolian faults) through waveform analysis of seismic data and borehole data from drilling projects [Ben-Zion and Sammis, 2003; Ben-Zion et al., 2003; Cochran et al., 2009; Ellsworth and Malin, 2012; Li et al., 2007; Yang and Zhu, 2010; Yang et al., 2011]. The fault zones are usually several hundred meters wide with 25-60% velocity reductions for both P and S waves. We investigate super-Rayleigh ruptures in damaged fault zones through dynamic rupture modeling using a 2D spectral element method [Huang and Ampuero, 2011; Huang et al., 2014].

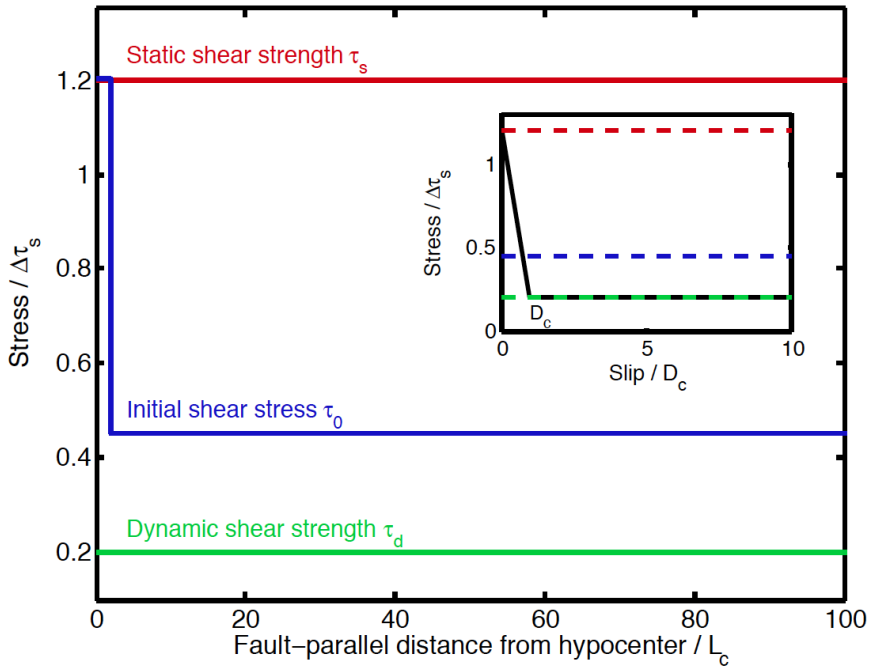

Figure 6.3: Fault stresses and slip-weakening friction in dynamic rupture simulations.

The fault bisects a symmetric fault zone with planar boundaries and relative velocity reductions Δv for both P and S waves. Hereafter, v_s denotes the S wave speed of *the host rock*. We only consider in-plane shear cracks that mimic the configuration of a strike-slip fault (Figure 6.2). Indeed all the observed super-Rayleigh ruptures are on strike-slip faults. Due to the symmetry of the problem considered here, the normal stress σ_0 remains constant. The initial shear stress has a uniform background value denoted by τ_0. We artificially start ruptures by setting an over-stressed nucleation patch, in which the initial shear stress is slightly larger than the static shear strength τ_s (Figure 6.3). The remaining part of the fault begins to rupture spontaneously when stress reaches the static shear strength τ_s. The whole fault is governed by a linear slip-weakening friction law (inset of Figure 6.3) characterized by the following parameters: static shear strength τ_s, dynamic shear strength τ_d and critical slip distance D_c. The fault stress drops from static shear strength τ_s to the dynamic shear strength τ_d over the critical slip distance D_c, and then stays at τ_d. According to typical laboratory values of static and dynamic friction coefficients, we set $\tau_s = 0.6\ \sigma_0$ and $\tau_d = 0.1\ \sigma_0$. The initial shear stress is given by the ratio of strength excess to stress drop $= (\tau_s - \tau_0)/(\tau_0 - \tau_d)$ [Das and Aki, 1977].

To preserve the generality of the problem, we use dimensionless quantities for space x, time t, slip D, slip velocity D' and stress τ:

$$\tilde{x} = x/L_c \tag{6.1}$$

$$\tilde{t} = tv_s/L_c \tag{6.2}$$

$$\widetilde{D} = D/D_c \tag{6.3}$$

$$\widetilde{D'} = D'/v_{dyn} \tag{6.4}$$

$$\tilde{\tau} = \tau/\Delta\tau_s \tag{6.5}$$

Given shear modulus G, we define the following parameters:

$$L_c = GD_c/\Delta\tau_s \tag{6.6}$$

$$v_{dyn} = v_s D_c/L_c \tag{6.7}$$

$$\Delta\tau_s = (\mu_s - \mu_d)\sigma_0 = \tau_y - \tau_d \tag{6.8}$$

The dimensionless density, shear modulus and critical slip distance are all 1, and the dimensionless normal stress is 2. Our results can be applied to a variety of initial conditions by converting these dimensionless quantities. For example, if $G = 30\ GPa$, $\Delta\tau_s = 30\ MPa$ and $D_c = 0.1\ m$, we find $L_c = 100\ m$ and the simulations shown in Figure 2b correspond to a 400 m wide fault zone.

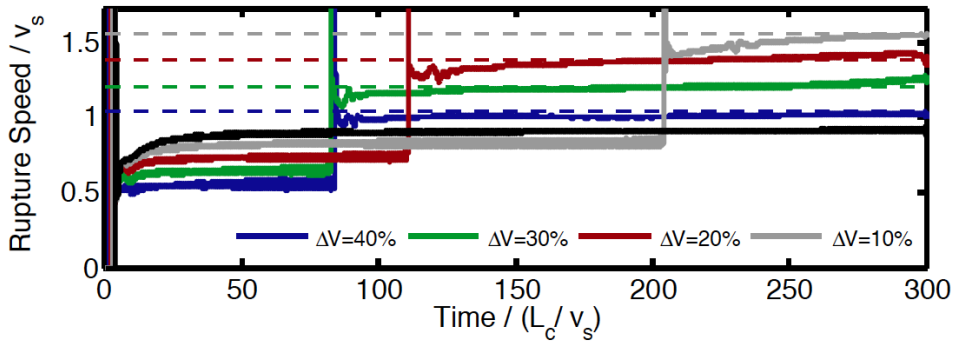

Figure 6.4: Rupture speed normalized by the S wave speed of the host rock v_s as a function of time. For the given stresses ($S = 3$), rupture speed approaches the Rayleigh wave speed in homogeneous media (black), but accelerates to supershear rupture speeds in a fault zone of width 4 L_c with different velocity reductions (color). The dashed lines show the P wave speeds in various fault zones.

Previous numerical simulations with slip-weakening friction find that ruptures in a homogeneous medium and initial stress field approach P wave speed if supershear transition happens [Andrews, 1976; Das and Aki, 1977; Andrews, 1985] (open triangle in Figure 6.1). Here, we find that super-

Rayleigh ruptures propagate at a speed around the P wave speed of the fault zone [Huang et al., 2014], i.e., between $0.9v_s$ and $1.559v_s$ for fault zones of 10-48% velocity reductions (Figure 6.4 and grey triangles in Figure 6.1). The transition length of supershear rupture is found to increase with decreasing velocity reduction. In particular, rupture speeds in fault zones of 18-42% velocity reductions lie in the range of unstable supershear, and ruptures in fault zones of 42-48% velocity reductions can propagate stably in the "forbidden speed range". Thus, the super-Rayleigh speeds between the Rayleigh wave speed and $\sqrt{2}v_s$ are unstable for ruptures in homogeneous media, but stable for ruptures in damaged fault zones.

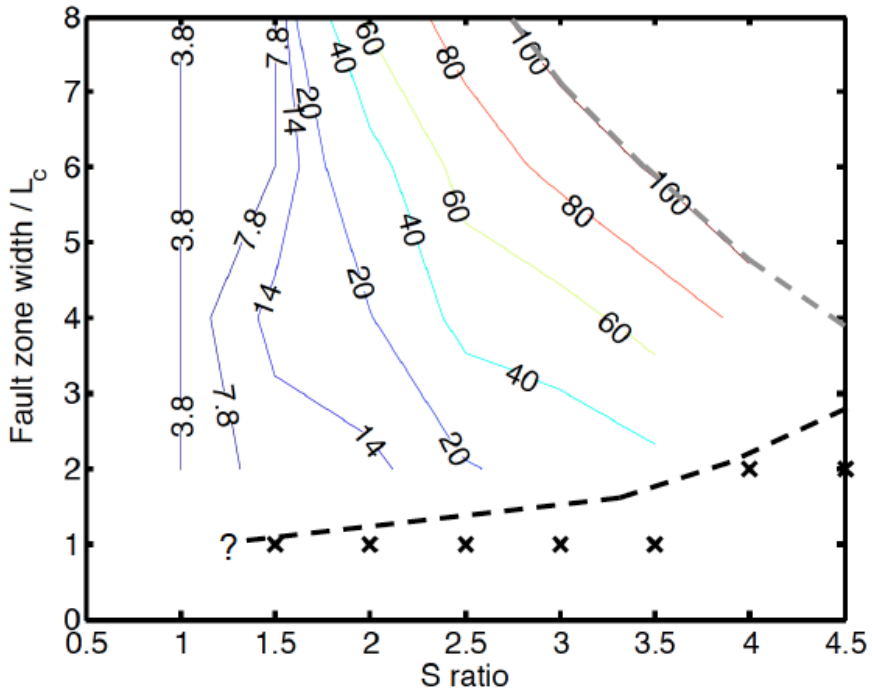

Figure 6.5: Contours of supershear transition lengths (the distances that ruptures propagate before accelerating to supershear speeds) in damaged fault zones of 30% velocity reduction as a function of S ratio and fault zone width. The transition lengths and fault zone widths are normalized by L_c. The gray dashed line on the top right (overlaid with the contour of 100 L_c) is the boundary above which supershear transition happens further than 100 L_c. The black dashed line near the bottom shows the boundary below which supershear transitions are not observed. The crosses denote the fault zone widths and S ratios for which oscillations of rupture speed occur.

One important parameter that controls the supershear transition in homogeneous media is the initial background stress, τ_0, quantified non-dimensionally by $S = (\tau_s - \tau_0)/(\tau_0 - \tau_d)$. The closer the initial shear stress τ_0 is to τ_s and the further τ_0 is from τ_d, the easier ruptures accelerate to

supershear speeds. The critical *S* ratio for supershear transition in homogeneous media is 1.77 for in-plane shear cracks [Andrews, 1985] and 1.19 for 3D ruptures [Dunham, 2007] under slip-weakening friction. However, we find that the supershear transition happens in damaged fault zones even when the *S* ratio is much larger than 1.77 for a certain range of fault zone widths (Figure 6.5). Such supershear transition is facilitated by stress perturbations carried by head waves that can refract back to the fault and interact with the rupture front. If the fault zone is too narrow, the wavelengths of head waves are shorter than the critical nucleation lengths of daughter crack (Figure 5.5), which prevents the permanent transition to supershear, and rupture speeds start oscillating instead (the region below the black dashed line in Figure 6.5). However in wider fault zones, the head waves need to propagate for a longer distance and the transition to supershear rupture may occur too late to be observed. For example, ruptures in a 6 L_c wide fault zone of 30% velocity reduction can accelerate to supershear speeds at a distance of 100 L_c when $S = 3.5$, which is only observable if the total rupture length is longer than 100 L_c. Moreover, we find that the transition lengths of supershear ruptures are also shortened (e.g., by a half when $S = 1$) in damaged fault zones than in a homogeneous medium when $S < 1.77$.

Our results predict that, if head waves are efficiently generated, supershear ruptures with unstable speeds should be observed in mature faults that operate at low average shear stress. Among the observed supershear earthquakes (Figure 6.1), the Düzce and Imperial Valley earthquakes were likely to happen inside fault zones. Indeed, the North Anatolian fault zone lies in the Karadere–Duzce branch near the source region of the Düzce earthquake [Ben-Zion et al., 2003]. In the next section, we will demonstrate an example of the coexistence of unstable super-Rayleigh earthquakes and damaged fault zones in Southern California.

6.3 The Variability of Rupture Speeds and Fault Zones

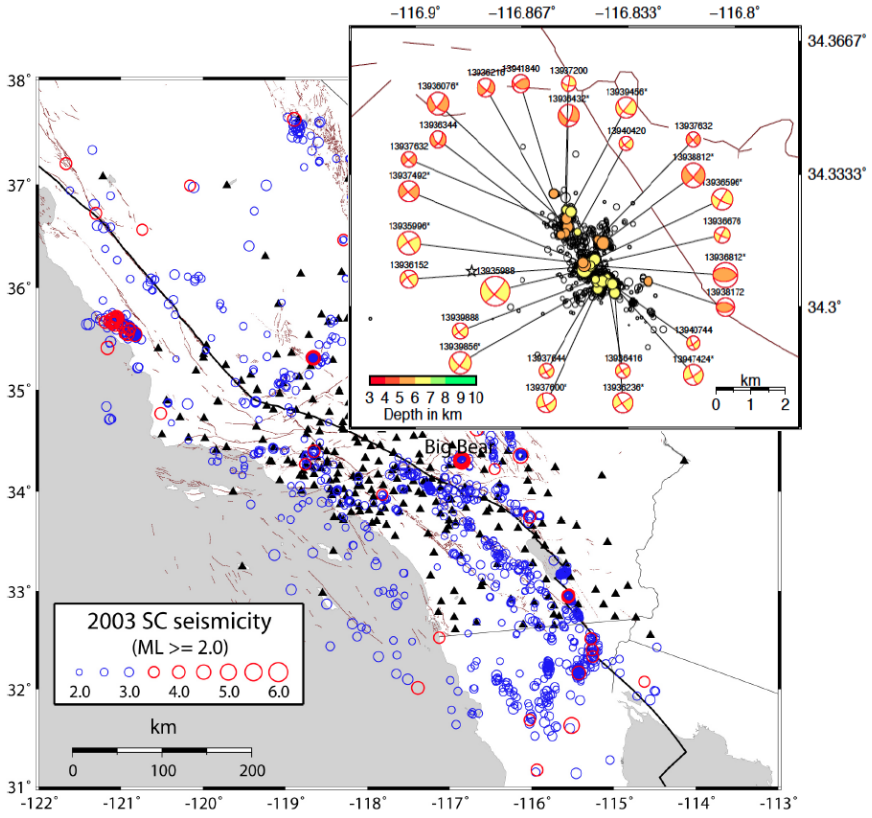

Figure 6.6: Southern California earthquakes in 2003 (circles and crosses) along with the broadband Trinet stations (triangles) [Tan and Helmberger, 2007]. The inset shows the 2003 Big Bear sequence with selected source mechanism solutions [Tan and Helmberger, 2010].

We investigate the correlation between fault zone structures and rupture speeds by analyzing high-frequency data, which is provided by dense arrays with abundant seismicity in Southern California (Figure 6.5). In particular, we test the variability of rupture speeds predicted by our dynamic rupture models in light of seismological observations of the well-studied 2003 Big Bear sequence, displayed in the inset. Rupture speeds and horizontal fault dimensions of several Mw 3.3-4.3 earthquakes were resolved by calibrating paths using small events [Tan and Helmberger, 2010] (Figure 6.6a). The results indicate that events away from the main fault (cross-faulting) have low rupture speeds in contrast with those near the main shock. We hypothesize that only the latter ruptured in a mature damaged zone related to the main fault. In particular, event A reached a speed of 3.62 km/s, which is inside the "unstable" supershear range given v_s= 3.5 km/s. It is also possible

that event A ruptured in the "forbidden speed range", as the lower bound of its rupture speed is 3.28 km/s for an extreme case. However, neither of these rupture speeds could be explained by ruptures in a homogeneous medium. Super-Rayleigh ruptures in damaged fault zones, which approach the P wave speeds of the fault zones, could naturally explain such rupture speeds. Considering the P wave speed in host rock in this area, v_p= 6 km/s [Tan and Helmberger, 2010], the rupture speed of event A (3.62 km/s) is consistent with supershear rupture in a fault zone with a velocity reduction of 40%.

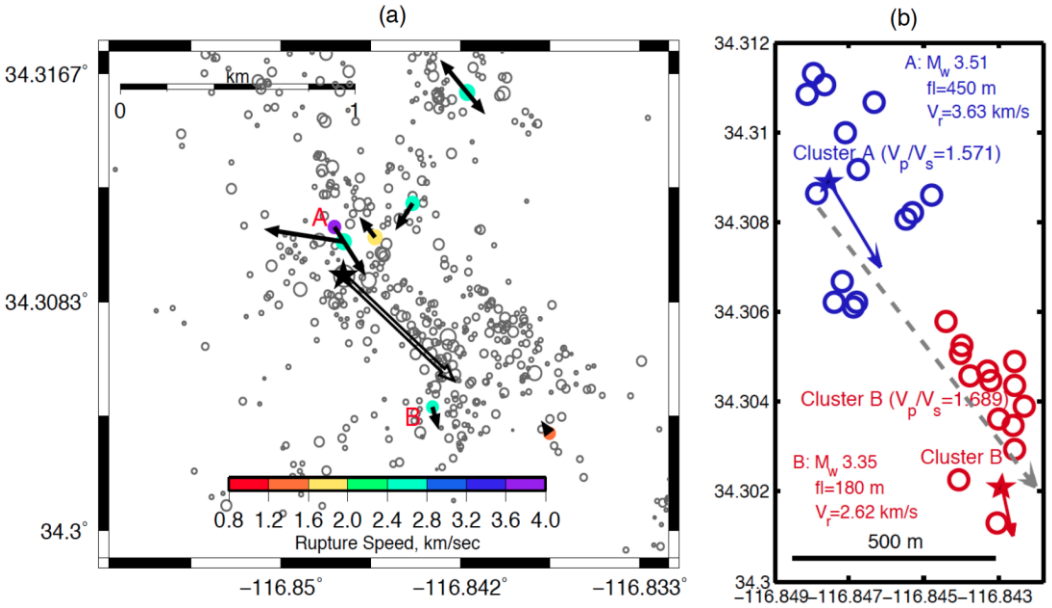

Figure 6.7: (a) Figure modified from Figure 10 in [Tan and Helmberger, 2010]. Rupture speeds of several Mw 3.3-4.3 earthquakes (including Events A and B) in the 2003 Big Bear sequence are indicated by bottom color bar. The arrows indicate the rupture propagation directions, and their lengths are proportional to the rupture lengths. The open arrows indicate the speculated rupture propagation for the mainshock. The open dots are relocated seismicity from Chi and Hauksson [2006]. (b) Map of clusters of Mw 2.1-3.1 earthquakes around event A (blue star) and event B (red star) and inferred Vp/Vs ratio of each cluster. Event locations are from [Hauksson et al., 2012]. The moment magnitudes, M_w, rupture lengths, fl, and rupture speeds, V_r, of events A and B are shown beside the clusters. The arrow associated with each star denotes the rupture propagation direction. The gray dashed arrow displays the approximate rupture propagation direction of the 2003 Mw 5.0 Big Bear mainshock.

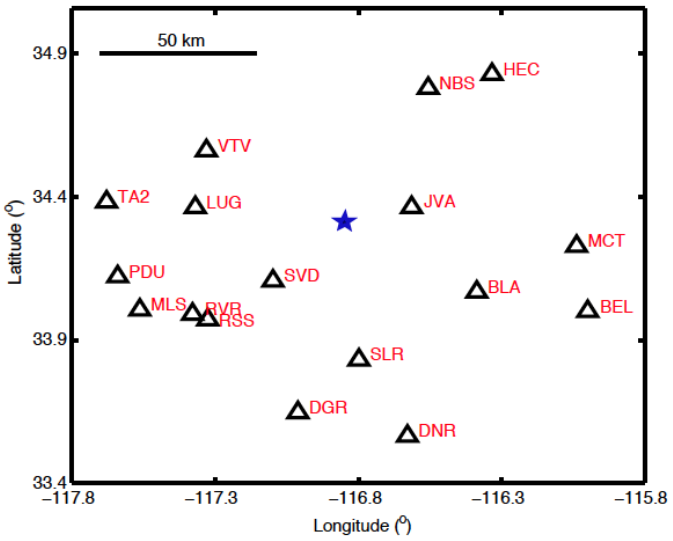

Figure 6.8: Station map. The star denotes the location of cluster A.

In contrast, event B propagated at a sub-Rayleigh rupture speed of 2.62 km/s. Such variations of rupture speeds could be caused by the along-strike heterogeneities of fault zone materials, i.e., a more damaged fault zone around event A. In order to investigate whether such heterogeneities exist along Big Bear fault, we measure the local Vp/Vs ratio (related to Poisson's ratio) which is an indicator of cracked materials [Shearer, 1988; Takei, 2002]. Our estimation of Vp/Vs ratio is unaffected by the inaccuracy of earthquake locations. We use data from two clusters of smaller earthquakes (Mw 2.1-3.1) around events A and B, respectively, in the 2003 Big Bear sequence (Figure 6b). The depths of these smaller earthquakes are around 4-6.5 km, which form a three-dimensional distribution and provide better resolution for Vp/Vs ratio inversion [Lin and Shearer, 2007]. Moreover, the cluster size (several hundred meters) is much smaller than the cluster-station distance (several tens of km) (Figure 6.7), and the ray paths from two nearby earthquakes to one station are considered as parallel. Thus, the Vp/Vs ratio inverted from each pair of events can be expressed as follows:

$$\frac{V_p}{V_s} = \frac{\Delta l^i / V_s}{\Delta l^i / V_p} = \frac{\Delta t_s^i}{\Delta t_p^i} \tag{6.9}$$

where Δl^i is the difference in the ray-path distances between each pair of events given a certain station i, and Δt_p^i and Δt_s^i are differential P- and S-wave travel times to station i, respectively. Details of the derivations are described by Lin and Shearer [2007].

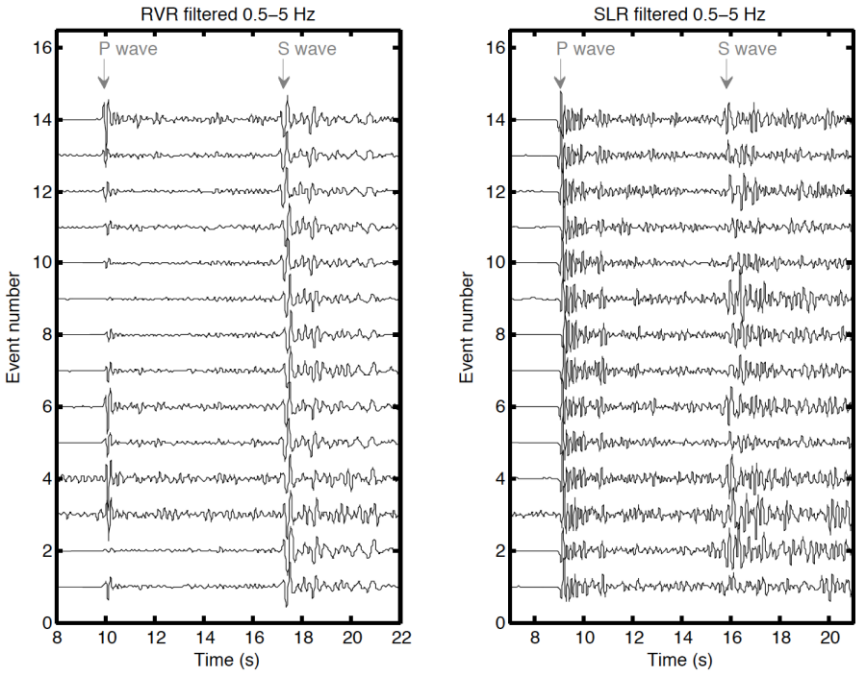

Figure 6.9: Filtered P and S waves from cluster A recorded by stations RVR and SLR.

Data at each station is filtered by a four-pole Butterworth filter with a frequency band of 0.5-5 Hz, lower than the corner frequency of these earthquakes. The filtered data has very similar waveforms for both P and S waves (Figure 6.8). We calculate differential P- and S-wave arrival times by waveform cross-correlations at each station. We use event pairs with a cross-correlation coefficient larger than 0.85 for at least five stations. The measured differential arrival times are demeaned for each event pair to eliminate the effect of differences of origin times of the earthquakes. This in fact yields differential P- and S-wave travel times, which satisfy Equation 6.9. We then apply a robust linear regression method [Huber, 1981] to the differential P- and S-wave travel times to obtain the Vp/Vs ratios (Figure 6.9). The standard errors are estimated by randomly resampling the differential times 10000 times (Figure 6.10). We find that cluster A shows an anomalously low Vp/Vs ratio of 1.571 ± 0.043 while the other cluster has a Vp/Vs ratio of 1.689 ± 0.035. A previous study using the same method finds a median Vp/Vs ratio of 1.673 ± 0.022 in Southern California [Lin and Shearer, 2009]. Compared to the region of cluster B, the relatively low Vp/Vs ratio inferred for cluster A suggests the presence of highly cracked rocks, i.e. a more damaged fault zone.

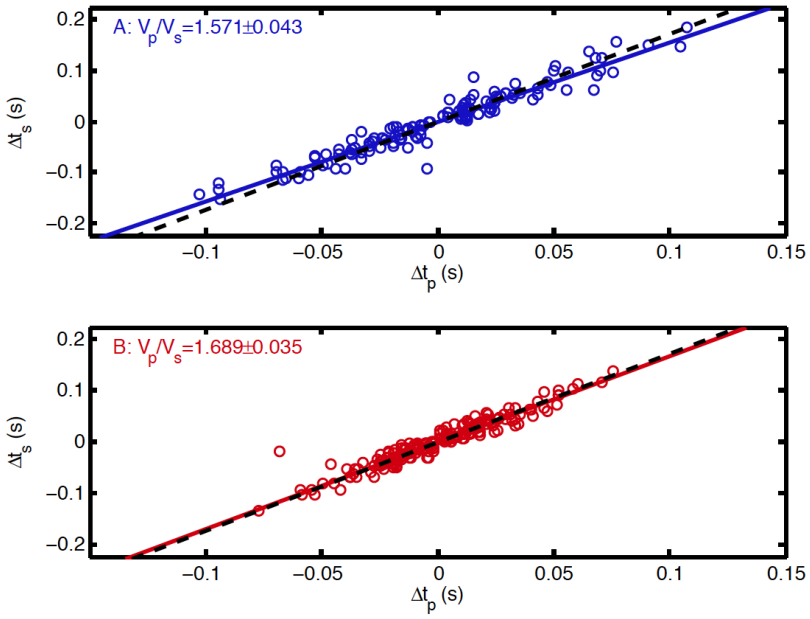

Figure 6.10: Vp/Vs ratio inversion results for clusters A and B based on differential P- and S-wave travel times of event pairs. The slope of each solid line provides the estimated Vp/Vs ratio, while the black dashed lines have a slope of $\sqrt{3}$.

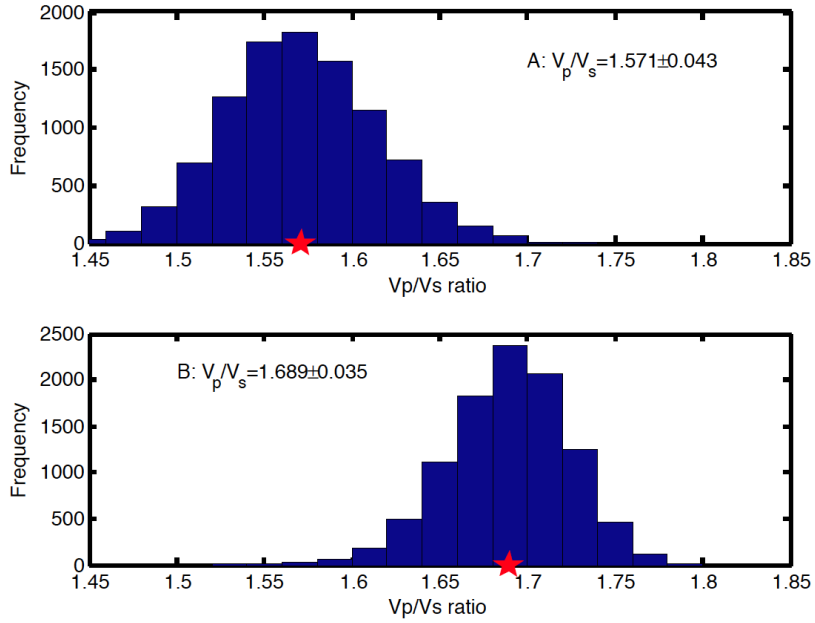

Figure 6.11: Standard errors of Vp/Vs ratio inversion results for clusters A and B, computed by bootstrapping method with differential times randomly resampled 10000 times.

6.4 Amplified High-Frequency Energy along a Fault Zone

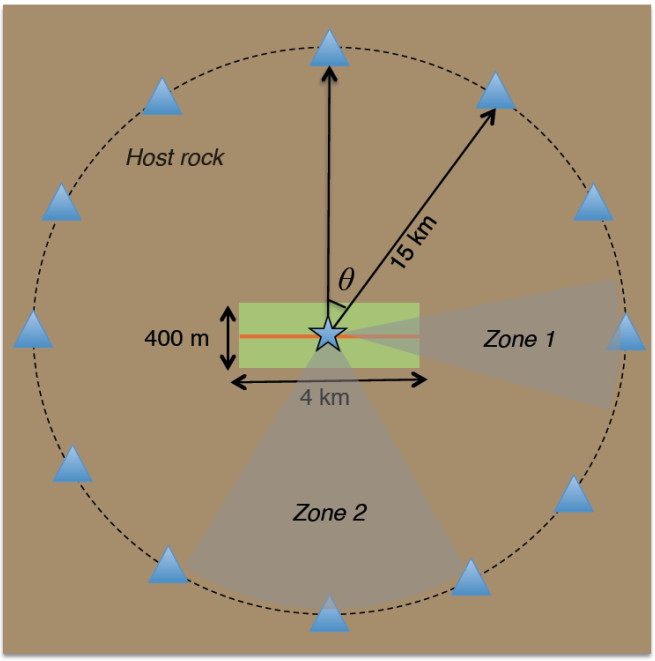

Figure 6.12: Configuration of the simulation of waves radiated by an earthquake (blue star) inside a damaged fault zone (green) embedded in a host rock (brown). The stations (blue triangles) are 15 km away from the source and are located at an azimuth of θ from the fault normal. Stations at $\theta = 75^{o}$-105^{o} are in Zone 1 and stations at $\theta = 150^{o}$-210^{o} are in Zone 2.

As a validation, we use kinematic models (Figure 6.11) to predict waveform differences between earthquakes in homogeneous media and inside fault zones, and compare with the data of cluster A. Here we assume that the differences of path effects between various sources and receivers can be neglected and refer the entire wavetrain as the effective source function. We examine the effective source functions as a function of azimuth (Figure 6.12), which are calculated from a double-couple source with a central frequency of 10 Hz, near the corner frequency of the small events in cluster A. Similarly to previous dynamic rupture simulations, a fault zone with lower seismic velocities is embedded in the host rock (v_p=6 km/s an v_s=3.5 km/s), but it has a finite length of 4 km rather than extending to infinity (Figure 6.11). Both P and S wave speeds are 40% lower for a length of 2 km in the center and then increase linearly to the host rock speeds in a 1 km wide transition zone in both

ends. Without the transition zones, waves are scattered by the abrupt ends of the fault zone and cause large arrivals at t ~ 3-3.2 s (Figure 6.13). We set receivers over all azimuths at a 15 km distance from the source, far enough to separate the arrivals of P and S waves. Given the purely elastic host rock with uniform material properties in the synthetic test, P waves should look the same for more distant stations, except for having weaker amplitudes.

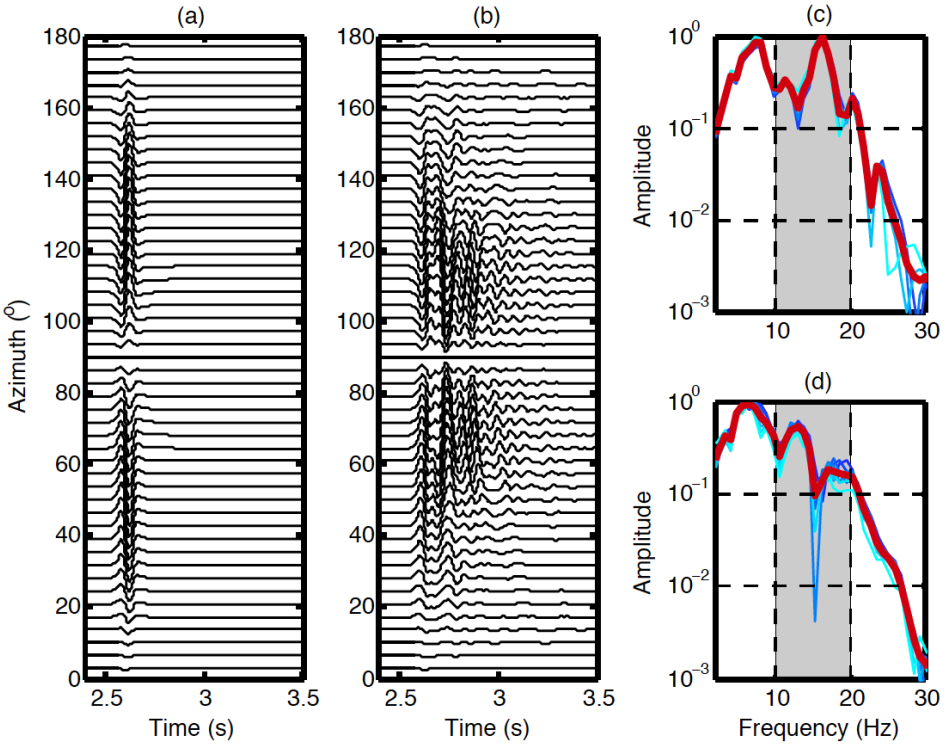

Figure 6.13: P waves recorded by stations at $\theta = 0^o$-90^o for a double couple source (a) in homogeneous media and (b) in a 400 m wide fault zone. Note that the records at $\theta = 90^o$-180^o at $\theta = 0^o$-90^o are symmetric with respect to the fault. Velocity spectra of P waves recorded by stations every 3^o in (c) Zone 1 and (d) Zone 2, except nodal stations. Red solid lines show the average velocity spectra.

As found in some previous fault zone studies and 3D simulations [Ben-Zion, 2002; Jahnke et al., 2002], the fault zone boundaries generate secondary arrivals that are caused by waves trapped inside the fault zone, i.e., reflected from the interfaces between the fault zone and the host rock. Moreover, the characteristic period of fault zone reflected P waves is shorter in the directions near fault strike (Zone 1). We calculate the velocity spectra of P waves recorded at each station by taking a 1 s window starting immediately before the first P arrivals. At all azimuths, the spectra of P waves show a peak around 5-10 Hz, near the corner frequency of the source (Figure 4c). But the spectra of

P waves recorded by stations in Zone 1 show second peaks at 10-20 Hz (grey patch in Figure 4c), which do not exist for stations far from fault strike (Zone 2), regardless of whether the fault zone is ended smoothly (Figure 6.12c) or abruptly (Figure 6.13b).

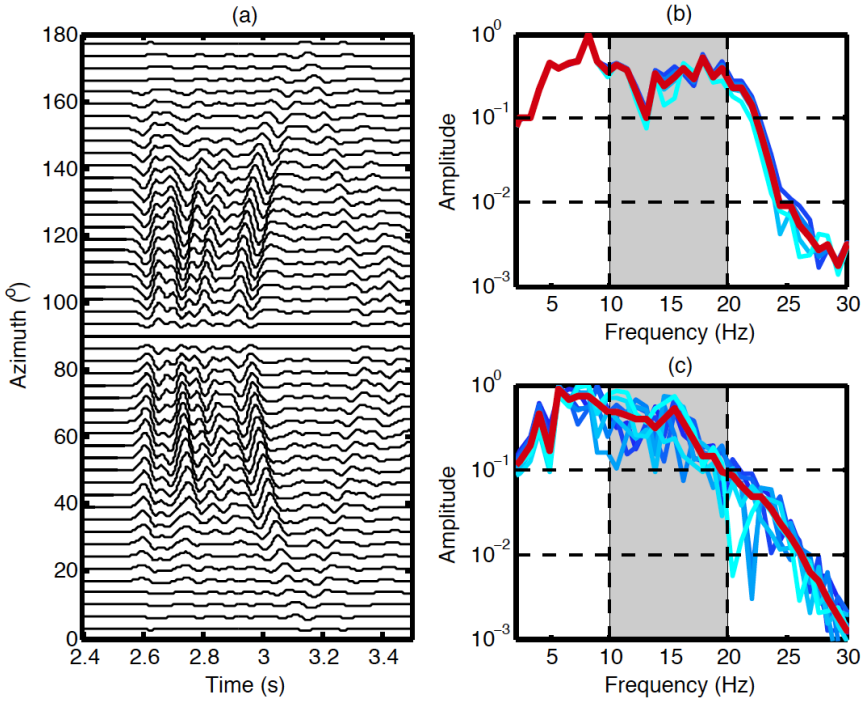

Figure 6.14: (a) P waves recorded by stations at $\theta = 0^{o}$-180^{o} for a double couple source in a 400 m wide fault zone with abrupt lateral ends and synthetic P wave velocity spectra every 3^{o} in (b) Zone 1 and (c) Zone 2, except nodal stations. Red solid lines show the average velocity spectra.

We then analyze the spectra of P waves of cluster A in the 2003 Big Bear sequence, computed at each station on a 1 s long window starting immediately before the P wave arrival. Similarly to the kinematic models, stations close to fault strike show an additional prominent spectral peak around 10-20 Hz (Figure 6.14). These second spectral peaks are probably not caused by the propagation paths, as they are observed on stations that span a range of azimuths (SLR, DGR and DNR stations in Figure 6.7). Moreover, these stations lie on hard rocks [Tan and Helmberger, 2007], which rules out site-specific ground motion amplification at 10-20 Hz. Through trial and error in kinematic models (Figure 6.15), we find that synthetic spectra from a 400 m wide fault zone with a velocity reduction of 40% are in good agreement with the observed spectra.

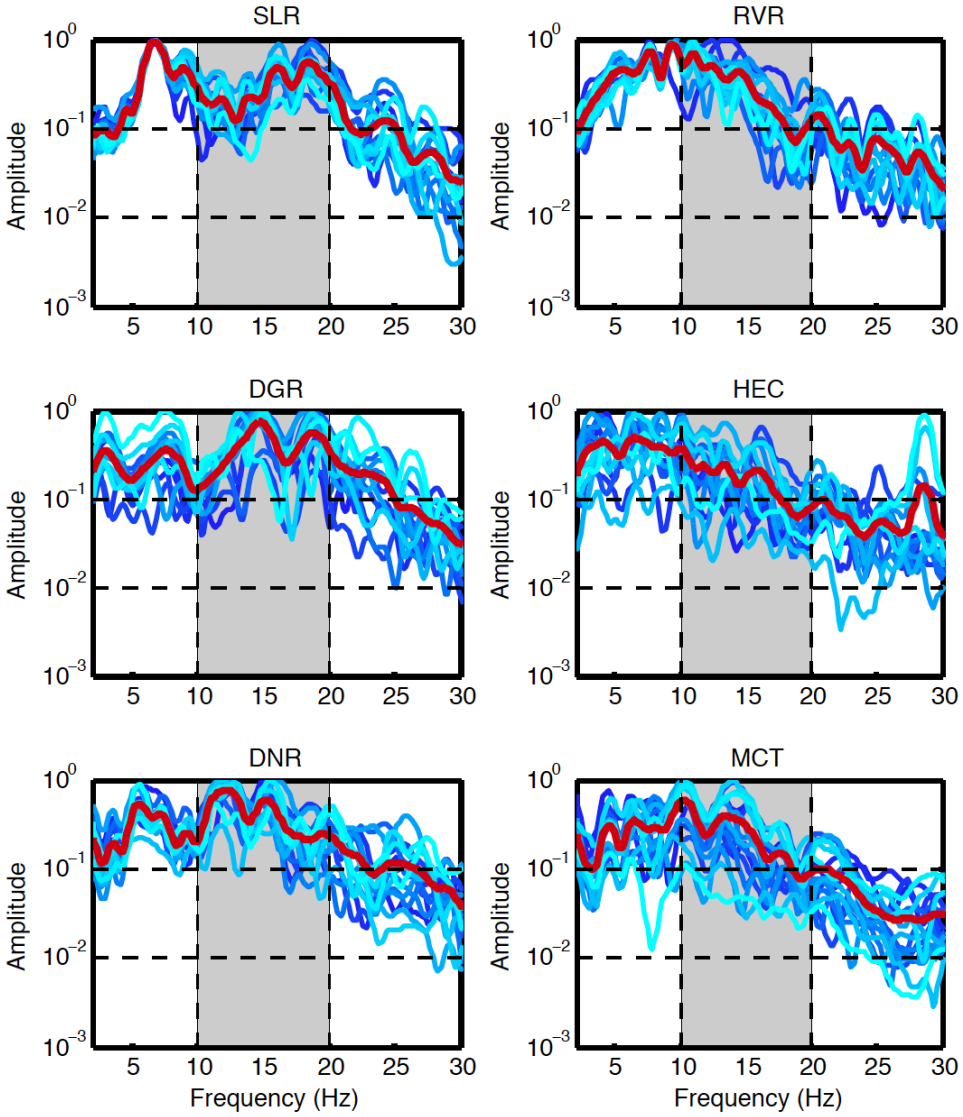

Figure 6.15: Observed velocity spectra for cluster A at stations in Zone 1 (left) and stations in Zone 2 (right). Red solid lines show the average velocity spectra. Station names are indicated above each figure.

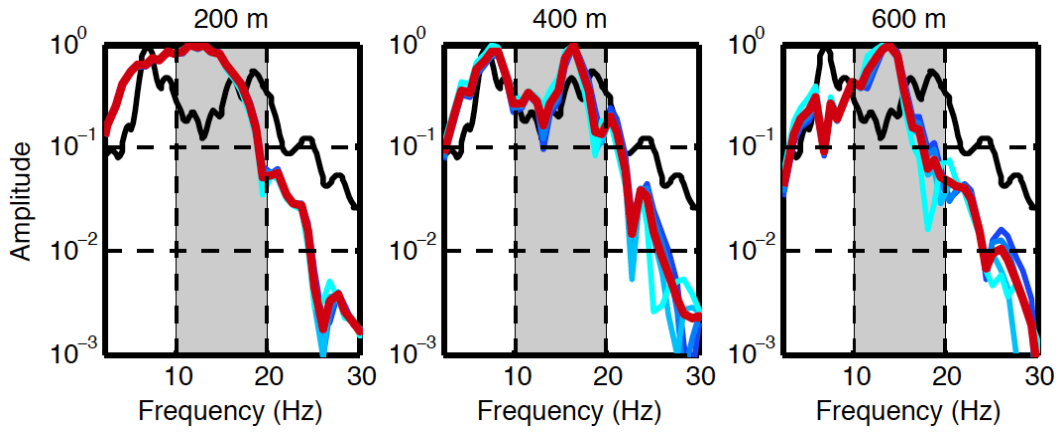

Figure 6.16: The comparison between observed and synthetic velocity spectra of P waves. Black lines show the average observed velocity spectra for cluster A at station SLR. Blue lines display synthetic velocity spectra of P waves recorded by stations every 3^o in Zone 1 for fault zones of 40% velocity reduction and widths of 200, 400 and 600 m. Red solid lines show the average synthetic velocity spectra.

6.5 Fault Zone Materials Profoundly Affect Earthquakes

Supershear earthquakes are usually associated with large shear stresses on the fault in homogeneous media, but here we show that large stresses are not needed when a damaged fault zone is present. Supershear transitions happen in fault zones even when $S > 1.77$ and a smaller S ratio favors a faster transition to supershear rupture. Our results are based on a fault zone model with sharp and planar boundaries, which may not be adequate for all natural fault zones. Abrupt changes of wave speeds are observed in the borehole data of the San Andreas fault zone [Ellsworth and Malin, 2012], and multiple reflections in high-frequency body waves from small earthquakes also demonstrate the presence of sharp boundaries in the San Jacinto, Landers and Calico fault zones [Li et al., 2007; Yang and Zhu, 2010; Yang et al., 2011]. Moreover, for a given fault zone width and fault stress condition, only earthquakes with a certain range of magnitudes can accelerate to supershear speeds if L_c or critical slip distance D_c is scaled with earthquake size. For example, earthquakes with $L_c = 400\ m$ (or $D_c = 0.4$ m when $G = 30$ GPa and $\Delta\tau_s = 30$ MPa) cannot undergo permanent supershear transition in a 400 m wide fault zone with 30% velocity reduction when $S \geq 1.5$, while earthquakes with $L_c = 200\ m$ can accelerate permanently to supershear speeds in the same fault zone when $S \leq 3.5$ (Figure 6.5). For smaller earthquakes with L_c in the order of 10 m, supershear ruptures can only occur for small S ratios when the transition lengths are shorter than the total rupture lengths.

Our results also suggest that major faults with pronounced fault zones are more prone to accommodate super-Rayleigh ruptures with unstable supershear speeds or "forbidden speeds". It is possible that the northern segment of the 1906 San Francisco earthquake involved supershear rupture with an inferred speed of ~3.9 km/s ($\sim 1.1\ v_s$) [Song et al., 2008], which is consistent with the ~ 35% velocity reduction in the San Andreas fault zone [Lewis and Ben-Zion, 2010]. As supershear ruptures can produce unusually large ground motions within the Mach cone [Bernard and Baumont], such variations of rupture speeds are important to consider for ground-motion predictions of earthquakes in well-known fault zones. The observations in Big Bear also show that fault zones can be composed of heterogeneous materials that promote super-Rayleigh ruptures in small earthquakes. In particular, events in damaged fault zones could have higher rupture speeds and larger source dimensions compared to others. This result provides a reasonable explanation for the large scatter in stress-drop measurements as influenced by their locations relative to fault zones. Material heterogeneities in fault zones, which can be studied through small earthquakes in well-instrumented areas, should be considered as another controlling factor of earthquakes besides the stress heterogeneities on the fault. The fault stresses and materials in fault zones are likely to evolve together during seismic cycles, and this certainly deserves more investigation in future studies.

Chapter 7

CONCLUSION

With the rapid development of numerical methods and computational technology, fully dynamic modeling of earthquake ruptures with large-scale complexities will become more feasible. Meanwhile, the fast-growing field of instrumentation also gives rise to a variety of high-resolution observations. The integration of dynamic rupture simulations and earthquake observations will play a crucial role in seismological studies with the following applications: (1) Observations can provide more realistic constraints on dynamic rupture simulations; (2) Dynamic rupture simulations are effective at identifying non-physical features inferred from observations, and thus help us gain more physical insights into the underlying mechanisms; (3) Dynamic rupture simulations are powerful tools to untangle the different complexities involved in the observed rupture process; (4) Dynamic rupture simulations can be used to "predict" observations, which can promote the development of next-generation models with the potential for practical applications in seismic hazard mitigation.

The thesis demonstrates examples of the above applications:

In Chapter 2, we develop an observation-based dynamic rupture simulation of the M_w 9.0 2011 Tohoku-Oki earthquake. The simulation explains the high-frequency radiations observed from the deep region by considering the asperities left from historical earthquakes. The simulation also shows that though the initial shear stress is low in the shallow region, dynamic waves reflected in the subduction wedge induce large transient stress changes, which promote up-dip rupture propagation and result in large final slip. The result implies that it would be difficult to nucleate an earthquake in the shallow region given the relatively low stress, but the final slip would be amplified once the rupture propagated through due to the dynamic effect of the subduction wedge.

In Chapter 3, we present a new way to develop dynamic rupture simulations by integrating a variety of seismic observations. We characterize the kinematic inversion results by the locations of peak slip and identify three different groups. We use three simulations to reproduce the three different slip distributions and the ratio of deep to shallow high-frequency slip-rate power derived from back projection. Despite the large variations among observations, we find that the average static stress

drop falls within the range of 4.5 MPa to 7 MPa and fracture energy in the shallow region is in the order of 10 MJ/m^2 in the simulations. Moreover, the simulations suggest that the average up-dip rupture speed should not exceed 2 km/s, or otherwise the amount of high-frequency energies radiated from the shallow region would be too large. We also calculate radiation efficiency, usually used to estimate energy partitioning of earthquakes [Kanamori and Rivera, 2006], from our dynamic rupture simulations. The calculated radiation efficiency is higher than that inferred from seismic data, implying additional energy dissipation processes. All the three simulations emphasize the important contribution of subduction wedge to the resulting large slip at shallow depth.

In Chapter 4, we elucidate the effects of damaged fault zones that usually exist around natural faults on the generation of slip pulses, a common feature of earthquake ruptures [Heaton, 1990]. We prove that fault zones with strong enough wave velocity contrasts can induce slip pulses, which are generated by reflected waves from the boundaries of the fault zone. This mechanism is robust to variations of initial stress, fault zone structure smoothness, rupture mode and exclusion of frictional healing. It differs from the other mechanisms of pulse generation in the predictability of the rise time, which is determined by the velocity contrast and width of the fault zone.

In Chapter 5, we investigate the respective contributions of different fault zone waves to rupture properties. We find that reflected waves induce multiple slip pulses and head waves cause oscillations of rupture speeds. Such effects should also exist in natural fault zones although the wavefield could be more complicated. We also consider other complexities of natural fault zones such as large attenuation and off-fault plastic deformations. We find large attenuation smears the shape of slip pulses and delays the initial acceleration of rupture speed, but it does not affect significantly the rise time and the period of rupture speed oscillations. Unlike the off-fault plastic deformations in homogeneous media, ruptures in fault zones cause plastic deformations on both extensional and compressional sides of the fault. The oscillating rupture speeds also lead to spatially periodic patterns of plastic deformations, which may leave a permanent geological signature around natural faults.

In Chapter 6, we find ruptures in damaged fault zones can propagate stably at super-Rayleigh speeds that are unstable in homogeneous media. However, such speeds are observed in several moderate and large earthquakes. Moreover, supershear ruptures in damaged fault zones do not

require large fault stresses. We use the 2003 Big Bear sequence as an example, in which the rupture speed of a M_w 3.5 earthquake is in the unstable super-Rayleigh range. We take advantage of the dense seismic network in Southern California and demonstrate that a damaged fault zone with laterally variable materials exists in the Big Bear region, which results in the variability of rupture speeds for small earthquakes.

Future studies of earthquake physics will rely more and more on the integration of a variety of tools such as seismology, geological survey and laboratory experiments. This thesis exemplifies the unique strength of integrating numerical simulations and observations. This thesis also addresses several important questions, e.g., why big earthquakes turn out to be big and why source properties of small earthquakes vary along fault zones. For megathrust earthquakes, rupture can propagate through shallow regions due to the large transient stress changes carried by dynamic waves in the subduction wedge. This effect is expected to be stronger for a subducted plate with smaller dip angle. Moreover, earthquakes in damaged fault zones could have larger rupture speeds and source dimensions, which provides a reasonable explanation for the variations of stress drop estimates for small earthquakes. Dynamic rupture simulations integrated with earthquake observations will certainly provide more insights into the mechanisms of earthquakes, with an ultimate goal of effective prevention and mitigation of seismic hazards.

A p p e n d i x A

SUPPLEMENTARY MATERIALS FOR CHAPTER 3

The amplitude spectrum of slip rate in a rupture model with process zone (Figure 3.4) can be expressed as a function of final slip D, the first corner frequency $f_{ris} = 1/t_{ris}$ and the second corner frequency $f_{pz} = 1/t_{pz}$. The amplitude spectrum is flat until the first corner frequency, and then decreases as a function of $f^{-1/2}$. After the second corner frequency, the amplitude spectrum decreases as a function of $f^{-3/2}$ in the case of linear slip-weakening friction law (Figure 5c in Kaneko et al., 2008). Thus, the amplitude spectrum can be expressed as:

$$v(f) = \begin{cases} D & if\ f < f_{ris} \\ D(\frac{f_{ris}}{f})^{1/2} & if\ f_{ris} < f < f_{pz} \\ D(\frac{f_{ris}}{f_{pz}})^{1/2}(\frac{f_{pz}}{f})^{3/2} & if\ f > f_{pz} \end{cases} \tag{A1}$$

As can be seen from Figure 3.4, the largest deep/shallow ratio of slip rate α happens when $f \geq f_{pz}$:

$$\alpha = \frac{D^d\sqrt{f_{ris}^d f_{pz}^d}}{D^s\sqrt{f_{ris}^s f_{pz}^s}} \tag{A2}$$

The formula for second corner frequency f_{pz} in Mode II is:

$$f_{pz} = \frac{(1-\upsilon)\Delta\tau_s v_R}{\mu D_c} A_{II}(v_R) \tag{A3}$$

where ν is Poisson's ratio, μ is shear modulus, $\Delta\tau_s$ is strength drop, v_R is the rupture velocity, and A_{II} is a function of v_R (Equation (5.3.11) in Freund, 1990). By combining (A2) and (A3) and assuming a uniform Poisson's ratio and shear modulus, the shallow/deep D_c ratio can be expressed as a function of α:

$$\frac{D_c^s}{D_c^d} = \alpha\frac{D^s}{D^d}\left(\frac{f_{ris}^s}{f_{ris}^d}\right)^{\frac{1}{2}}\frac{\Delta\tau_s^s v_R^s}{\Delta\tau_s^d v_R^d}\frac{A_{II}^s(v_R^s)}{A_{II}^d(v_R^d)} \tag{A4}$$

The final slip, rise time and rupture velocity can be inferred from slip inversions. The strength drop

is our model parameter. For example in our first model, as $\left(\frac{f_{ris}^{s}}{f_{ris}^{d}}\right)^{\frac{1}{2}} \sim 1$, $\frac{\Delta\tau_s^s v_R^s}{\Delta\tau_s^d v_R^d} \sim 1$, and $\frac{A_{II}^s(v_R^s)}{A_{II}^d(v_R^d)} \sim 1$, we can simplify (A4) to:

$$\frac{D_c^s}{D_c^d} \approx \alpha\left(\frac{D^s}{D^d}\right) \tag{A5}$$

As the observed high-frequency slip rate power ratio is at least 10, α has to be larger than $\sqrt{10}$. Given $\frac{D^s}{D^d} \sim 2$ to 3, the shallow/deep D_c ratio is larger than 6 to 9. Note that the needed D_c ratio (> 10) in our model is larger than this range, as the observed power ratio involves smoothing in time and space. Thus, (A4) and (A5) only give a lower bound of the shallow/deep D_c ratio.

A p p e n d i x B

SUPPLEMENTARY MATERIALS FOR CHAPTER 4

Convergence test in the configuration of SCEC TPV3

We first carry out a benchmark of SEM using the 2D analogue of the SCEC TPV3 problem [Harris et al., 2009] and compare our results to another method, the DFM results of Rojas et al. [2008]. DFM is a highly efficient parallel finite difference code [Day, 1982b; Harris and Day, 1997; Day and Ely, 2002]. Both codes handle dynamic fault conditions based on the traction-at-split-node method [Andrews, 1999]. We model an isotropic, homogeneous and elastic fault plane with density of 2670 kg m^{-3}, S wave velocity of 3464 m s^{-1} and P wave velocity of 6000 m s^{-1}. The rupture is nucleated in a middle patch of 3000 m size and propagates for a distance of 15 km. The static friction is 0.677 and dynamic friction is 0.525 in the 30 km central segment. Rupture is stopped by abrupt barriers with much higher friction coefficient.

We use five GLL nodes per spectral element side in our simulation. The equivalent grid size is the average spacing of GLL nodes, a quarter of the SEM element size. Thus, the SEM simulation with element size of 50 m (SEM50) has the same spatial resolution as the DFM reference with grid size of 12.5 m (DFM12.5). We tested the following SEM element sizes: 75, 100, 125, 150, 187.5, 250, 300, 375 and 750 m. The rupture time is defined as the first time when slip rate at a given location exceeds 1 mm/s. We calculate the RMS rupture time difference of each simulation compared to SEM50 and express the results as a percentage of the mean rupture time of SEM50. The RMS rupture time differences as well as time steps are shown as a function of average grid spacing in Figure B1a, the same representation used by Rojas et al. [2008]. The SEM results converge at approximately the same rate as the DFM results. However, the log-log plot of RMS rupture time difference as a function of grid spacing has a significant curvature for both SEM and DFM. To explain this curvature, we first observe that the rupture time in our SEM simulations converges locally (at each fault point) as a function of grid spacing. Moreover, this local convergence appears smooth and monotonic. We hence postulate that the rupture time $t(i,h)$ at position i is asymptotically related to the exact rupture time $t(i,0)$ by:

$$t(i,h) \approx t(i,0) + c(i)h^{p} \tag{B1}$$

where h is the average grid spacing, $c(i)$ is a problem-dependent constant and p is the leading-order exponent. This implies that the RMS rupture time difference of the j^{th} simulation relative to the k^{th} simulation is:

$$e_{jk} = q(h_j^p - h_k^p) \tag{B2}$$

where $q = \sqrt{\dfrac{\sum_{i=1}^{n}(c(i))^2}{n}}$.

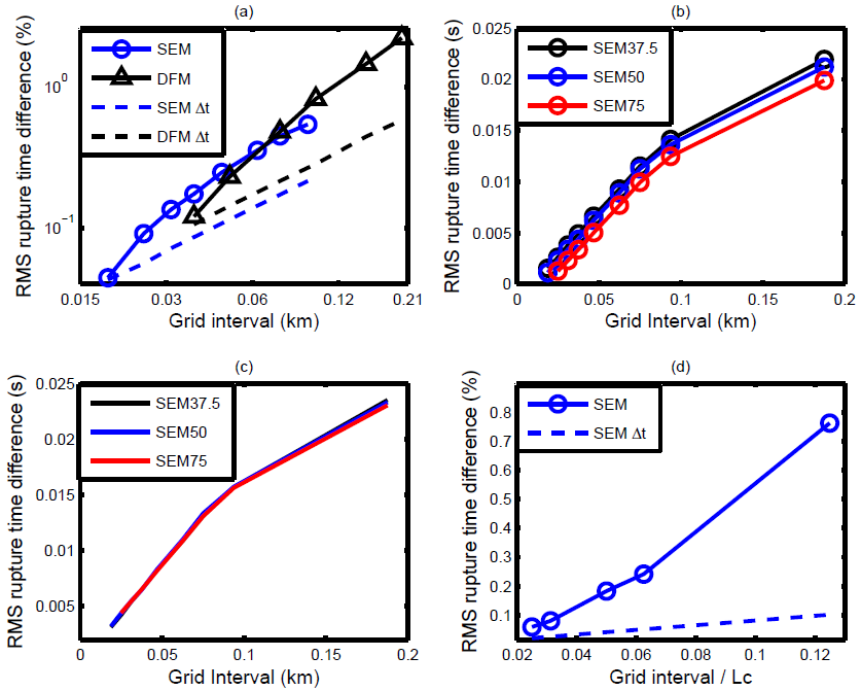

Figure B1: (a) RMS of rupture time difference relative to the finest resolution simulation in the SCEC TPV3 problem as a function of grid interval for SEM and DFM (log-log scale). (b) Same but relative to SEM37.5, SEM50 and SEM75 (linear scale). (c) Same as (b) after correcting for the effect of the reference simulation. (d) RMS rupture time difference relative to SEM0.0625 as a function of grid interval for SEM simulations in the LVFZ model setup.

Figure B1b shows, as a function of grid spacing, the RMS rupture time difference of each simulation relative to three different reference simulations, SEM37.5, SEM50 and SEM75. The relative errors (with the exception of the coarser one, SEM750) follow a linear trend of the form of Equation (B2) with p=1. A least squares regression indicates that q = 0.168, independent of the

choice of reference simulation. Figure B1c shows the rupture time errors corrected for the influence of the reference simulation (qh_k) as a function of grid spacing.

Comparison of results of LVFZ simulations to DFM

We ran a simulation of rupture in an LVFZ with SEM and DFM based on the same input parameters and compare the results as follows.

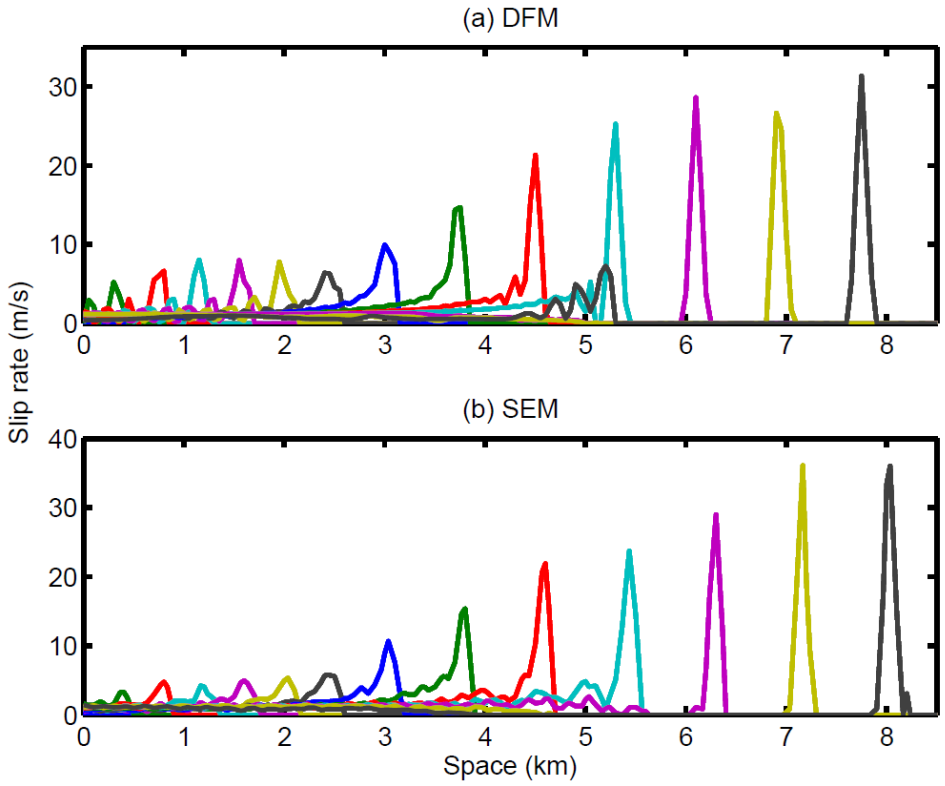

Figure B2: Spatial distributions of slip rate every 0.46 s for rupture inside an 800 m wide LVFZ with velocity reduction of 40% computed with (a) DFM and (b) SEM.

We choose 50 m grid size in DFM and 200 m element size in SEM. The LVFZ that bisects the fault plane has a width of 800 m and velocity reduction of 40% for both P and S waves. Specifically, the S wave speed of LVFZ is 2078.4 m s^{-1} and its P wave speed is 3600 m s^{-1}. The friction law and coefficients are the same as described in Section 2 of the main text. The rupture propagates for 6.5 seconds total, during which the multiple reflected waves from the interface of LVFZ and country rock continuously alter the shear stress on the fault plane, resulting in slip rate oscillations and arrest

episodes. Figures B2a and B2b show the spatial distribution of slip rate in time interval of 0.46 s for both simulations.

Slip pulses are generated in both SEM and DFM simulations. The rise times are short compared to the total rupture time. The slip rates at different times in both simulations are comparable except inside the nucleation zone. The ruptures propagate at a relatively constant speed of about 1900 m s^{-1} after 4 seconds, which is the Rayleigh wave speed of the LVFZ. Overall, the two codes produce very similar patterns of slip functions and rupture processes.

However, owing to the inherent differences between equivalent SEM and DFM simulations, we still see some minor differences, such as more high-frequency oscillations and a slightly higher maximum slip rate in SEM. Since the GLL nodes are not evenly distributed, the required time step in SEM is always smaller than DFM given the same equivalent grid size. Because the artificial viscosity on the fault plane is normalized by the actual time step in both codes, the SEM simulations are always less damped than their corresponding DFM simulation.

Convergence test of the dimensionless LVFZ problem

We show here that the simulations conserve numerical convergence in our LVFZ model setup using dimensionless quantities. We consider an LVFZ with $W = 2$ and $\Delta v = 0.4$. The onset of spontaneous rupture occurs around $t = 14$ and the simulation runs until $t = 45$. It is expected that as the ratio of element size to W decreases the rupture process should be better resolved. In our simulation of finest resolution, SEM0.0625, the rupture behaves as a single pulse. Its healing phase is clean, the slip rate has weak high-frequency oscillations and its peak amplitude grows gradually with time. Coarse simulations like SEM0.25 have instead a crack following the pulse. Figure B1d shows the RMS of the rupture time difference with respect to SEM0.0625, as a function of average grid size, including time steps for comparison. The simulations with finer resolution than SEM0.5 converge linearly, as found previously in our convergence tests in homogeneous medium.

Appendix C

SUPPLEMENTARY MATERIALS FOR CHAPTER 5

To show that the simulations are convergent, we carry out the convergence test for different element sizes. There are five GLL nodes in each spectral element, so the average grid interval is a quarter of the element size. The test simulations have the same frictional parameters and fault zone velocity contrasts, except that the element size varies. We show in Figure C1 the RMS of rupture time difference relative to the finest simulation with element size of 0.0625 L_c for both 2 L_c and 4 L_c wide fault zones. We find that the wider the fault zone is, the larger the RMS error is. But the 4 L_c simulations converge faster, and the RMS error for element size of 0.1 L_c is negligible for both 2 L_c and 4 L_c cases.

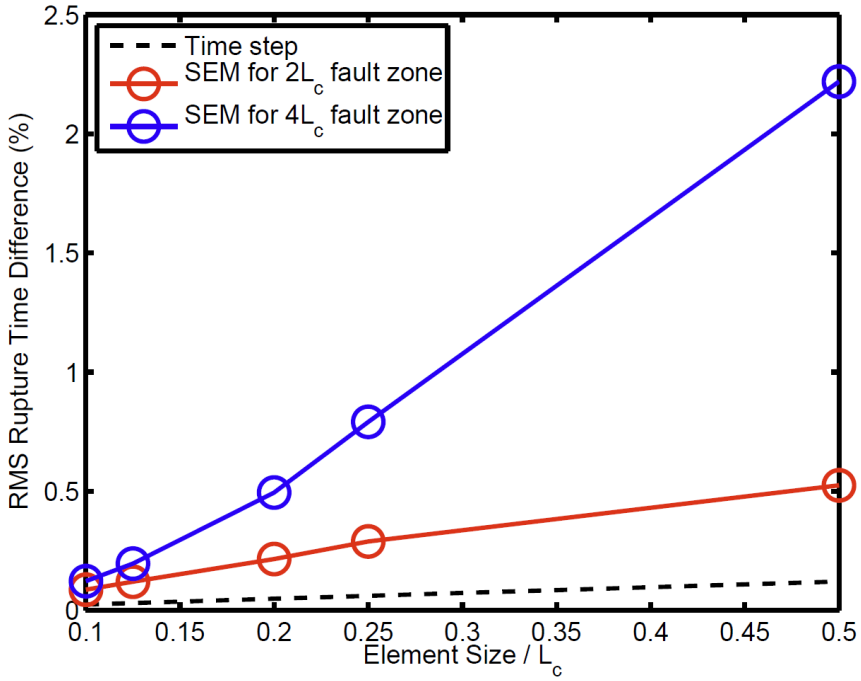

Figure C1: RMS rupture time difference relative to the finest simulation with element size of 0.0625 L_c for both 2 L_c and 4 L_c wide fault zones.

BIBLIOGRAPHY

Aagaard, B. T., and T. H. Heaton (2008), Constraining fault constitutive behavior with slip and stress heterogeneity, *J. Geophys. Res., 113*, B04301, doi:10.1029/2006JB004793.

Aki, K., and P. G. Richards (2002), *Quantitative Seismology*, University Science Books, Sausalito, Calif.

Ampuero, J. P., (2009), SEM2DPACK, A Spectral Element Method tool for 2D wave propagation and earthquake source dynamics, User's Guide, version 2.3.6, Available online at http://www.sourceforge.net/projects/sem2d/.

Ampuero, J. P., and Y. Ben Zion (2008), Cracks, pulses and macroscopic asymmetry of dynamic rupture on a bimaterial interface with velocity weakening friction, *Geophys. J. Int., 173*(2), 674-692, doi:10.1111/j.1365-246X.2008.03736.x.

Ampuero, J. P., J. P. Vilotte, and F. Sanchez-Sesma (2002), Nucleation of rupture under slip dependent friction law: Simple models of fault zone, *J. Geophys. Res., 107*(B12), 2324, doi:10.1029/2001JB000452.

Andrews, D. J. (1976), Rupture velocity of plane strain shear cracks, *J. Geophys. Res., 81*(32), 5679-5687.

Andrews, D. J. (1985), Dynamic plane-strain shear rupture with a slip-weakening friction law calculated by a boundary integral method, *Bull. Seismol. Soc. Am., 75*(1), 1-21.

Andrews, D. J. (1999), Test of two methods for faulting in finite-difference calculations, *Bull. Seismol. Soc. Am., 89*(4), 931-937.

Andrews, D. J., and Y. Ben-Zion (1997), Wrinkle-like slip pulse on a fault between different materials, *J. Geophys. Res., 102*(B1), 553-571.

Antolik, M., R. E. Abercrombie, and G. Ekström (2004), The 14 November 2001 Kokoxili (Kunlunshan), Tibet, Earthquake: Rupture transfer through a large extensional step-over, *Bull. Seismol. Soc. Am., 94*, 1173-1194.

Aochi, H., and S. Ide (2011), Conceptual multi-scale dynamic rupture model for the 2011 off the Pacific coast of Tohoku Earthquake, *Earth Planets Space, 63*, 761-765.

Archuleta, R. J. (1984), A faulting model for the 1979 Imperial Valley earthquake, *J. Geophys. Res.*, *89*, 4559-4585.

Asano, K., T. Iwata, K. Irikura (2005), Estimation of source rupture process and strong ground motion simulation of the 2002 Denali, Alaska, earthquake, *Bull. Seismol. Soc. Am., 95*, 1701-1715.

Beeler, N., and T. Tullis (1996), Self-healing slip pulses in dynamic rupture models due to velocity-dependent strength, *Bull. Seismol. Soc. Am., 86*(4), 1130-1148.

Ben-Zion, Y. (1998), Properties of seismic fault zone waves and their utility for imaging low-velocity structures, *J. Geophys. Res., 103*(B6), 12567-12585, doi:10.1029/98JB00768.

Ben-Zion, Y. (2002), Properties of seismic fault zone waves and their utility for imaging low-velocity structures, *J. Geophys. Res., 103*, 12567-12585.

Ben-Zion, Y. and Y. Huang (2002), Dynamic rupture on an interface between a compliant fault zone layer and a stiffer surrounding solid, *J. Geophys. Res., 107*(B2), 2042, doi:10.1029/2001JB000254.

Ben-Zion, Y. and C. G. Sammis (2003), Characterization of fault zones, *Pure Appl. Geophys., 160*(3-4), 677-715.

Ben-Zion, Y. and J. -P. Ampuero (2009), Seismic radiation from regions sustaining material damage, *Geophys. J. Int., 178*(3), 1351-1356, doi:10.1111/j.1365-246X.2009.04285.x.

Ben-Zion, Y., Z. Peng, D. Okaya, L. Seeber, J. G. Armbruster, N. Ozer, A. J. Michael, S. Baris and M. Aktar (2003), A shallow fault-zone structure illuminated by trapped waves in the Karadere-Duzce branch of the North Anatolian Fault, western Turkey, *Geophys. J. Int., 152*(3), 699-717, doi:10.1111/j.1365-246X.2003.01870.x.
Ben-Zion, Y., T. Rockwell, Z. Shi, and S. Xu (2012), Reversed-polarity secondary deformation structures near fault stepovers, *J. of Appl. Mech., 79*, 031025, doi:10.1115/1.4006154.
Bernard, P., and D. Baumont (2005), Shear Mach wave characterization for kinematic fault rupture models with constant supershear rupture velocity, *Geophys. J. Int., 162*, 431-447.
Beroza, G. C., and T. Mikumo (1996), Short slip duration in dynamic rupture in the presence of heterogeneous fault properties, *J. Geophys. Res., 101*(B10), 22449-22460.
Beroza, G. C., and P. Spudich (1988), Linearized inversion for fault rupture behavior: application to the 1984 Morgan Hill, California, earthquake, *J. Geophys. Res., 93*(B6), 6275-6296.
Biegel, R. L., C. G. Sammis, and A. J. Rosakis (2008), An experimental study of the effect of off-fault damage on the velocity of a slip pulse, *J. Geophys. Res., 113*, B04302, doi:10.1029/2007JB005234.
Birgören, G., H. Sekiguchi, and K. Ikikura (2004), Rupture model of the 1999 Düzce, Turkey, earthquake deducted from high and low frequency strong motion data, *Geophys. Res. Lett., 31*, L05610.
Bouchon, M., and M. Vallee (2003), Observation of long supershear rupture during the magnitude 8.1 Kunlunshan earthquake, *Science, 301*, 824-826, doi:10.1126/science.1086832.
Bouchon, M., H. Karabulut, M.-P. Bouin, J. Schmittbuhl, M. Vallee, R. Archuleta, S. Das, F. Renard, and D. Marsan (2010), Faulting characteristics of supershear earthquakes, *Tectonophysics., 493*(3-4), 244-253, doi:10.1016/j.tecto.2010.06.011.
Bouchon, M., M.-P. Bouin, H. Karabulut, M. N. Toksoz, M. Dietrich, and A. J. Rosakis (2001), How fast is rupture during an earthquake? New insights from the 1999 Turkey earthquakes, *Geophys. Res. Lett., 28*, 2723-2726, doi:10.1029/2001GL013112.
Bouchon, M., M. N. Toksoz, H. Karabulut, M.-P. Bouin, M. Dietrich, M. Aktar, and M. Edie (2002), Space and time evolution of rupture and faulting during the 1999 Izmit (Turkey) earthquake, *Bull. Seismol. Soc. Am., 92*(1), 256-266, doi:10.1785/0120000845.
Bouin, M.-P., M. Bounchon, H. Karabulut, and M. Aktar (2004), Rupture process of the 1999 November 12 Düzce (Turkey) earthquake deducted from strong motion and global positioning system measurements, *Geophys. Res. Lett., 156*, 207-211.
Boullier, A. M., T. Ohtani, K. Fujimoto, H. Ito, and M. Dubois (2001), Fluid inclusions in pseudotachylytes from the Nojima fault, Japan, *J. Geophys. Res., 106*(B10), 21965-21977.
Brietzke, G. B. and Y. Ben-Zion (2006), Examing tendencies of in-plane rupture to migrate to material interfaces, *Geophys. J. Int., 167*(2), 807-819, doi:10.1111/j.1365-246X.2006.03137.x.
Broberg, K. B. (1999), *Cracks and fracture*, Academic, San Diego, Calif.
Burridge, R., G. Conn, and L. B. Freund (1979), The stability of a rapid mode II shear crack with finite cohesive traction. *J. Geophys. Res., 85*, 2210-2222.
Candela, T., F. Renard, M. Bouchon, J. Schmittbuhl, E. E. Brodsky (2011), Stress drop during earthquakes: Effects of fault roughness scaling, *Bull. Seismol. Soc. Am., 101*(5), 2369-2387, doi: 10.1785/0120100298.
Carcione, J. M., D. Kosloff, and R. Kosloff (1988), Wave propagation simulation in a linear viscoelastic medium, *Geophys. J., 95,* 597-611.
Casey, M. (1980), Mechanics of shear zones in isotropic dilatant materials, *J. Struct. Geol., 2* (1/2), 143-147.
Chen, K. H., B. L. N. Kennett, and T. Furumura (2013), High-frequency waves guided by the subducted plates underneath Taiwan and their association with seismic intensity anomalies, *J. Geophys. Res. Solid Earth, 118*, 665–680, doi:10.1002/jgrb.50071.

Chester, F. M., and J. M. Logan (1986), Implications for mechanical properties of brittle faults from observations of the Punchbowl fault zone, California, *Pure App. Geophys., 124*(1-2), 79-106, doi: 10.1007/BF00875720.
Chester, F. M., and J. S. Chester (1998), Ultracataclasite structure and friction processes of the Punchbowl fault, San Andreas system, California, *Tectonophysics, 295*(1-2), 199-221.
Chester, F. M., and J. S. Chester (2000), Stress and deformation along wavy frictional faults, *J. Geophys. Res., 105*(B10), 23,421-23,430, doi:10.1029/2000JB900241.
Chi, W.-C., and E. Hauksson (2006), Fault-perpendicular aftershock clusters following the 2003 M_w =5.0 Big Bear, California, Earthquake, *Geophys. Res. Lett., 33*, L07301, doi: 10.1029/2009gl039494.
Childs, C., T. Manzocchi, J. J. Walsh, C. G. Bonson, A. Nicol, and M. P. J. Schopfer (2009), A geometric model of fault zone and fault rock thickness variations, *J. Struct. Geol., 31*(2), 117-127, doi:10.1016/j.jsg.2008.08.009.
Chu, R., L. Zhu, and D. V. Helmberger (2009), Determination of earthquake focal depths and source time functions in central Asia using teleseismic P waveforms, *Geophys. Res. Lett., 36,* L17317, doi: 10.1029/2009gl039494.
Cochard, A., and R. Madariaga (1996), Complexity of seismicity due to highly rate-dependent friction, *J. Geophys. Res., 101*(B11), 25321-25336.
Cochard, A., and J. R. Rice (2000), Fault rupture between dissimilar materials: Ill-posedness, regularization, and slip-pulse response, *J. Geophys. Res., 105*(25), 891-907.
Cochran, E. S., Y. G. Li, P. M. Shearer, S. Barbot, Y. Fialko, and J. E. Vidale (2009), Seismic and geodetic evidence for extensive, long-lived fault damage zones, *Geology, 37*(4), 315-318, doi:10.1130/G25306A.1.
Cormier, V. and P. Spudich (1984), Amplification of ground motion and waveform complexity in fault zones: examples from the San Andreas and Calaveras fault zones, *Geophys. J. R. Astron. Soc., 79*, 135-152.
Cowie, P. A., and C. H. Scholz (1992), Physical explanation for the displacement length relationship of faults using a post-yield fracture mechanics model, *J. Struct. Geol., 14*(10), 1133-1148, doi:10.1016/0191-8141(92)90065-5.
Das, S. (2010), Earthquake supershear rupture speeds, *Tectonophysics, 493*(3), 213-215, doi: 10.1016/j.tecto.2010.07.009.
Das, S., and K. Aki (1977), A numerical study of two-dimensional spontaneous rupture propagation, *Geophys. J. R. astr. Soc., 50*(3), 643-668.
Day, S. M. (1982a), Three-dimensional finite difference simulation of fault dynamics: Rectangular faults with fixed rupture velocity, *Bull. Seismol. Soc. Am., 72*(3), 705-727.
Day, S. M. (1982b). Three-dimensional simulation of spontaneous rupture: The effect of nonuniform prestress, *Bull. Seism. Soc. Am., 72*(6), 1881-1902.
Day, S. M. and G. P. Ely (2002), Effect of a shallow weak zone on fault rupture: Numerical simulation of scale-model experiments, *Bull. Seismol. Soc. Am., 92*(8), 3022-3041, doi:10.1785/0120010273.
Dieterich, J. H. (1978), Time-dependent friction and the mechanics of stick slip, *Pure Appl. Geophys.*, *116*, 790-806.
Dieterich, J. H. (1979), Modeling of rock friction 1. Experimental results and constitutive equations, *J. Geophys. Res.*, *84*, 2161-2168.
Di Toro, G., S. Nielsen, G. Pennacchioni (2005), Earthquake rupture dynamics frozen in exhumed ancient fault, *Nature, 436*, 1009-1012, doi: 10.1038/nature03910.
Di Toro, G., R. Han, T. Hirose, N. De Paola, S. Nielsen, K. Mizoguchi, F. Ferri, M. Cocco, and T. Shimamoto (2011), Fault lubrication during earthquakes, *Nature, 471*, 494-499, doi:10.1038/nature09838.

Dor, O., T. K. Rockwell, and Y. Ben-Zion (2006), Geological observations of damage asymmetry in the structure of the San Jacinto, San Andreas and Punchbowl faults in southern California: A possible indicator for preferred rupture propagation direction, *Pure Appl. Geophys*., *163*, 301-349, doi:10.1007/s00024-005-0023-9.
Duan, B. (2008), Effects of low-velocity fault zones on dynamic ruptures with nonelastic off-fault response, *Geophys. Res. Lett.,35,* L04307, doi:10.1029/2008GL033171.
Duan, B. (2012), Dynamic rupture of the 2011 Mw 9.0 Tohoku-Oki earthquake: Roles of a possible subducting seamount, *J. Geophys. Res.*, *117*, B05311.
Dunham, E. M. (2007), Conditions governing the occurrence of supershear ruptures under slip-weakening friction, *J. Geophys. Res., 112*, B07302, doi:10.1029/2006JB004717.
Dunham, E. M., and R. J. Archuleta (2004), Evidence for a supershear transient during the 2002 Denali Fault earthquake, *Bull. Seismol. Soc. Am., 94*(6B), S256-S268, doi:10.1785/0120040616.
Dunham, E. M., D. Belanger, L. Cong, and J. E. Kozdon (2011a), Earthquake ruptures with strongly rate-weakening friction and off-fault plasticity, Part 1: Planar faults, *Bull. Seismol. Soc. Am., 101* (5), 2296-2307.
Dunham, E. M., D. Belanger, L. Cong, and J. E. Kozdon (2011b), Earthquake ruptures with strongly rate-weakening friction and off-fault plasticity, Part 2: Nonplanar faults, *Bull. Seismol. Soc. Am., 101* (5), 2308-2322.
Ellsworth, W. L., and P. E. Malin (2011), Deep rock damage in the San Andreas Fault revealed by P- and S-type fault-zone-guided waves, *Geological Society, London, Special Publications 2011, 359*, 39-53, doi:10.1144/SP359.3.
Ellsworth, W. L., M. Celebi, J. R. Evans, E. G. Jensen, R. Kayen, M. C. Metz, D. J. Nyman, J. W. Roddick, P. Spudich, C. D. Stephens (2004), Near-field ground motion of the 2002 Denali Fault, Alaska, earthquake recorded at Pump Station 10, *Earthq. Spectra, 20*(3), 597-615, doi:10.1193/1.1778172.
Faulkner, D. R., T. M. Mitchell, D. Healy, and M. J. Heap (2006), Slip on 'weak' faults by the rotation of regional stress in the fracture damage zone, *Nature, 444,* 922-925, doi:10.1038/nature05353.
Faulkner, D. R., T. M. Mitchell, E. Jensen, and J. Cembrano (2011), Scaling of fault damage zones with displacement and the implications for fault growth processes, *J. Geophys. Res*., *116,* B05403, doi:10.1029/2010JB007788.
Field, F. A., and B. R. Baker (1962), Crack propagation under shear displacements, *J. Appl. Mech*., 436-437.
Freund, L. B. (1990), *Dynamic Fracture Mechanics*, Cambridge Univ. Press, Cambridge.
Fujiwara, T., S. Kodaira, T. No, Y. Kaiho, N. Takahashi, and Y. Kaneda (2011), The 2011 Tohoku-Oki earthquake: Displacement reaching the trench axis, *Science, 334*, 1240.
Furumura T., and B. L. N. Kennett (2008), A Scattering Waveguide in the Heterogeneous Subducting Plate, *Adv. Geophys., 50*(7), 195-217, doi: 10.1016/S0065-2687(08)00007-1.
Galvez, P., J.-P. Ampuero, L. A. Dalguer, and T. Nissen-Meyer (2011), Dynamic rupture modeling of the 2011 M9 Tohoku earthquake with an unstructured 3D spectral element method, *AGU Fall Meet. Suppl., Abstract* U51B-0043.
Goto, H., and S. Sawada (2010), Trade-offs among dynamic parameters inferred from results of dynamic source inversion, *Bull. Seismol. Soc. Am., 100*(3), 910-922, doi:10.1785/0120080250.
Goto, H., Y. Yamamoto, and S. Kita (2012), Dynamic rupture simulation of the 2011 off the Pacific coast of Tohoku Earthquake: Multi-event generation within dozens of seconds, *Earth Planets Space, 64*, 1167-1175.

Harris, R. A., and S. M. Day (1993), Dynamics of fault interaction: parallel strike-slip faults, *J. Geophys. Res., 98*, 4461-4472.
Harris, R. A., and S. M. Day (1997), Effects of a low-velocity zone on a dynamic rupture, *Bull. Seismol. Soc. Am., 87*(5), 1267-1280.
Harris, R. A., M. Barall, R. Archuleta, E. Dunham, B. Aagaard, J. Ampuero, H. Bhat, V. Cruz-Atienza, L. Dalguer, and P. Dawson (2009), The SCEC/USGS dynamic earthquake rupture code verification exercise, *Seismol. Res. Lett., 80*(1), 119-126, doi:10.1785/gssrl.80.1.119.
Hartzell, S. H., and T. H. Heaton (1986), Rupture history of the 1984 Morgan Hill, California, earthquake from the inversion of strong motion records, *Bull. Seismol. Soc. Am., 76*(3), 649-674.
Hauksson, E., W. Yang, and P. M. Shearer (2012), Waveform relocated earthquake catalog for Sourthern California (1981 to 2011) , *Bull. Seismol. Soc. Am., 102*(5), 2239-2244.
Heaton, T. H. (1990), Evidence for and implications of self-healing pulses of slip in earthquake rupture, *Phys. Earth Planet. Inter., 64*(1), 1-20.
Hickman, S. H., M. D. Zoback, and W. L. Ellsworth (2005). Structure and Composition of the San Andreas fault zone at Parkfield: initial results from SAFOD phase 1 and 2, *EOS Trans. AGU 83*(47), 237.
Huang, Y., and J.-P. Ampuero (2011), Pulse-like ruptures induced by low-velocity fault zones, *J. Geophys. Res., 116*, B12307, doi:10.1029/2011JB008684.
Huang, Y., L. Meng, and J.-P. Ampuero (2012), A dynamic model of the frequency-dependent rupture process of the 2011 Tohoku-Oki earthquake, *Earth Planets Space, 64*, 1061-1066.
Huang, Y., J.-P. Ampuero, and H. Kanamori (2013), Slip-weakening models of the 2011 Tohoku-Oki earthquake and constraints on stress drop and fracture energy, *Pure Appl. Geophys.,* doi:10.1007/s00024-013-0718-2.
Huang, Y., D. V. Helmberger, and J.-P. Helmberger (2013), Rupture propagating at the forbidden speed: Is fault zone structure playing a role?, Abstract T53D-2608 presented at 2013 Fall Meeting, AGU, San Francisco, Calif., 9-13 Dec.
Huang, Y., J.-P. Ampuero, and D. V. Helmberger (2014), Earthquake ruptures modulated by waves in damaged fault zones. *J. Geophys. Res.,* doi:10.1002/2013JB010724.
Huber, P. J. (1973), Robust regression: asymptotics, conjectures and Monte Carlo, *Ann. Statist., 1*, 799-821.
Hyndman, R. D., M. Yamano, and D.A. Oleskevich (1997), The seismogenic zone of subduction thrust faults, *Island Arc, 6*, 244-260.
Ida, Y. (1972), Cohesive force across the tip of a longitudinal-shear crack and Grffith's specific surface energy, *J. Geophys. Res., 77*(20), 3796-3805.
Ide, S. (2007), Dynamic rupture propagation modeling, *Scientific Drilling, Special Issue No. 1*, doi:10.2204/iodp.sd.s01.05.2007.
Ide, S., A. Baltay, and G.C. Beroza (2011), Shallow dynamic overshoot and energetic deep rupture in the 2011 Mw 9.0 Tohoku-Oki earthquake*, Science, 332*, 1426-1429.
Igarashi, T., T. Matsuzawa, and A. Hasegawa (2003), Repeating earthquakes and interplate aseismic slip in the northeastern Japan subduction zone*, J. Geophys. Res., 108*, 2249.
Iinuma, T., R. Hino, M. Kido, D. Inazu, Y. Osada, Y. Ito, M. Ohzono, H. Tsushima, S. Suzuki, H. Fujimoto, and S. Miura (2012), Coseismic slip distribution of the 2011 off the Pacific Coast of Tohoku Earthquake (M9.0) refined by means of seafloor geodetic data, *J. Geophys. Res., 117*, B07409.
Ishii, M., P. M. Shearer, H. Houston, J. E. Vidale (2005), Extent, duration and speed of the 2004 Sumatra-Andaman earthquake imaged by the Hi-Net array, *Nature, 435*, 933-936.
Ito, Y., T. Tsuji, Y. Osada, M. Kido, D. Inazu, Y. Hayashi, H. Tsushima, R. Hino, and H. Fujimoto (2011), Frontal wedge deformation near the source region of the 2011 Tohoku-Oki earthquake, *Geophys. Res. Lett., 38*, L00G05.

Jahnke, G., H. Igel, and Y. Ben-Zion (2002), Three-dimensional calculations of fault-zone-guided waves in various irregular structures, *Geophys. J. Int., 151*, 416-426.
Ji, C., D. J. Wald, and D. V. Helmberger (2002), Source description of the 1999 Hector Mine, California, earthquake, part II: Complexity of slip history, *Bull. Seismol. Soc. Am., 92*(4), 1208-1226.
Ji, C., D. V. Helmberger, D. J. Wald, and K. F. Ma (2003), Slip history and dynamic implications of the 1999 Chi-Chi, Taiwan, earthquake, *J. Geophys. Res., 108*(B9), 2412, doi:10.1029/2002JB001764.
Johri, M, E. M. Dunham, M. D. Zoback, and Z. Fang (2014), Prediction fault damage zone by modeling dynamic rupture propagation and comparison with field observations, *J. Geophys.Res.*, doi:10.1002/2013JB010335.
Kame, N., J. R. Rice, and R. Dmowska (2003), Effects of pre-stress state and rupture velocity on dynamic fault branching, *J. Geophys. Res., 108*(B5), 2265, doi:10.1029/2002JB002189.
Kanamori, H., and T. H. Heaton (2000), Microscopic and macroscopic physics of earthquakes, in Geocomplexity and the Physics of Earthquakes, *Geophys. Monogr., 120*, 147-163.
Kanamori, H., and L. Rivera (2006), Energy partitioning during an earthquake, *Geophys. Monogr., 170*, 3-13, doi:10.1029/170GM03.
Kanamori, H. and K. Yomogida (2011), Preface. First Results of the 2011 Off the Pacific Coast of Tohoku Earthquake, *Earth Planets Space, 63*(7), 511, doi: 10.5047/eps.2011.07.019.
Kaneko, Y. and N. Lapusta (2010), Supershear transition due to a free surface in 3-D simulations of spontaneous dynamic rupture on vertical strike-slip faults, *Tectonophysics*, *493*, 272-284.
Kaneko, Y., N. Lapusta, and J.-P. Ampuero (2008), Spectral-element modeling of spontaneous earthquake rupture on rate and state faults: Effect of velocity-strengthening friction at shallow depths, *J. Geophys.Res., 113* (B9), B09317, doi:10.1029/2007JB005553.
Kaneko, Y., J. P. Ampuero and N. Lapusta (2011), Spectral-element simulations of long-term fault slip: Effects of low-rigidity layers on earthquake-cycle dynamics, *J. Geophys. Res*., doi:10.1029/2011JB008395, in press.
Kano, Y., J. Mori, R. Fujio, H. Ito, T. Yanagidani, S. Nakao, and K. F. Ma (2006), Heat signature on the Chelungpu fault associated with the 1999 Chi-Chi, Taiwan earthquake, *Geophys. Res. Lett., 33*, L14306, doi:10.1029/2006GL026733.
Kato, N., and S. Yoshida (2011), A shallow strong patch model for the 2011 great Tohoku-oki earthquake: A numerical simulation, *Geophys. Res. Lett., 38*, L00G04,
Kido, M., Y. Osada, H. Fujimoto, R. Hino, and Y. Ito (2011), Trench-normal variation in observed seafloor displacements associated with the 2011 Tohoku-Oki earthquake, *Geophys. Res. Lett., 38*, L24303.
Kimura, G., S. Hina, Y. Hamada, J. Kameda, T. Tsuji, M. Kinoshita, and A. Yamaguchi (2012), Runaway slip to the trench due to rupture of highly pressurized megathrust beneath the middle trench slope: The tsunamigenesis of the 2011 Tohoku earthquake off the east coast of northern Japan, *Earth Planet. Sci. Lett., 339-340*, 32-45.
Kiser, E., and M. Ishii (2012), The March 11, 2011 Tohoku-oki earthquake and cascading failure of the plate interface, *Geophys. Res. Lett., 39*, L00G25.
Kodaira, S., T. No, Y. Nakamura, T. Fujiwara, Y. Kaiho, S. Miura, N. Takahashi, Y. Kaneda, and A. Taira (2012), Coseismic fault rupture at the trench axis during the 2011 Tohoku-oki earthquake, *Nature Geosci., 5*, 646-650.
Koketsu, K., Y. Yokota, N. Nishimura, Y. Yagi, S. Miyazaki, K. Satake, Y. Fujii, H. Miyake, S. Sakai, Y. Yamanaka, and T. Okada (2011), A unified source model for the 2011 Tohoku earthquake, *Earth Planet. Sci. Lett., 310*, 480-487.

Komatitsch, D., and J. Tromp (1999), Introduction to the spectral element method for three-dimensional seismic wave propagation, *Geophys. J. Int., 139*(3), 806-822, doi: 10.1046/j.1365-246X.1999.00967.x.
Konca, A. O., S. Lepreine, J.-P. Avouac, and D. V. Helmberger (2010), Rupture process of the 1999 M_w 7.1 Duzce earthquake from joint analysis of SPOT, GPS, INSAR, Strong-motion, and teleseismic data: A supershear rupture with variable rupture velocity, *Bull. Seismol. Soc. Am., 100*, 267-288.
Kozdon, J. E., and E. M. Dunham (2013), Rupture to the trench: Dynamic rupture simulations of the 11 March 2011 Tohoku earthquake, *Bull. Seismic. Soc. Am., 103*, 1275-1289.
Lay, T., C. J. Ammon, H. Kanamori, L. Xue, and M. J. Kim (2011), Possible large near-trench slip during the 2011 Mw 9.0 off the Pacific coast of Tohoku earthquake, *Earth, Planets Space, 63*, 687-692.
Lay, T., H. Kanamori, C. J. Ammon, K.D. Koper, A. R. Hutko, L. Ye, H. Yue and T. M. Rushing (2012), Depth-varying rupture properties of subduction zone megathrust faults, *J. Geophys. Res., 117*, B04311.
Lee, S.-J., B.-S. Huang, M. Ando, H.-C. Chiu, and J.-H. Wang (2011), Evidence of large scale repeating slip during the 2011 Tohoku-Oki earthquake, *Geophys., Res. Lett., 38*, L19306.
Lewis, M. A. and Y. Ben-Zion (2010), Diversity of fault zone damage and trapping structures in the Parkfield section of the San Andreas Fault from comprehensive analysis of near fault seismograms, *Geophys. J. Int., 183*(3), *1579-1595,* doi:10.1111/j.1365-246X.2010.04816.x.
Lewis, M. A., Z. Peng, Y. Ben-Zion and F. L. Vernon (2005), Shallow seismic trapping structure in the San Jacinto fault zone near Anza, California, *Geophys. J. Int., 162*(3), *867-881,* doi:10.1111/j.1365-246X.2005.02684.x.
Li, H., L. Zhu, and H. Yang (2007), High resolution structures of the Landers fault zone inferred from aftershock waveform data, *Geophys. J. Int., 171*(3), 1295-1307, doi:10.1111/j.1365-246X.2007.03608.x.
Li, Y. G. (2010), Fault damage in the 2008 M8 Wenchuan Earthquake Epicentral Region, *Academic Perspective, 6*(1), 2-16.
Li, Y. G., and P. Leary (1990), Fault zone trapped seismic waves, *Bull. Seismol. Soc. Am., 80*(5), 1245-1271.
Li, Y. G., K. Aki, D. Adams, A. Hasemi, and W. H. K. Lee (1994), Seismic guided waves trapped in the fault zone of the Landers, California, earthquake of 1992, *J. Geophys. Res., 99*(B6), 11705-11711,11722.
Li, Y. G., J. E. Vidale, S. M. Day, and D. D. Oglesby (2002), Study of the 1999 M 7.1 Hector Mine, California, earthquake fault plane by trapped waves, *Bull. Seismol. Soc. Am., 92*(4), 1318-1332.
Li, Y. G., P. Chen, E. S. Cochran, J. E. Vidale, and T. Burdette (2006), Seismic evidence for rock damage and healing on the San Andreas fault associated with the 2004 M 6.0 Parkfield earthquake, *Bull. Seismol. Soc. Am., 96*(4B), S349-S363, doi:10.1785/0120050803.
Lin, G., and P. Shearer (2007), Estimating local Vp/Vs ratios within similar earthquake clusters, *Bull. Seismol. Soc. Am,. 97*, 379-388.
Lin, G., and P. Shearer (2009), Evidence for water-filled cracks in earthquake source regions, *Geophys. Res. Lett., 36*, L17315.
Loveless, J. P., and B. J. Meade (2010), Geodetic image of plate motions, slip rates, and partitioning of deformation in Japan, *J. Geophys. Res., 115*, B02410, doi: 10.1029/2008JB006248.
Luo, Y., Y. Tan, S. Wei, D. Helmberger, Z. Zhan, S. Ni, E. Hauksson, and Y. Chen (2010), Source mechanism and rupture directivity of the 18 May 2009 Mw 4.6 Inglewood, California, Earthquake, *Bull. Seismol. Soc. Am., 100*(6), 3269-3277, doi:10.1785/0120100087.
Ma, S., and G. C. Beroza (2008), Rupture dynamics on a bimaterial interface for dipping faults, *Bull. Seismol. Soc. Am., 98*(4), 1642-1658, doi: 10.1785/0120070201.

Ma, S., and E. T. Hirakawa (2013), Dynamic wedge failure reveals anomalous energy radiation of shallow subduction earthquakes, *Earth Planet. Sci. Lett., 375*, 113-122.
Madariaga, R. (1976), Dynamics of an expanding circular fault, *Bull. Seismol. Soc. Am., 66*(3), 639-666.
Madariaga, R. (1983), High-frequency radiation from dynamic earthquake fault models, *Ann. Geophys., 1*, 17-23.
Madariaga, R., J.-P. Ampuero, and M. Adda-Bedia (2006), Seismic radiation from simple models of earthquakes, *"Radiation Energy and the Physics of Earthquakes", AGU Monograph*; A. McGarr, R. Abercrombie, H. Kanamori and G. di Toro, Eds.
Meng, L., A. Inbal, and J.-P. Ampuero (2011), A window into the complexity of the dynamic rupture of the 2011 Mw 9 Tohoku-Oki earthquake, *Geophys. Res. Lett., 38*, L00G07,
Miura, S., N. Takahashi, A. Nakanishi, T. Tsuru, S. Kodaira, and Y. Kaneda (2005), Structural characteristics off Miyagi forearc region, the Japan Trench seismogenic zone, deduced from a wide-angle reflection and refraction study, *Tectonophysics*, *407*, 165-188.
Mizuno, T., Y. Kuwahara, H. Ito, and K. Nishigami (2008), Spatial variations in fault-zone structure along the Nojima fault, central Japan, as inferred from borehole observations of fault-zone trapped waves, *Bull. Seismol. Soc. Am., 98*(2), 558-570, doi:10.1785/0120060247.
Moczo, P., J. Kristek, and L. Halada (2004), *The Finite-Difference Method for Seismologists. An Introduction*. Comenius University, Bratislava.
Nielsen, S. B. (1998), Free surface effects on the propagation of dynamic rupture, *Geophys. Res. Lett*., *25*(1), 125-128.
Noda, H., and N. Lapusta (2010), Three-dimensional earthquake sequence simulations with evolving temperature and pore pressure due to shear heating: Effect of heterogeneous hydraulic diffusivity, *J. Geophys. Res.*, *115*, B12314, doi: 10.1029/2010JB007780.
Noda, H., and N. Lapusta (2012), On averaging interface response during dynamic rupture and energy partitioning diagrams for earthquakes, *J. Appl. Mech., 79*, 031026.
Noda, H., and N. Lapusta (2013), Stable creeping fault segments can become destructive as a result of dynamic weakening, *Nature, 493*, 518-523.
Oglesby, D. D. (2008), Rupture termination and jump on parallel offset faults, *Bull. Seismol. Soc. Am., 98*, 440-447.
Oglesby, D. D., and S. M. Day (2002), Stochastic fault stress: Implications for fault dynamics and ground motion, *Bull. Seismol. Soc. Am., 92*(8), 3006-3021.
Olsen, K. B., R. Madariaga, and R. J. Archuleta (1997), Three-dimensional dynamic simulation of the 1992 Landers earthquake, *Science, 278*, 834-838.
Pelties, C., Y. Huang, and J.-P. Ampuero (2013), Pulse-like rupture induced by three-dimensional fault zone flower structures, Abstract EGU2013-269 presented at EGU General Assembly 2013, EGU, Vienna, Austria, 7-12 Apr.
Peng, Z., Y. Ben-Zion, A. J. Michael and L. Zhu (2003), Quantitative analysis of seismic fault zone waves in the rupture zone of the 1992 Landers, California, earthquake: evidence for a shallow trapping structure, *Geophys. J. Int., 155*(3), 1021-1041, doi:10.1111/j.1365-246X.2003.02109.x.
Perrin, G., J. R. Rice, and G. Zheng (1995), Self-healing slip pulse on a frictional surface, *J. Mech. Phys. Solids, 43*(9), 1461-1495.
Pollitz, F. F., R. Burgmann, and P. Banerjee (2011), Geodetic slip model of 2011 M9.0 Tohoku earthquake, *Geophys. Res. Lett*., *38*, L00G08, doi: 10.1029/2011GL048632.
Reches, Z., and D. A. Lockner (2010), Fault weakening and earthquake instability by powder lubrication, *Nature, 467*, 452-455, doi:10.1038/nature09348.
Rempe, M. T. Mitchell, J. Renner, S. Nippress, Y. Ben-Zion, and T. Rockwell (2013), Damage and seismic velocity structure of pulverized rocks near the San Andreas Fault, *J. Geophys. Res. Solid Earth, 118*, 2813-2831, doi:10.1002/jgrb.50184.

Rice, J. R. (1993), Spatio-temporal complexity of slip on a fault, *J. Geophys. Res., 98*, 9885-9907.
Rice, J. R. (2006), Heating and weakening of faults during earthquake slip, *J. Geophys. Res., 111*, B05311, doi:10.1029/2005JB004006.
Rice, J. R., C. G. Sammis, and R. Parsons (2005), Off-fault secondary failure induced by a dynamic slip pulse, *Bull. Seismol. Soc. Am., 95*(1), 109-134, doi:10.1785/0120030166.
Rojas, O., S. Day, J. Castillo, and L. A. Dalguer (2008), Modelling of rupture propagation using high order mimetic finite differences, *Geophys. J. Int., 172*(2), 631-650, doi:10.1111/j.1365-246X.2007.03651.x.
Rosakis, J. (1999), Cracks faster than the shear wave speed, *Science*, *284*, 1337-1340.
Rowe, C. D., J. C. Moore, F. Remitti, and the IODP Expedition 343/343T Scientists (2013), The thickness of subduction plate boundary faults from the seafloor into the seismogenic zone, *Geology, 41*(9), 991-994, doi: 10.1130/G34556.1.
Ruina, A. (1983), Slip instability and state variable friction laws, *J. Geophys. Res., 111*(B12), 10359-10370.
Sagy, A. and D. Korngreen (2012), Dynamic branched fractures in pulverized rocks from a deep borehole, *Geology, 40*(9), 799-802, doi: 10.1130/G33194.1.
Samudrala, O., Y. Huang, and A. J. Rosakis (2002a), Subsonic and inersonic mode II crack propagation with a rate dependent cohesive zone. *J. Mech. Phys. Solids, 50*, 1231-1268.
Samudrala, O., Y. Huang, and A. J. Rosakis (2002b), Subsonic and intersonic shear rupture of weak planes with a velocity weakening cohesive zone. *J. Geophys. Res., 107*(B8), 2170.
Sato, H., T. Ishikawa, N. Ujihara, S. Yoshida, M. Fujita, M. Mochizuki, and A. Asada (2011), Displacement above the hypocenter of the 2011 Tohoku-Oki earthquake, *Science, 332*, 1395.
Savage, H. M., and E. E. Brodsky (2011), Collateral damage: evolution with displacement of fracture distribution and secondary fault strands in fault damage zones, *J. Geophys. Res., 116*(B3), B03405, doi:10.1029/2010JB007665.
Scholz, C. H. (1987), Wear and gouge formation in brittle faulting, *Geology, 15*(6), 493-495, doi: 10.1130/0091-7613(1987)15<493:WAGFIB>2.0.CO;2.
Sekiguchi, H., and T. Iwata (2002), Rupture process of the 1999 Kocaeli, Turkey, earthquake estimated from strong-motion waveforms, *Bull. Seismol. Soc. Am., 92*, 300-311.
Shaw, B. E., and J. R. Rice (2000), Existence of continuum complexity in the elastodynamics of repeated fault ruptures, *J. Geophys. Res., 105*(B10), 23791-23810, doi:10.1029/2000JB900203.
Shearer, P. M. (1988), Cracked media, Poisson's ratio, and the structure of the upper oceanic crust, *Geophys. J., 92*, 357-362.
Shi, Z., and Y. Ben Zion (2006), Dynamic rupture on a bimaterial interface governed by slip weakening friction, *Geophys. J. Int., 165*(2), 469-484, doi:10.1111/j.1365-246X.2006.02853.x.
Sibson, R. H. (1986), Brecciation processes in fault zones: Inferences from earthquake rupturing, *Pure Appl. Geophys., 124*(1-2), 159-175, doi: 10.1007/BF00875724.
Simons, M., et al. (2011), The 2011 magnitude 9.0 Tohoku-Oki earthquake: Mosaicking the megathrust from seconds to centuries, *Science, 332*, 1421-1425.
Smith, D. E., and T. H. Heaton (2011), Models of stochastic, spatially varying stress in the crust compatible with focal-mechanism data, and how stress inversions can be biased toward the stress rate, *Bull. Seismol. Soc. Am., 101*(3), 1396-1421, doi:10.1785/0120100058.
Song, S. G., G. C. Beroza, and P. Segall (2008), A unified source model for the 1906 San Francisco earthquake, *Bull. Seismol. Soc. Am., 98*, 823-831.
Spudich, P., and E. Cranswick (1984), Direct observation of rupture propagation during the 1979 Imperial Valley earthquake using a short baseline accelerometer array, *Bull. Seismol. Soc. Am., 74*(6), 2083-2114.

Spudich, P., and K. Olsen (2001), Fault zone amplified waves as a possible seismic hazard along the Calaveras fault in central California, *Geophys. Res. Lett., 28*(13), 2533-2536.
Takei, Y. (2002), Effect of pore geometry on VP/VS: From equilibrium geometry to crack, *J. Geophys. Res., 107,* 2043.
Tajima, F., J. Mori, and B. L. N. Kennett (2013), A review of the 2011 Tohoku-Oki earthquake (Mw 9.0): Large-scale rupture across heterogeneous plate coupling, *Tectonophysics, 586*, 15-34.
Tan, Y., and D. Helmberger (2007), A new method for determining small earthquake source parameters using short-period P waves, *Bull. Seismol. Soc. Am., 97*, 1176-1195.
Tan, Y., and D. Helmberger (2010), Rupture directivity characteristics of the 2003 Big Bear Sequence, *Bull. Seismol. Soc. Am., 100*(3), 1089-1106, doi:10.1785/0120090074.
Templeton, E. L., and J. R. Rice (2008), Off-fault plasticity and earthquake rupture dynamics: 1. Dry materials or neglect of fluid pressure changes, *J. Geophys. Res., 113,* B09306, doi:10.1029/2007JB005529.
Tobin, H. J., and D. M. Saffer (2009), Elevated fluid pressure and extreme mechanical weakness of a plate boundary thrust, Nankai Trough subduction zone, *Geology, 37*, 679-682.
Tromp, J., D. Komatitsch, and Q. Y. Liu (2008), Spectral-element and adjoint methods in seismology, *Commun. Comput. Phys.*, *3*(1), 1-32.
Vallée, M., M. Landès, N. M. Shapiro, and Y. Klinger (2008), The 14 November 2001 Kokoxili (Tibet) earthquake: High-frequency seismic radiation originating from the transitions between sub-Rayleigh and supershear rupture velocity regimes, *J. Geophys. Res., 113*, B07305.
Wald, D. J., and T. H. Heaton (1994), Spatial and temporal distribution of slip for the 1992 Landers, California, earthquake, *Bull. Seismol. Soc. Am., 84*(3), 668-691.
Walker, K. T., and P. M. Shearer (2009), Illuminating the near-sonic rupture velocities of the intracontinental Kokoxili Mw 7.8 and Denali fault Mw 7.9 strike-slip earthquakes with global P wave back projection imaging, *J. Geophys. Res., 114,* B02304, doi:10.1029/2008JB005738.
Wang, D., and J. Mori (2012), The 2010 Qinghai, China, earthquake: A moderate earthquake with supershear rupture, *Bull. Seismol. Soc. Am., 102*, 301-308.
Weertman, J. (1980), Unstable slippage across a fault that separates elastic media of different elastic constants, *J. Geophys. Res., 85*(B3), 1455-1461, doi:10.1029/JB085iB03p01455.
Weertman, J. (2014), Transonic gliding edge dislocations/slip pulse near and on an interface/fault, *J. Geophys. Res.*, doi:10.1002/2013JB010121.
Wei, S., R. Graves, D. Helmberger, J.-P. Avouac, and J. Jiang (2012), Sources of shaking and flooding during the Tohoku-Oki earthquake: A mixture of rupture styles, *Earth Planet. Sci. Lett., 333-334*, 91-100.
Xia, K., A. J. Rosakis, and H. Kanamori (2004), Laboratory Earthquakes: The Sub-Rayleigh-to-Supershear Rupture Transition, *Science, 303*(5665), 1859-1861, doi:10.1126/science.1094022.
Xu, S., J. P. Ampuero, Y. Ben-Zion, and V. Lyakhovsky (2009), Dynamic rupture on a frictional interface with off-fault damage, Eos Trans. AGU, 90(52), Fall Meet. Suppl., Abstract T43A-2040.
Xu, S., Y. Ben-Zion, and J.-P. Ampuero (2012), Properties of inelastic yielding zones generated by in-plane dynamic ruptures-I. Model description and basic results, *Geophys. J. Int.*, *191*(3), 1325-1342, doi: 10.1111/j.1365-246X.2012.05679.x.
Yagi, Y., and Y. Fukahata (2011), Rupture process of the 2011 Tohoku-oki earthquake and absolute elastic strain release, *Geophys. Res. Lett., 38*, L19307.
Yang, H. and L. Zhu (2010), Shallow low-velocity zone of the San Jacinto fault from local earthquake waveform modeling, *Geophys. J. Int., 183*(1), 421-432, doi:10.1111/j.1365-246X.2010.04744.x.
Yang, H., L. Zhu and E. S. Cochran (2011), Seismic structures of the Calico fault zone inferred from local earthquake travel time modeling, *Geophys. J. Int., 186*(2), 760-770, doi:10.1111/j.1365-246X.2011.05055.x.

Yao, H., P. Gerstoft, P. M. Shearer, and C. Mecklenbräuker (2011), Compressive sensing of the Tohoku-Oki Mw 9.0 earthquake: Frequency-dependent rupture modes, *Geophys. Res. Lett*., *38*, L20310, doi:10.1029/2011GL049223.

Yoshida, S., and N. Kato (2011), Pore pressure distribution along plate interface that causes a shallow asperity of the 2011 great Tohoku-oki earthquake, *Geophys. Res. Lett., 38*, L00G13.

Yue, H., and T. Lay (2011), Inversion of high-rate (1sps) GPS data for rupture process of the 11 March 2011 Tohoku earthquake (Mw 9.1), *Geophys. Res. Lett., 38*, L00G09.

Yue, H., T. Lay, J. T. Freymueller, K. Ding, L. Rivera, N. A. Ruppert, and K. D. Koper (2013), Supershear rupture of the 5 January 2013 Craig, Alaska (M_w 7.5) earthquake, *J. Geophys. Res., 118*, 5903-5919.

Zheng, G., and J. R. Rice (1998), Conditions under which velocity-weakening friction allows a self-healing versus a cracklike mode of rupture, *Bull. Seismol. Soc. Am., 88*(6), 1466-1483.